Summer 2021

Development and Implementation of Novel Intelligent Motor Control for Performance Enhancement of PMSM Drive in Electrified Vehicle Application

Soumava Bhattacharjee
University of Windsor

Development and Implementation of Novel Intelligent Motor Control for Performance Enhancement of PMSM Drive in Electrified Vehicle Application

By

Soumava Bhattacharjee

A Thesis
Submitted to the Faculty of Graduate Studies
through the Department of Electrical and Computer Engineering
in Partial Fulfillment of the Requirements for
the Degree of Master of Applied Science
at the University of Windsor

Windsor, Ontario, Canada

Development and Implementation of Novel Intelligent Motor Control for Performance Enhancement of PMSM Drive in Electrified Vehicle Application

by

Soumava Bhattacharjee

APPROVED BY:

_____

Y. H. Kim
Department of Civil and Environmental Engineering

_____

B. Balasingam
Department of Electrical and Computer Engineering

_____

K. L. V. Iyer, Co–Advisor
Department of Electrical and Computer Engineering

_____

N. C. Kar, Co–Advisor
Department of Electrical and Computer Engineering

April 30, 2021

DECLARATION OF CO–AUTHORSHIP/PREVIOUS PUBLICATIONS

I. Co–Authorship

I hereby declare that this thesis incorporates material that is the result of joint research, as follows: This thesis includes the outcome of publications which also have co-authors who are/were graduate students or post-doctoral fellows supervised by Dr. Narayan Kar. In all cases, only the primary contributions of the author towards these publications are included in this thesis. The contribution of co–authors was primarily through the provision of assistance in experimentation and analysis.

I am aware of the University of Windsor Senate Policy on Authorship and I certify that I have properly acknowledged the contribution of other researchers on my thesis and have obtained written permission from each of the co–author(s) to include the above material(s) in my thesis. I certify that, with the above qualification, this thesis, and the research to which it refers, is the product of my own work.

II. Previous Publication

This thesis includes selected sections and extended work of research that have been published/submitted for publication in peer-reviewed IEEE Transactions and IEEE International Conferences, as follows:

Thesis Chapter	Publication title/full citation	Publication status
3	**S. Bhattacharjee**, S. Halder, A. Kundu, K. L. V. Iyer, and N. C. Kar, "Artificial Neural Network Based Improved Modulation Strategy for GaN–Based Inverter in EV," in proceedings of the *IEEE Canadian Conference on Electrical and Computer Engineering*, Canada, 2020.	*Published*
5, 6	**S. Bhattacharjee**, S. Halder, A. Balamurali, M. Towhidi, K. L. V. Iyer, and N.C. Kar, "An Advanced Policy Gradient Based Vector Control of PMSM for EV Application," in *Electric Drives Production Conference*, Germany, 2020.	*Published*

5, 6	**S. Bhattacharjee**, S. Halder, Y. Yan, A. Balamurali, K. L. V. Iyer, and N.C. Kar, "Real–Time SIL Validation of a Novel PMSM Control Based on Deep Deterministic Policy Gradient Scheme for Electrified Vehicles," in *IEEE Transactions on Power Electronics*, April 2021.	*Submitted*
5	**S. Bhattacharjee,** Y. Yan, K. L. V. Iyer, and N.C. Kar, "Multi–Critic Based Enhanced Vector Control Optimization with Multi–Q–Learning for Motor Control," US Patent Publication.	*Submitted Provisional Patent*

I certify that I have obtained written permission from the copyright owners to include the above published materials in my thesis. I certify that the above material describes work completed during my registration as a graduate student at the University of Windsor.

III. General

I declare that, to the best of my knowledge, my thesis does not infringe upon anyone's copyright nor violate any proprietary rights and that any ideas, techniques, quotations, or any other material from the work of other people included in my thesis, published or otherwise, are fully acknowledged in accordance with the standard referencing practices. Furthermore, to the extent that I have included copyrighted material that surpasses the bounds of fair dealing within the meaning of the Canada Copyright Act and has included copies of such copyright clearances to the appendix of this thesis.

I declare that this is a true copy of my thesis, including any final revisions, as approved by my thesis committee and the Graduate Studies office, and that this thesis has not been submitted for a higher degree to any other University or Institution.

ABSTRACT

The demand for electrified vehicles has grown significantly over the last decade causing a shift in the automotive industry from traditional gasoline vehicles to electric vehicles (EVs). With the growing evolution of EVs, high power density, and high efficiency of electric powertrains (e–drive) are of the utmost need to achieve an extended driving range. However, achieving an extended driving range with enhanced e-drive performance is still a bottleneck.

The control algorithm of e–drive plays a vital role in its performance and reliability over time. Artificial intelligence (AI) and machine learning (ML) based intelligent control methods have proven their continued success in fault determination and analysis of motor–drive systems. Considering the potential of intelligent control, this thesis investigates the legacy space vector modulation (SVM) strategy for wide–bandgap (WBG) inverter and conventional current PI controller for permanent magnet synchronous motor (PMSM) control to reduce the switching loss, computation time and enhance transient performance in the available state–of–the-art e–drive systems. The thesis converges on AI– and ML–based control for e–drives to enhance the performance by focusing in reducing switching loss using ANN–based modulation technique for GaN–based inverter and improving transient performance of PMSM by incorporating ML–based parameter independent controller.

Dedicated to my parents and sister-

Bhaskar Bhattacharjee, Anjana Bhattacharjee, and

Dr. Chandrima Bhattacharjee.

I love you all.

ACKNOWLEDGEMENTS

I hereby express my sincere gratitude to my advisor Dr. Narayan C. Kar, for his kind encouragement, continuous guidance throughout the study, and research for the past two years in my MASc program. I owe a part of my success to his encouragement towards the growth of research work and provide resources to achieve excellence by developing novel ideas.

Also, I am grateful to my co–advisor Dr. Lakshmi Varaha Iyer for guiding and supporting my research with his constant motivations and pushing my boundaries to achieve an extra mile. I thank you for your constant support with your resources and for helping me to implement my research.

I would also like to express my gratitude and respect towards my thesis committee members, Dr. Balakumar Balasingam and Dr. Yong Hoon Kim for agreeing to serve on my committee, and attending my seminars and defense. With their valuable suggestions, I was able to improve the quality of my research and this thesis.

I would like to thank Dr. Sreekanta Das for introducing me to Dr. Kar and being my local guardian at Windsor. His constant guidance and motivation played an integral role in this journey.

I am thankful to Dr. Sukanta Halder for his continuous guidance during my research at CHARGE labs. His idea and inspiration encouraged me to work in this field of research.

I am thankful to past and present colleagues and friends who supported me enormously during my research. I appreciate the guidance and expert opinions from Dr. Debmalya Banerjee, Dr. Aishwarya Balamurali, and others with timely advice. In addition, I am very thankful to Mr. Ye Yan for his guidance and proactive help with my research. Also, special thanks to Mrs. Eunha Chu for her relentless help and important suggestions in all my scientific contributions.

I express my profound gratitude to my parents and my sister who encouraged me, supported me, and gave me the confidence and strength to overcome all difficulties in life.

TABLE OF CONTENTS

LIST OF TABLES

LIST OF FIGURES

CHAPTER 1

INTRODUCTION

Electric vehicles (EVs) are gaining significant attention for research and advancement in recent years mainly due to global climate change and awareness for sustainable development. Zero emission as well as lower operating and maintenance costs of EVs with additional autonomous capabilities has led to an increased global commercialization and sales as shown in Fig. 1.1 [1]. The government of Canada has also set ambitious targets for EVs to increase sales to 100% by 2040 [2]. However, EVs are not sufficiently developed to compete with existing gasoline vehicles. With the increasing market demand, the government and private organizations have set targets and milestones to further advance and improve the electrification process. These milestones focus on improving different features of EVs such as the traction motor and drives, power electronics components, fast charging capability, State of Health (SoH), reliability, and so on [3]. As the electrification process progresses, it is the need of the hour to further enhance the control techniques for optimal performance and improved efficiency. The last decade witnessed a significant advancement in deep learning (DL) and machine learning (ML) based intelligent control which achieved remarkable performance in different engineering, medical, and scientific domains [4]–[6]. To further utilize its potential, DL–based controls are incorporated in motor drives to enhance performance for EV applications [7].

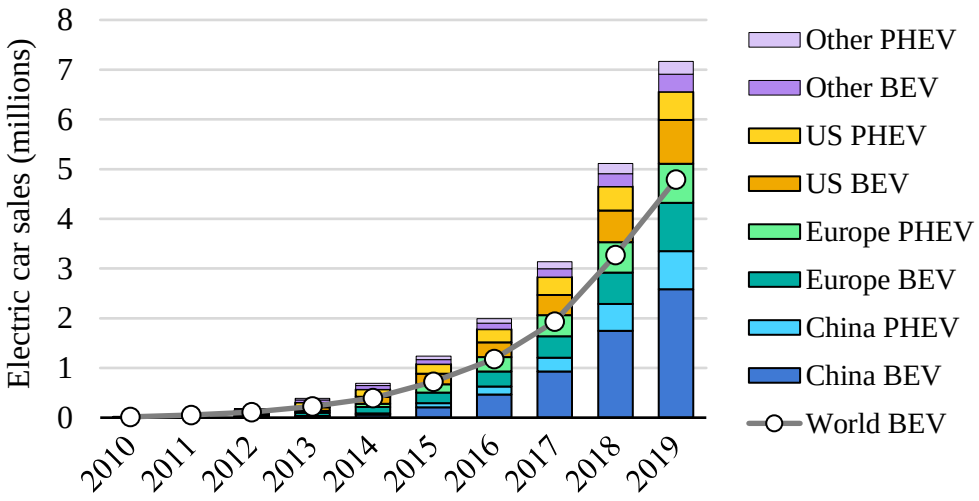

Fig. 1.1. Global electric car sales, FY2020 [1].

1.1 Overview of Electrified Vehicles

The concept of electric vehicles is well known from the design of electric–powered carriage by Robert Anderson in 1832 [8]. With the rapid shift in technology, the concept of EV took different forms such as hybrid electric vehicles (HEVs), plug–in hybrid electric vehicles (PHEVs), battery electric vehicles (BEVs), and fuel cell electric vehicles (FCEV). Further regulatory actions are imposed by the governments to shift from HEVs to BEVs to mandate zero–emission. Incorporation of the autonomous capability with LiDAR technology in BEVs like Tesla Model X and Audi e–tron has boosted the attention of customers leading to increased sales. A physical powertrain layout of a BEV is shown in Fig. 1.2.

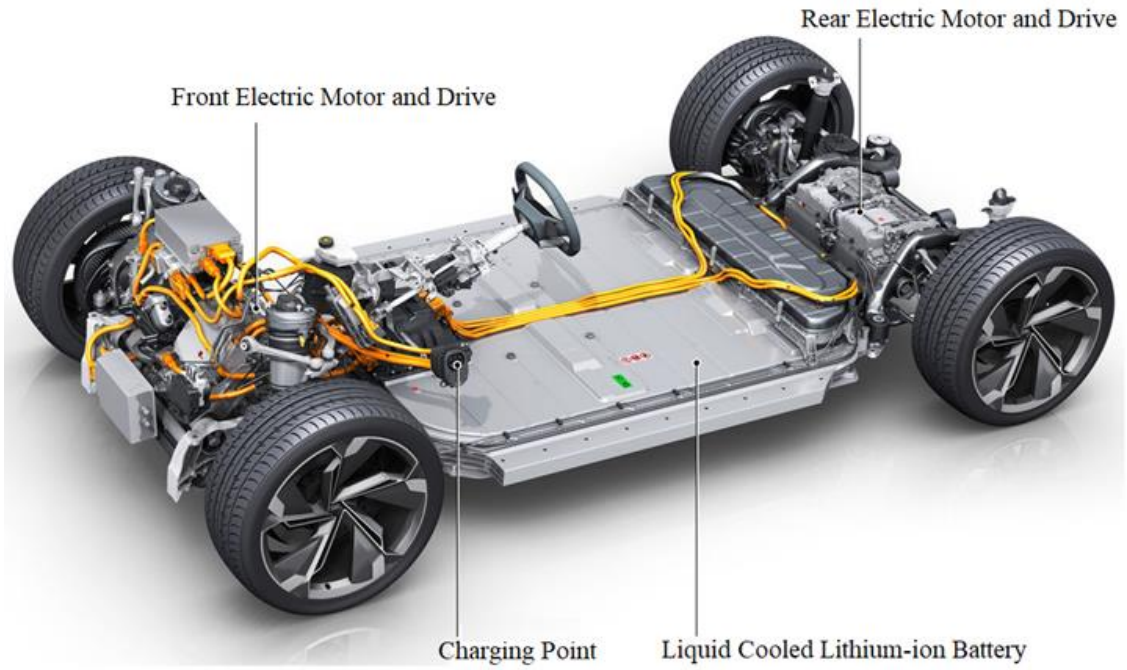

Fig. 1.2. Powertrain layout of Audi e–tron Sportback [9].

BEVs incorporate different subsystems mainly motor–drive system, a battery pack integrated with a charging point, a battery management system, and a master controller to monitor the overall control system. Several technologies and control strategies are employed for the system to interact with each other to make an EV operate. The integrated motor–drive systems house the traction motor with the power inverter and the motor controller. Based on the manufacturer, either a permanent magnet synchronous motor

(PMSM) or an induction motor (IM) is used for traction. The motor predominantly interacts with the power converter and the controller to drive the EV under steady and dynamic conditions. The interaction varies among subsystems however each system plays a crucial role in the overall operation of EV. The interaction among different subsystems of an EV is shown in Fig. 1.3 [10]. Using the ideology, over the years different models of EVs are introduced in the market. Table 1.1 presents the commercially available EVs in the Canadian market.

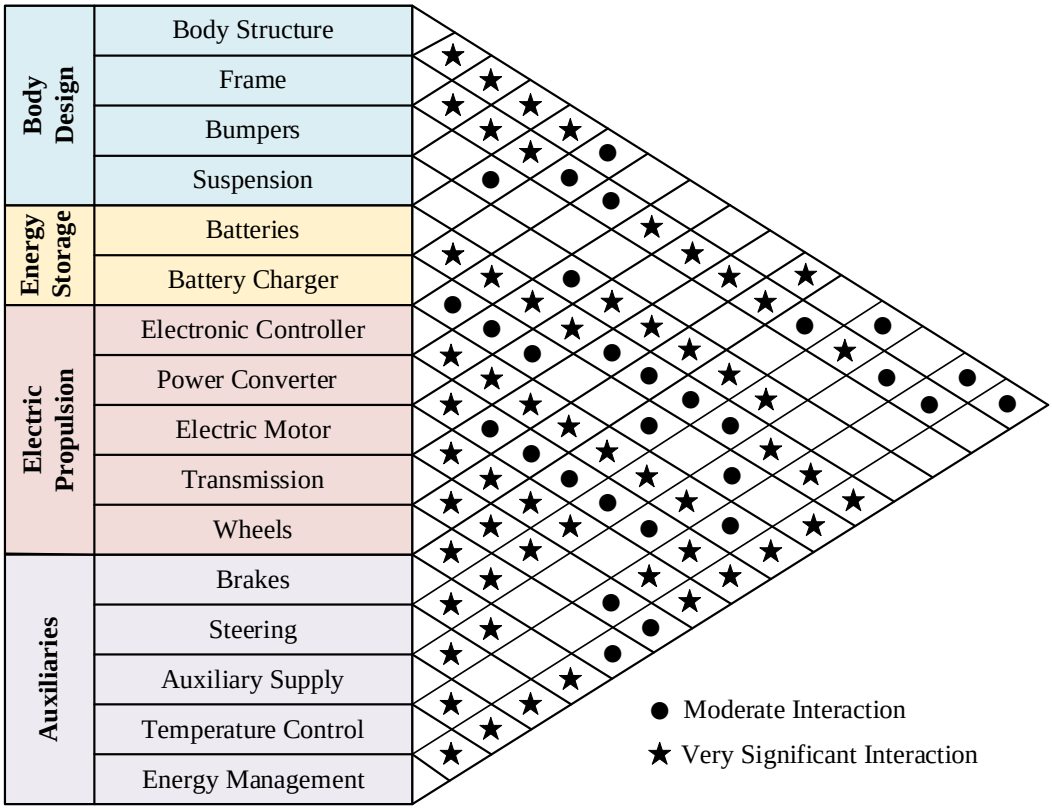

Fig. 1.3. Interaction among various EV subsystems [10].

1.2 Overview of PMSM Drives in Electrified Vehicles

Permanent magnet synchronous motor (PMSM) drives are widely used in engineering and industrial applications such as robotics, automotive, and aerospace [12]–[15]. Study shows that 83% of automotive OEMs use PMSM drives compared to IM drives in their electric vehicles [16]. Overtime PMSM drive designs have been improved in terms of high torque, high power density, reliability, and lightweight compared to other motor drive technology

TABLE 1.1

COMMERCIALLY AVAILABLE EVS IN Canada, 2020 [11]

	Plug–in Hybrid EVs (PHEVs)		Battery EVs (BEVs)	
Motor	Internal combustion engine and electric motor		One or more electric motors	
Range	All–electric: 20 to 200 km		100 to 700 km	
Models and All Electric Range	**Model**	**Range**	**Model**	**Range**
	Toyota RAV4 / Prius	68 km / 40 km	Volkswagen e–Golf	201 km
	Hyundai IONIQ	47 km	MINI Cooper SE	177 km
	Ford Fusion Energi / Escape	42km / 65km	Hyundai IONIQ / KONA	274 km / 415 km
	Kia Niro / Optima	45 km	Kia Soul / Nitro	391 km
	Honda Clarity	77 km	Nissan LEAF	363 km
	Subaru Crosstrek	27 km	BMW i3	246 km
	Mitsubishi Outlander	35 km	Chevrolet BOLT	417 km
	MINI Cooper SE Countryman	29 km	Tesla Model 3 / Model Y / Model S / Model X	568 km / 525 km / 663 km / 580 km
	BMW i3 REx / X3 xDrive30e / 530e / i8	203 km / 29 km / 46 km / 29 km	Audi e–tron	351 km
	Chrysler Pacifica Hybrid	53 km	Jaguar I–PACE	377 km
	Volvo S60 / V60 / XC60 / S90 / XC90 T8	35 km	Porche Taycan	323 km
	Audi Q5 TFSIe	32 km	Ford Mustang Mach E	483 km
	Lincoln Aviator Grand Touring	34 km	GM Hummer (pre–order)	485+ km
	Porsche Panamera E–Hybrid	23 km	Tesla Cybertruck (pre–order)	402+ km
	Mercedes Benz S 560e	31 km	Volvo XC40 Pure Electric	335 km
	Bentley Bentayga	29 km		

[17]–[18]. Also, a wide speed–torque range at low–speed operation is achieved in PMSM drives.

A very significant interaction between the traction motor, power converter, and its control strategy is noted from Fig. 1.3. The operation of the inverter plays a key role in the efficiency of the PMSM. However, the conduction losses, switching losses, parasitic losses due to converter topology, and other losses affect the efficiency and overall performance of the inverter [18]. The losses from the power converter add to the overall loss of the

machine leading to increased losses. Ongoing research focuses on enhanced power converter topology with next–generation wide bandgap (WBG) based silicon carbide (SiC) and gallium nitride (GaN) switches [20]–[22].

With the evident requirement of high speed–torque characteristics over a wide driving range, there is still an opportunity to improve the overall PMSM drive performance. This calls for an enhanced control strategy to harness the potential of the newly designed e–drive by increasing efficiency, reliability, and robust control strategies.

1.3 Background of Control Strategies for PMSM Drives

The fundamental operation of PMSM is characterized by wide speed–torque characteristics by ensuring smooth rotation over the entire speed range and full torque control including fast acceleration and deceleration [23]. In the EV industry, the PMSM control standard is governed by traditional vector controls mainly field–oriented control (FOC) and direct torque control (DTC) due to its robust performance and efficient low–cost real–time implementation capabilities. Growing research involves advanced control strategies incorporating sophisticated techniques with the existing FOC or DTC concepts to enhance the performance and stability of the motor drive system.

1.3.1 Field–Oriented Control

With enhanced performance and operational capabilities of PMSMs, the AC motor dynamics get complicated due to its coupled magnetic flux and torque vectors. With the conceptualization of Park transformation by Robert H. Park in 1929, the stator current vector of PMSM can be easily decoupled to separate magnetizing flux and torque vectors. This enabled the development of FOC control for AC machines and drives [24]. Vector control or FOC achieved efficient and reliable control of PMSM with enhanced dynamic performance. The control theory decomposes the reference current vectors in the direct and quadrature coordinate axes represented as i_d and i_q respectively from the speed controller of the drive. Proportional–Integral (PI) controllers are integrated to track the reference speed and current compared with the feedback values. Fig. 1.4 shows the overview block diagram of FOC in PMSM. Detailed analysis and study of different variants of FOC control are illustrated in Chapter 4.

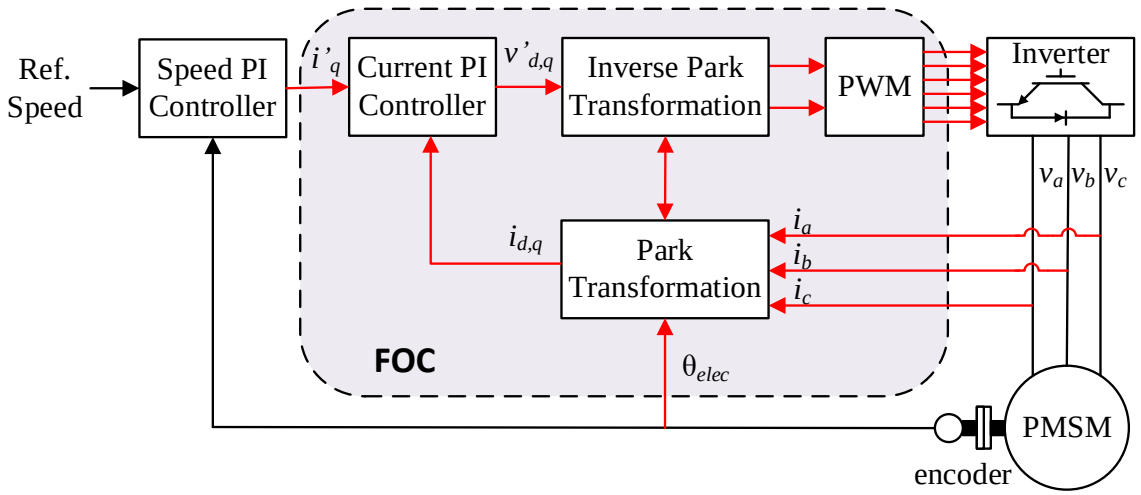

Fig. 1.4. Overview block diagram of field–oriented control (FOC).

1.3.2 Direct Torque Control

In 1986 DTC was introduced by Isao Takahashi and Toshihiko Noguchi from Japan in an IEEE journal [25]. The control was initially proposed for induction machines however later it was adopted for PMSMs. With the promising and outstanding torque control and dynamic performance of PMSM, it became an alternative control scheme for PMSM. DTC scheme influences direct control of stator flux, unlike stator current control in FOC technique.

The conventional DTC scheme assumes a constant stator voltage with no change in rotor flux for a given time frame. Hence rapid flux and electromagnetic torque control can be achieved with enhanced torque response from the machine. Since torque control is equivalent to current control, the stator current is also governed indirectly. The block diagram for DTC is shown in Fig. 1.5.

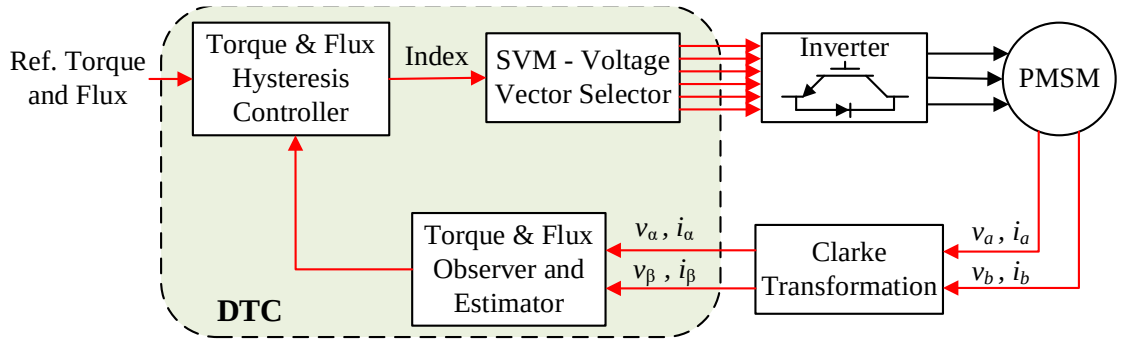

Fig. 1.5. Block diagram of direct torque control (DTC).

The control scheme incorporates a flux observer to determine the location of the stator flux. It computes the electromagnetic torque of the motor and a bang–bang control is adopted by comparing the reference flux and torque. Next, the appropriate voltage vector from the space vector modulation technique is selected to control the torque angle and further achieve torque control in PMSMs.

1.3.3 Advanced Control Strategies

The advancement in modern control strategies plays a key role in the development of high–performance PMSM drives. Advanced control strategies are incorporated in the conventional FOC and DTC algorithm to enhance the dynamic performance and overall stability of the control system. The advanced control strategies for PMSM drives can be classified as:

1. Improved conventional control techniques
2. Modern control theory based PMSM control
3. Intelligent control methodologies

PID controller algorithm and tuning methodology have been improved over the years to enhance system dynamic performance and stability. Over the years PID control is further integrated with the anti–windup feature to enable smooth transition during any varying environment. Incorporating resonant controller and optimization methodologies with particle swarm algorithm and fuzzy control with exiting PID control algorithm has enhanced the performance of the conventional PID controller [26]–[28]. The effective tuning of PID controller parameters depends on plant parameters which are derived from inverter and motor transfer functions. Under the entire operating range of the motor, equivalent circuit parameters changes which affects the control performance of the motor.

Modern control theory includes adaptive, robust, and predictive control algorithms for PMSM control. These types of model–based controls consider parameter variation and saturation of PMSM drives in terms of cost function and hence mitigating non–linearity of the system. Robust control techniques including H∞ control and observer–based control have enabled enhanced dynamic control of PMSM with accurate speed and current tracking capability [29]–[35]. Modern control theory uses complex mathematical equations to evaluate performances at the next sampling state for optimal control signals. Moreover, it

makes use of the mathematical model of e–drive which increases the online computational burden further compromising the performance of PMSM.

Over the last decade, intelligent control algorithms have been enhanced drastically to improve the performance of any control system. Fuzzy logic controls, neural networks (NN), machine learning, and deep learning have enabled researchers to render high precision and robust control of PMSM drives. The self–learning ability of neural networks has enabled controls to learn from dynamic environments where the cost of exploration is expensive [36]–[39]. The use of legacy supervised learning in NNs requires large and labeled training and test data sets under different dynamic conditions enabling increased training time.

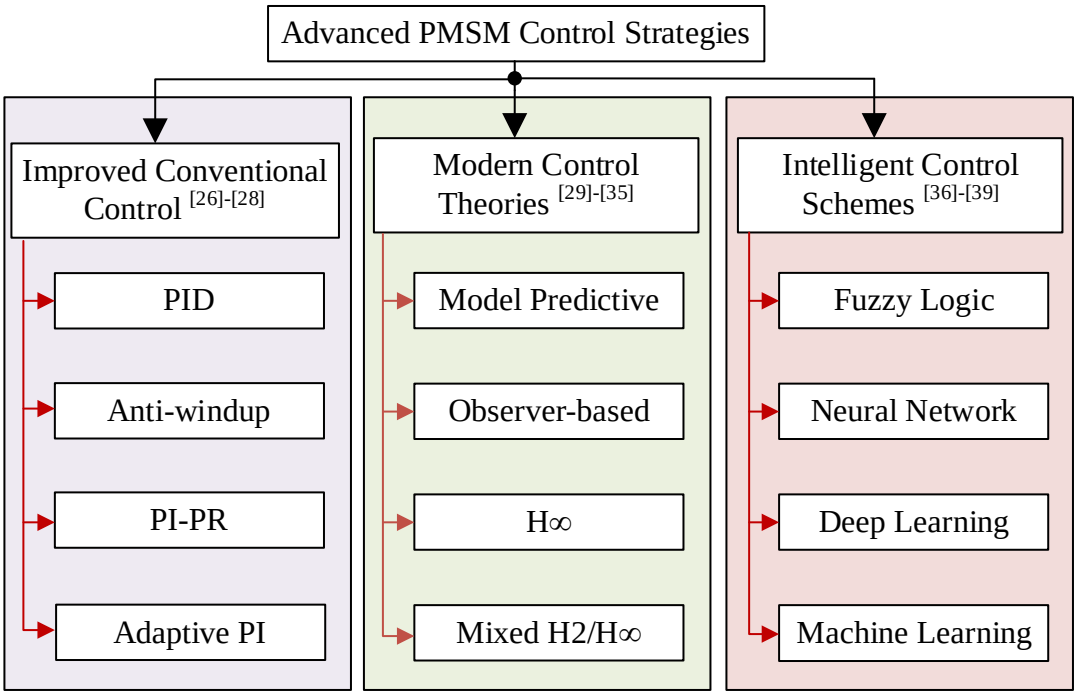

Fig. 1.6. Classification of advanced PMSM control strategies.

1.4 Research Objective and Contribution

This thesis focuses on the development and validation of advanced and intelligent control schemes for PMSM drives in electrified vehicles. The thesis investigates different conventional and modern control theory–based control techniques and proposes intelligent control techniques based on neural network and machine learnings. Initially, an artificial neural network (ANN) based on improved space vector modulation (SVM) for wide

bandgap (WBG) inverter is proposed and is validated with an in–house GaN inverter. Later, an advanced machine learning based vector control of PMSM e–drive is proposed and validated in real–time simulator. The major contributions of this thesis are summarized below:

1. Develop an ANN–based modified SVM technique and compare its performance with a modified SVM technique. Both modulation techniques are co–simulated in Simulink and PSIM and further validated using an in–house GaN inverter
2. Develop an advanced deep reinforcement learning (DRL) based controller for FOC of PMSM and the performance is compared with the adaptive PI–based FOC control. The proposed control algorithm is validated using an Opal–RT real–time simulator

1.5 Organization of this Thesis Highlighting Research Contribution

This thesis presents the research conducted towards developing an intelligent PMSM control for electrified vehicles. The thesis is represented in 7 chapters including this introductory chapter. A brief outlook of each chapter is summarized as follows:

Chapter 2 presents a mathematical model based improved space vector modulation (SVM) strategy, developed and verified using MATLAB Simulink. Finally, a methodology to further improve the SVM performance is proposed.

Chapter 3 introduces a soft computing ANN–based modified SVM for GaN inverter. Investigating an analytical study on WBG based high–frequency inverter, a detailed methodology on the training of the proposed modulation technique is presented in this chapter. Further, a co–simulation and comparative study on the proposed ANN–based modified SVM is presented. The implementation methodology and validation results of a 5 kW GaN inverter in a low cost 150 MHz DSP are also included in this chapter.

Chapter 4 presents a simulation study on different field–oriented control (FOC) methodologies of PMSM drive. The IPMSM dynamics with the state–of–the–art control is modeled and developed. An adaptive PI–based current controller is modeled and its performance is investigated using MATLAB Simulink.

Chapter 5 introduces an advanced machine learning based vector control for IPMSM. A deep reinforcement learning (DRL) based control technique is proposed. Deep

deterministic policy gradient based novel current controller (DPG–NCC) is developed for a robust vector control. The mathematical model and training methodology of the novel control is explained in this chapter.

Chapter 6 extends the research presented in chapter 5 to implement and validate the proposed DPG–NCC methodology. A validation technique with real–time OPAL–RT simulator is used to test its performance in real–time environment (RTE). A detailed comparative study with analysis of conventional and proposed control is presented in this chapter.

Chapter 7 concludes the thesis by summarizing the research work that has been achieved with the development of DPG–ACC based intelligent control techniques of IPMSM e–drive. The future work to further extend this research is also illustrated in this chapter.

1.6 References

[1] Global EV Outlook 2020, IEA (2020), Paris, “https://www.iea.org/reports/global-ev-outlook-2020”

[2] Zero Emission Vehicle Infrastructure Program, Government of Canada, “https://www.nrcan.gc.ca/energy-efficiency/energy-efficiency-transportation/zero-emission-vehicle-infrastructure-program/21876”

[3] U.S. Department of Energy, “Electrical and Electronics Technical Roadmap,” pp 1–41, 2017.

[4] F. Altaf, S. M. S. Islam, N. Akhtar, and N. K. Janjua, "Going Deep in Medical Image Analysis: Concepts, Methods, Challenges, and Future Directions," *IEEE Access*, vol. 7, pp. 99540–99572, 2019.

[5] A. Krizhevsky, I. Sutskever, and G. E. Hinton. "Imagenet Classification with Deep Convolutional Neural Networks," *Communications of the ACM*, vol. 60, no. 6, pp 84–90, 2017.

[6] D. Silver *et al.*, “Mastering the Game of Go Without Human Knowledge,” *Nature*, vol. 550, pp 354–359, 2017.

[7] X. Fu and S. Li, "A Novel Neural Network Vector Control Technique for Induction Motor Drive," *IEEE Trans. Energy Conversion*, vol. 30, no. 4, pp. 1428-1437, Dec. 2015.

[8] M. Guarnieri, "When Cars Went Electric, Part One [Historical]," *IEEE Industrial Electronics Magazine*, vol. 5, no. 1, pp. 61–62, March 2011.

[9] Electric Drivetrain of Audi e–tron Sportback Concept, "https://www.audi-mediacenter.com/en/photos/detail/audi-e-tron-sportback-concept-44496"

[10] C. C. Chan, "The State of the Art of Electric and Hybrid Vehicles," in *Proc. IEEE*, vol. 90, no. 2, pp. 247–275, Feb. 2002.

[11] Plug N' Drive, Electric Vehicles Available in Canada, 2020 Model Year, "https://www.plugndrive.ca/electric-cars-available-in-canada"

[12] F. Betin *et al*, "Trends in Electrical Machines Control: Samples for Classical, Sensorless, and Fault-Tolerant Techniques," *IEEE Industrial Electronics Magazine*, vol. 8, no. 2, pp. 43-55, June 2014.

[13] P. Pillay and R. Krishnan, "Application Characteristics of Permanent Magnet Synchronous and Brushless DC Motors for Servo Drives," *IEEE Trans. Industry Applications*, vol. 27, no. 5, pp. 986-996, Sept.-Oct. 1991.

[14] T. Zhao, S. Wu, and S. Cui, "Multiphase PMSM With Asymmetric Windings for More Electric Aircraft," *IEEE Trans. Transportation Electrification*, vol. 6, no. 4, pp. 1592-1602, Dec. 2020.

[15] T. Yuan, D. Wang, X. Wang, X. Wang, and Z. Sun, "High-Precision Servo Control of Industrial Robot Driven by PMSM-DTC Utilizing Composite Active Vectors," *IEEE Access*, vol. 7, pp. 7577-7587, 2019.

[16] Electric Motor for Electric Vehicles 2013-2023: Forecasts. Technologies, Players, IDTechEx research report, Nov. 2013

[17] Z. Yang, F. Shang, I. P. Brown and M. Krishnamurthy, "Comparative Study of Interior Permanent Magnet, Induction, And Switched Reluctance Motor Drives for EV and HEV Applications," *IEEE Trans. Transportation Electrification*, vol. 1, no. 3, pp. 245-254, Oct. 2015.

[18] R. Menon, A. H. Kadam, N. A. Azeez and S. S. Williamson, "A Comprehensive Survey on Permanent Magnet Synchronous Motor Drive Systems for Electric

Transportation Applications," in *Proc*. 2016 *IECON*, Florence, Italy, 2016, pp. 6627-6632.

[19] B. Sarlioglu, C. T. Morris, D. Han, and S. Li, "Driving Toward Accessibility: A Review of Technological Improvements for Electric Machines, Power Electronics, and Batteries for Electric and Hybrid Vehicles," *IEEE Industry Applications Magazine*, vol. 23, no. 1, pp. 14-25, Jan.-Feb. 2017.

[20] M. Farhadi, F. Yang, S. Pu, B. Vankayaplati, and B. Akin, "Temperature Independent Gate Oxide Degradation Monitoring of SiC MOSFETs Based on Junction Capacitances," *IEEE Trans. Power Electronics*, vol. 36, no. 7, pp. 8308-8324, 2021.

[21] E. Gurpinar and A. Castellazzi, "Single-Phase T-Type Inverter Performance Benchmark Using Si IGBTs, SiC MOSFETs, and GaN HEMTs," *IEEE Trans. Power Electronics*, vol. 31, no. 10, pp. 7148-7160, Oct. 2016.

[22] T. Liu, C. Chen, K. Xu, Y. Zhang, and Y. Kang, "GaN-Based MHz Single Phase Inverter with a Hybrid TCM Control Method for High Efficiency and High-Power Density," *IEEE Trans. Power Electronics*, vol. 36, no. 6, pp. 6797-6813, 2021.

[23] PMSM Control, NXP, “https://www.nxp.com/applications/industrial/aerospace-and-mobile-robotics/pmsm:PMSM-MOTORS”

[24] S. Vaez-Zadeh, “Control of Permanent Magnet Synchronous Motors,” Oxford University Press, 2018.

[25] I. Takahashi and T. Noguchi, "A New Quick-Response and High-Efficiency Control Strategy of an Induction Motor," *IEEE Trans. Industry Applications*, vol. IA-22, no. 5, pp. 820-827, Sept. 1986.

[26] P. March and M. C. Turner, "Anti-Windup Compensator Designs for Nonsalient Permanent-Magnet Synchronous Motor Speed Regulators," *IEEE Trans. Industry Applications*, vol. 45, no. 5, pp. 1598-1609, Sept.-Oct. 2009.

[27] A. V. Sant and K. R. Rajagopal, "PM Synchronous Motor Speed Control Using Hybrid Fuzzy-PI with Novel Switching Functions," *IEEE Trans. Magnetics*, vol. 45, no. 10, pp. 4672-4675, Oct. 2009.

[28] C. Xia, B. Ji, and Y. Yan, "Smooth Speed Control for Low-Speed High-Torque Permanent-Magnet Synchronous Motor Using Proportional–Integral–Resonant

Controller," *IEEE Trans. Industrial Electronics*, vol. 62, no. 4, pp. 2123-2134, April 2015.

[29] Y. Han, C. Gong, L. Yan, H. Wen, Y. Wang, and K. Shen, "Multiobjective Finite Control Set Model Predictive Control Using Novel Delay Compensation Technique for PMSM," *IEEE Trans. Power Electronics*, vol. 35, no. 10, pp. 11193-11204, Oct. 2020.

[30] G. Feng, C. Lai, and N. C. Kar, "A Closed-Loop Fuzzy-Logic-Based Current Controller for PMSM Torque Ripple Minimization Using the Magnitude of Speed Harmonic As the Feedback Control Signal," *IEEE Trans. Industrial Electronics*, vol. 64, no. 4, pp. 2642-2653, April 2017.

[31] Z. Wang, A. Yu, X. Li, G. Zhang, and C. Xia, "A Novel Current Predictive Control Based on Fuzzy Algorithm for PMSM," *IEEE Journal Emerging and Selected Topics Power Electronics*, vol. 7, no. 2, pp. 990-1001, June 2019.

[32] A. K. Junejo, W. Xu, C. Mu, M. M. Ismail, and Y. Liu, "Adaptive Speed Control of PMSM Drive System Based a New Sliding-Mode Reaching Law," *IEEE Trans. Power Electronics*, vol. 35, no. 11, pp. 12110-12121, Nov., 2020.

[33] S. Wang, K. Zhao, W. Wang, L. Sun, and D. Li, "Nonlinear Speed Control for PMSM Using Mixed H2/H∞ State Output Feedback Control," in *Proc. ICEMS*, Hangzhou, China, 2014, pp. 539-543.

[34] G. Feng, C. Lai, W. Li, Z. Li, and N. C. Kar, "Efficient Permanent Magnet Temperature Modeling and Estimation for Dual Three-Phase PMSM Considering Inverter Nonlinearity," *IEEE Trans. Power Electronics*, vol. 35, no. 7, pp. 7328-7340, July 2020.

[35] A. Balamurali, G. Feng, A. Kundu, H. Dhulipati, and N. C. Kar, "Noninvasive and Improved Torque and Efficiency Calculation Toward Current Advance Angle Determination for Maximum Efficiency Control of PMSM," *IEEE Trans. Transportation Electrification*, vol. 6, no. 1, pp. 28-40, March 2020.

[36] G. Feng, C. Lai, and N. C. Kar, "A Closed-Loop Fuzzy-Logic-Based Current Controller for PMSM Torque Ripple Minimization Using the Magnitude of Speed Harmonic as the Feedback Control Signal," *IEEE Trans. Industrial Electronics*, vol. 64, no. 4, pp. 2642-2653, April 2017.

[37] C. Wang and Z. Q. Zhu, "Fuzzy Logic Speed Control of Permanent Magnet Synchronous Machine and Feedback Voltage Ripple Reduction in Flux-Weakening Operation Region," *IEEE Trans. Industry Applications*, vol. 56, no. 2, pp. 1505-1517, March-April 2020.

[38] H. Jie, G. Zheng, J. Zou, X. Xin, and L. Guo, "Adaptive Decoupling Control Using Radial Basis Function Neural Network for Permanent Magnet Synchronous Motor Considering Uncertain and Time-Varying Parameters," *IEEE Access*, vol. 8, pp. 112323-112332, 2020.

[39] S. Li, H. Won, X. Fu, M. Fairbank, D. C. Wunsch, and E. Alonso, "Neural-Network Vector Controller for Permanent-Magnet Synchronous Motor Drives: Simulated and Hardware-Validated Results," *IEEE Trans. Cybernetics*, vol. 50, no. 7, pp. 3218-3230, July 2020.

CHAPTER 2

MATHEMATICAL MODELING OF MODIFIED SPACE VECTOR MODULATION STRATEGY

2.1 Introduction

Inverter control plays a crucial role in the performance and overall state of health (SoH) of PMSM drives. In a voltage source inverter (VSI), the switching of the device is achieved using the pulse width modulation (PWM) technique to produce variable frequency and voltage from a fixed DC voltage. A two–level inverter consists of six switches, S_1–S_6, which are arranged in a desired configuration as shown in Fig. 2.1. The performance and efficiency of VSI depend on the switching control scheme and hence an efficient modulation strategy for switching of power switches is necessary to achieve a wide modulation range, high frequency, and minimum loss of power converters [1]–[2]. Over time a wide variety of PWM approaches are developed and the commonly used PWM switching techniques are sinusoidal PWM (SPWM) and space vector modulation (SVM) [3]–[6]. In the subsequent sections of this chapter, detailed analysis with the mathematical model of the SVM algorithm is developed and its performance is verified using MATLAB Simulink.

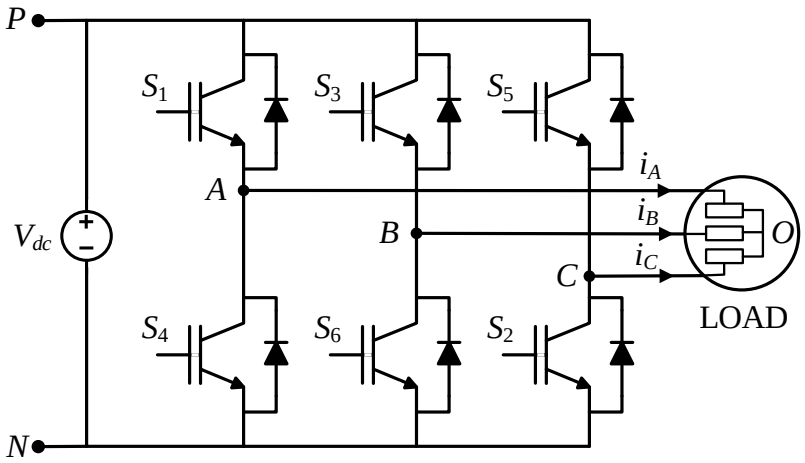

Fig. 2.1. Schematic of two–level VSI.

2.2 Sinusoidal PWM

SPWM generates the inverter gating signal by comparing a carrier wave with three sinusoidal reference waves shifted at 120°. Fig. 2.2 represents the simulation result for an output voltage of a VSI with total harmonics distortion (THD) analysis using the SPWM technique with RL load. The main drawback of this modulation scheme is its high harmonic content with increased total THD [7]–[10]. This leads to increased loss components such as switching loss, in the inverter. Third–harmonics injection can be incorporated with the reference wave to reduce the harmonics content. However, the disadvantage is the amount of added third harmonics components cannot be calculated with any predefined methodology. To mitigate the loss and reduce THD, a modified space vector modulation (SVM) algorithm is proposed in the next section.

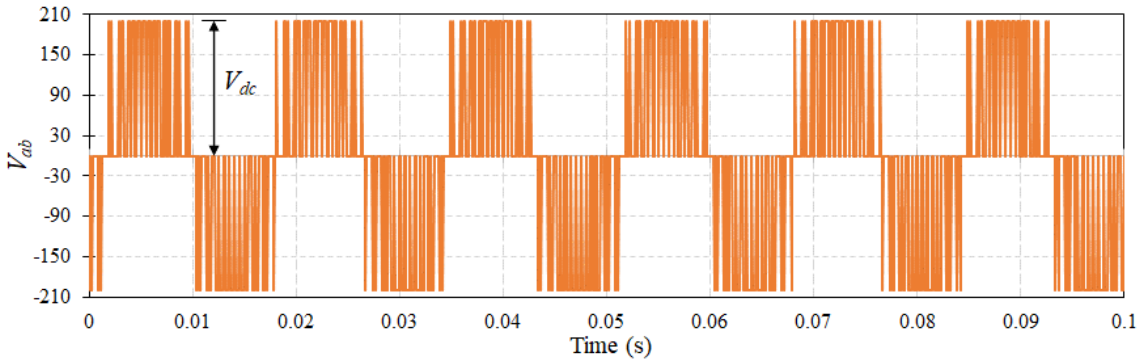

(a)

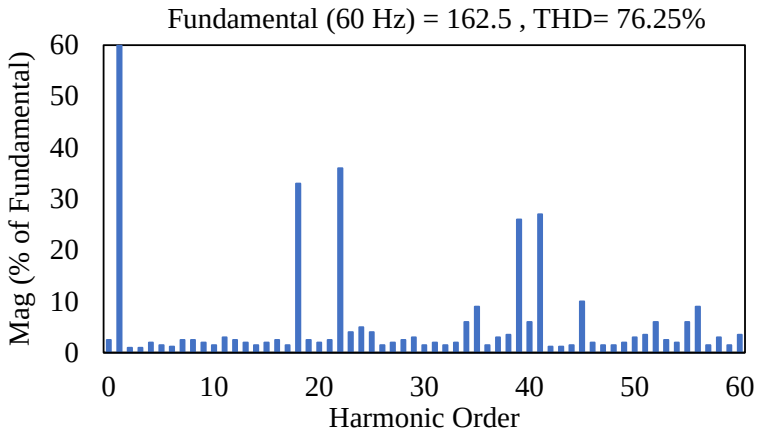

(b)

Fig. 2.2. Performance of SPWM in two–level VSI. (a) Line–to–line voltage. (b) Harmonic spectrum analysis (THD) on voltage waveform.

2.3 Space Vector Modulation

SVM technique is widely used in real–time and PMSM e–drive control due to its high feasibility in existing two–level VSI [9]–[11]. The development and mathematical modeling of the SVM algorithm are presented in this section.

2.3.1 Switching States in SVM

The two–level VSI consists of six power devices including three upper and three lower devices respectively, with a DC voltage source. Only one of the two power switches turns on in each phase, and hence there are eight combinations of on–off states which correspond to the different space vectors. Table 2.1 represents the space vectors and switching states in a two–level VSI where '1' and '0' denotes the upper and lower switch of the VSI respectively with the corresponding terminal voltage.

TABLE 2.1

SWITCHING STATES OF SVM

Space Vector		**Switching States**	**On–state switches**	**Vector Definition**
Zero Vector	$\vec{V}_0$	[111]	S_1, S_3, S_5	$\vec{V}_0 = 0$
		[000]	S_4, S_6, S_2	
Active Vectors	$\vec{V}_1$	[100]	S_1, S_6, S_2	$\vec{V}_1 = \frac{2}{3} V_{dc} e^{j0}$
	$\vec{V}_2$	[110]	S_1, S_3, S_2	$\vec{V}_2 = \frac{2}{3} V_{dc} e^{j\frac{\pi}{3}}$
	$\vec{V}_3$	[010]	S_4, S_3, S_2	$\vec{V}_3 = \frac{2}{3} V_{dc} e^{j\frac{2\pi}{3}}$
	$\vec{V}_4$	[011]	S_4, S_3, S_5	$\vec{V}_4 = \frac{2}{3} V_{dc} e^{j\frac{3\pi}{3}}$
	$\vec{V}_5$	[001]	S_4, S_6, S_5	$\vec{V}_5 = \frac{2}{3} V_{dc} e^{j\frac{4\pi}{3}}$
	$\vec{V}_6$	[101]	S_1, S_6, S_5	$\vec{V}_6 = \frac{2}{3} V_{dc} e^{j\frac{5\pi}{3}}$

2.3.2 *Space Vectors in SVM*

The space vector diagram of the SVM algorithm is shown in Fig. 2.3 where the active and zero switching states are represented by space vectors. The space vector represents a hexagon with all switching states in 6 sectors comprising of the active vectors ($\vec{V}_1$ to $\vec{V}_6$) and zero vector ($\vec{V}_0$).

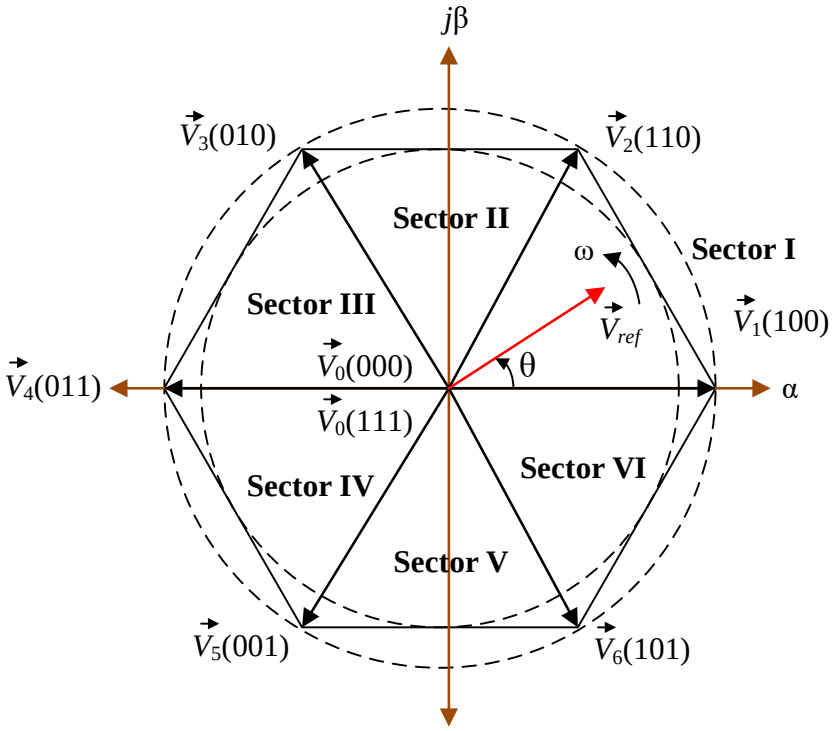

Fig. 2.3. Space vector in SVM algorithm in two–level VSI.

Considering a two–level VSI connected to a balanced three–phase load as in (2.1), the three–phase voltages (v_{AO}, v_{BO}, and v_{CO}) can be transformed into two–phase voltages (v_α and v_β) using Clarke transformation as represented in (2.2).

$$v_{AO}(t) + v_{BO}(t) + v_{CO}(t) = 0 \tag{2.1}$$

$$\begin{bmatrix} v_\alpha \\ v_\beta \end{bmatrix} = \frac{2}{3}\begin{bmatrix} 1 & -\frac{1}{2} & -\frac{1}{2} \\ 0 & \frac{\sqrt{3}}{2} & -\frac{\sqrt{3}}{2} \end{bmatrix}\begin{bmatrix} v_{AO}(t) \\ v_{BO}(t) \\ v_{CO}(t) \end{bmatrix} \tag{2.2}$$

The space vector can be represented in α–β plane using the two–phase voltages as shown below:

$$\vec{V}(t) = v_{\alpha}(t) + jv_{\beta}(t) \tag{2.3}$$

Substituting (2.2) in (2.3), we get

$$\vec{V}(t) = \frac{2}{3}[v_{AO}(t)e^{j0} + v_{BO}(t)e^{j2\pi/3} + v_{CO}(t)e^{j4\pi/3}] \tag{2.4}$$

where, $e^{ji} = \cos x + j \sin x$ and i = 0, 2π/3 and 4π/3 from (2.4). For example, for switching state $\vec{V}_1$[100], the load phase voltages can be represented as

$$\begin{cases} v_{AO}(t) = \frac{2}{3}V_{dc} \\ v_{BO}(t) = -\frac{1}{3}V_{dc} \\ v_{CO}(t) = -\frac{1}{3}V_{dc} \end{cases} \tag{2.5}$$

Hence by substituting (2.5) in (2.4) the corresponding space vector for each sector can be derived as in (2.6). A general representation for deriving the active space vectors ($\vec{V}_1$ to $\vec{V}_6$) is represented in (2.7), where i = 1,2, …, 6. The space vector definition for each switching state is illustrated in Table 2.1 using (2.7).

$$\vec{V}_1 = \frac{2}{3}V_{dc}e^{j0} \tag{2.6}$$

$$\vec{V}_i = \frac{2}{3}V_{dc}e^{j(i-1)\frac{\pi}{3}} \tag{2.7}$$

From Fig. 2.3 it can be noted that the reference vector ($\vec{V}_{ref}$) rotates and changes continuously in space whereas the zero and active vectors are stationary. The angular velocity (ω) of the reference vector ($\vec{V}_{ref}$) can be expressed as

$$\omega = 2\pi f \tag{2.8}$$

where f is the fundamental frequency of VSI output voltage. Further, the angular displacement (θ) of $\vec{V}_{ref}$ can be expressed as

$$\theta(t) = \int_0^t \omega(t)dt + \theta(0) \tag{2.9}$$

The switching states and the gate signals for the VSI can be generated from the $\vec{V}_{ref}$ using (2.8) and (2.9) applying the nearest three vector (N3V) scheme. The rotation of the $\vec{V}_{ref}$ facilitates different switches to turn on or off enabling the VSI output voltage to change over one cycle time. The amplitude and frequency of the $\vec{V}_{ref}$ corresponds to its magnitude and rotating speed, respectively.

2.3.3 Dwell Time Calculation

The on–state and off–state time, for example, the duty cycle time of a switch is represented by the dwell time during a sampling period T_s of the SVM scheme. The dwell time calculation for a given space vector is based on the fundamental 'volt–second balancing' principle, where the sum of voltage multiplied by time interval equals the product of the $\vec{V}_{ref}$ and T_s.

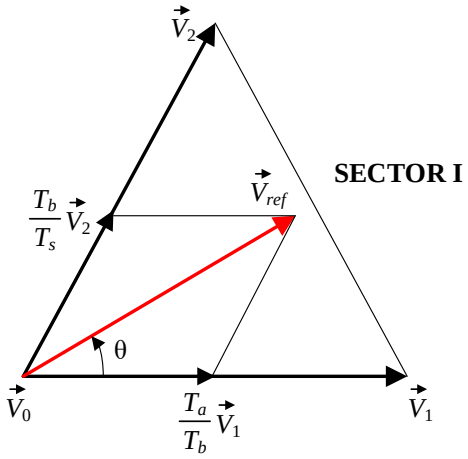

Fig. 2.4. $\vec{V}_{ref}$ in sector I due to $\vec{V}_1$, $\vec{V}_2$ and $\vec{V}_0$.

Assuming $\vec{V}_{ref}$ in the sector I with adjacent active and zero vectors as shown in Fig. 2.4, using the volt–second balancing equation the dwell times (T_a, T_b and T_0) can be interpreted as

$$\vec{V}_{ref} T_s = \vec{V}_1 T_a + \vec{V}_2 T_b + \vec{V}_0 T_0 \tag{2.10}$$

$$T_s = T_a + T_b + T_0 \tag{2.11}$$

The space vectors for the sector I in (2.10) are

$$\begin{aligned} \vec{V}_{ref} &= \vec{V}_{ref} e^{j\theta} \\ \vec{V}_1 &= \frac{2}{3} V_{dc} \\ \vec{V}_2 &= \frac{2}{3} V_{dc} e^{j\frac{\pi}{3}} \\ \vec{V}_0 &= 0 \end{aligned} \tag{2.12}$$

Substituting (2.12) in (2.11) and representing in the α–β plane,

$$\begin{aligned} \text{Re} : V_{ref} (\cos\theta) T_s &= \frac{2}{3} V_{dc} T_a + \frac{1}{3} V_{dc} T_b \\ \text{Im} : V_{ref} (\sin\theta) T_s &= \frac{1}{\sqrt{3}} V_{dc} T_b \end{aligned} \tag{2.13}$$

The dwell times T_a, T_b, and T_c in the sector I for $0 \le \theta \le \pi/3$ can be represented by solving (2.13) with (2.11) as

$$\begin{aligned} T_a &= \frac{\sqrt{3} T_s V_{ref}}{V_{dc}} \sin\left(\frac{\pi}{3} - \theta\right) \\ T_b &= \frac{\sqrt{3} T_s V_{ref}}{V_{dc}} \sin\theta \\ T_0 &= T_s - T_a - T_b \end{aligned} \tag{2.14}$$

Similarly, the expressions from (2.14) can be utilized to derive the dwell times values for different sectors. However, the angular displacement θ must be modified to ensure the new angular displacement θ*'* lies between zero and π/3. The relationship between the old and new angular displacement is expressed in (2.15) for $0 \le \theta' \le \pi/3$ where i = 1, 2, … ,6 for corresponding six sectors.

$$\theta' = \theta - (i-1)\frac{\pi}{3} \tag{2.15}$$

The relationship with the location of the $\vec{V}_{ref}$ and its corresponding dwell times is expressed in the following table.

TABLE 2.2

RELATIONSHIP BETWEEN $\vec{V}_{ref}$ LOCATION AND DWELL TIMES OF SVM

$\vec{V}_{ref}$ **Location**	$\theta = 0$	$0 \le \theta \le \frac{\pi}{6}$	$\theta = \frac{\pi}{6}$	$\frac{\pi}{6} < \theta < \frac{\pi}{3}$	$\theta = \frac{\pi}{3}$
Dwell Times	$T_a > 0$ $T_b = 0$	$T_a > T_b$	$T_a = T_b$	$T_a < T_b$	$T_a = 0$ $T_b > 0$

Considering the modulation index m_a, (2.14) can be further expressed as

$$\begin{aligned} T_a &= T_s m_a \sin\left(\frac{\pi}{3} - \theta\right) \\ T_b &= T_s m_a \sin\theta \\ T_0 &= T_s - T_a - T_b \end{aligned} \tag{2.16}$$

where,

$$m_a = \frac{\sqrt{3}V_{ref}}{V_{dc}} \tag{2.17}$$

$$0 \le m_a \le 1 \tag{2.18}$$

2.3.4 Switching Sequences of SVM

The selection of an appropriate switching sequence for the SVM scheme plays a key role in the efficient performance of VSI with reduced losses. The two fundamental criteria for designing of switching sequence are:

1. One switch is turned on and the other is turned off in one VSI leg during the switching of states
2. The transition of reference voltage from one sector to the next in the space vector does not require any minimum switching instances

The conventional switching sequence is derived in terms of seven segments of which the switching sequences for the sector I is represented in Fig. 2.5. Table 2.3 represents different switching sequences in all six sectors of the SVM scheme. It is observed that the switching of switches is based on the sampling period. Hence the switching frequency f_{sw} equals the sampling frequency f_{sp}.

$$f_{sw} = f_{sp} = \frac{1}{T_s} \tag{2.19}$$

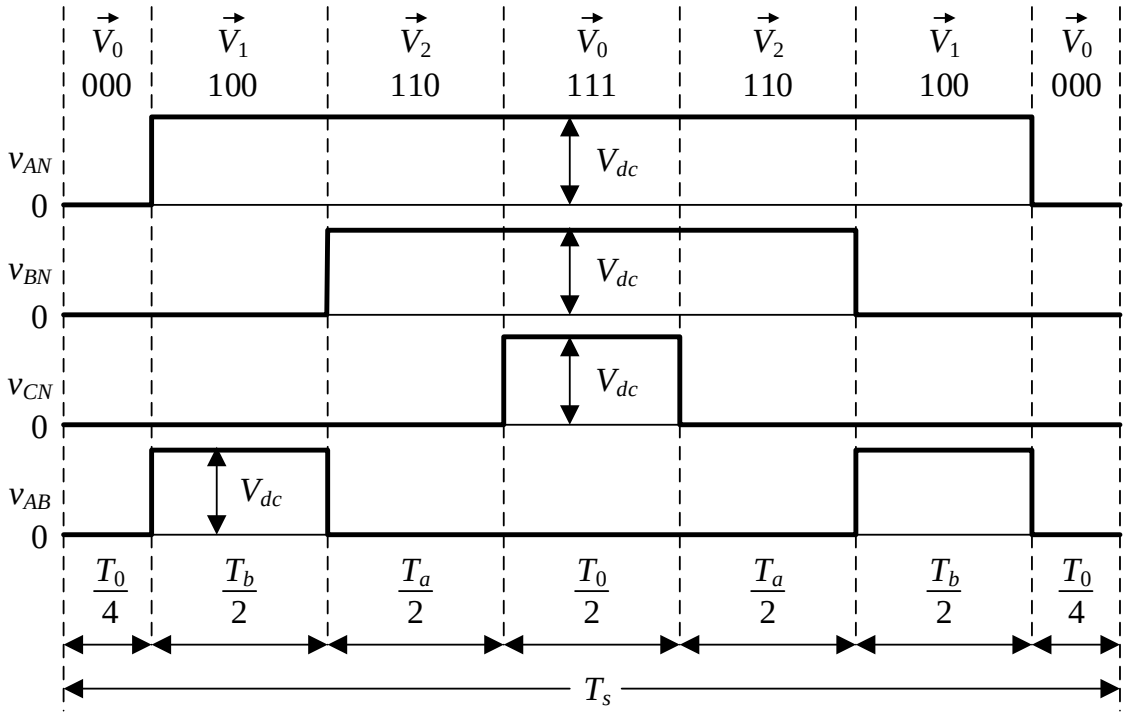

Fig. 2.5. Conventional switching sequence in sector I.

TABLE 2.3

CONVENTIONAL SWITCHING SEQUENCE

Sectors	**Switching Segments**						
	1	2	3	4	5	6	7
I	$\vec{V}_0$ [000]	$\vec{V}_1$ [100]	$\vec{V}_2$ [110]	$\vec{V}_0$ [111]	$\vec{V}_2$ [110]	$\vec{V}_1$ [100]	$\vec{V}_0$ [000]
II	$\vec{V}_0$ [000]	$\vec{V}_3$ [010]	$\vec{V}_2$ [110]	$\vec{V}_0$ [111]	$\vec{V}_2$ [110]	$\vec{V}_3$ [010]	$\vec{V}_0$ [000]
III	$\vec{V}_0$ [000]	$\vec{V}_3$ [010]	$\vec{V}_4$ [011]	$\vec{V}_0$ [111]	$\vec{V}_4$ [011]	$\vec{V}_3$ [010]	$\vec{V}_0$ [000]
IV	$\vec{V}_0$ [000]	$\vec{V}_5$ [001]	$\vec{V}_4$ [011]	$\vec{V}_0$ [111]	$\vec{V}_4$ [011]	$\vec{V}_5$ [001]	$\vec{V}_0$ [000]
V	$\vec{V}_0$ [000]	$\vec{V}_5$ [001]	$\vec{V}_6$ [101]	$\vec{V}_0$ [111]	$\vec{V}_6$ [101]	$\vec{V}_5$ [001]	$\vec{V}_0$ [000]
VI	$\vec{V}_0$ [000]	$\vec{V}_1$ [100]	$\vec{V}_6$ [101]	$\vec{V}_0$ [111]	$\vec{V}_6$ [101]	$\vec{V}_1$ [100]	$\vec{V}_0$ [000]

Since from Fig. 2.3, the $\vec{V}_{ref}$ in sector I and sector IV is 180° apart, the line–to–line voltage v_{AB} should be a mirror image to each other. Though this conventional switching sequence passes the fundamental design criteria, the conventional switching sequence of the SVM technique is not symmetrical which might lead to increased losses in VSI and drive. The symmetrical switching structure ensures reduced losses in VSI and smooth operation of the load. A time delay of $T_s/2$ is observed from the comparison of the line–to–line voltage v_{AB} of the VSI for both sector I and sector II respectively in Fig. 2.6.

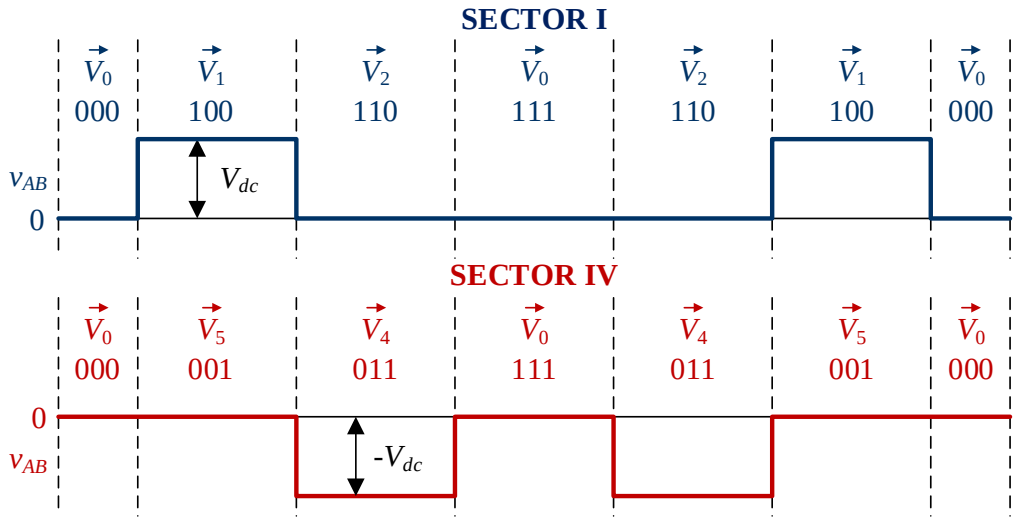

Fig. 2.6. Line–to–line voltage of sector I and IV using conventional switching sequence.

2.4 Modified SVM

To ensure symmetrical line–to–line voltage in the three–phase VSI, both the conventional and a modified switching sequence is used alternatively to generate the SVM signal in different locations of the $\vec{V}_{ref}$. The SVM diagram and switching sequence for the modified SVM are illustrated in Fig. 2.7, and Table 2.4, respectively. This SVM scheme further aids in reduced losses and enhanced performance of the VSI.

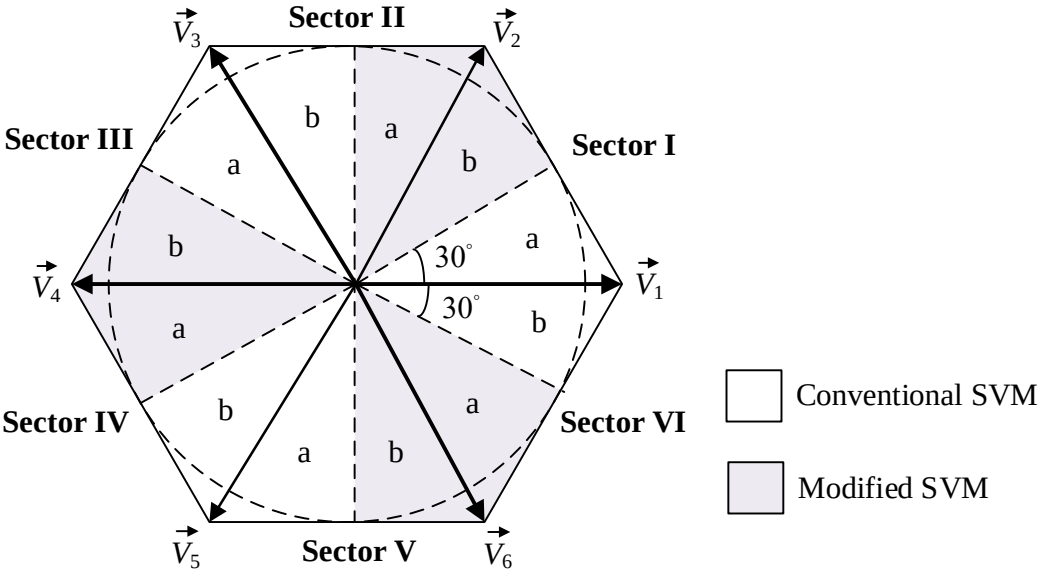

Fig. 2.7. Space vector diagram with two switching sequence.

TABLE 2.4

TWO SWITCHING SEQUENCE FOR MODIFIED SVM

Sectors	**Switching Sequence**						
I–a	$\vec{V}_0$ [000]	$\vec{V}_1$ [100]	$\vec{V}_2$ [110]	$\vec{V}_0$ [111]	$\vec{V}_2$ [110]	$\vec{V}_1$ [100]	$\vec{V}_0$ [000]
I–b	$\vec{V}_0$ [111]	$\vec{V}_2$ [110]	$\vec{V}_1$ [100]	$\vec{V}_0$ [000]	$\vec{V}_1$ [100]	$\vec{V}_2$ [110]	$\vec{V}_0$ [111]
II–a	$\vec{V}_0$ [111]	$\vec{V}_2$ [110]	$\vec{V}_3$ [010]	$\vec{V}_0$ [000]	$\vec{V}_3$ [010]	$\vec{V}_2$ [110]	$\vec{V}_0$ [111]
II–b	$\vec{V}_0$ [000]	$\vec{V}_3$ [010]	$\vec{V}_2$ [110]	$\vec{V}_0$ [111]	$\vec{V}_2$ [110]	$\vec{V}_3$ [010]	$\vec{V}_0$ [000]
III–a	$\vec{V}_0$ [000]	$\vec{V}_3$ [010]	$\vec{V}_4$ [011]	$\vec{V}_0$ [111]	$\vec{V}_4$ [011]	$\vec{V}_3$ [010]	$\vec{V}_0$ [000]
III–b	$\vec{V}_0$ [111]	$\vec{V}_4$ [011]	$\vec{V}_3$ [010]	$\vec{V}_0$ [000]	$\vec{V}_3$ [010]	$\vec{V}_4$ [011]	$\vec{V}_0$ [111]
IV–a	$\vec{V}_0$ [111]	$\vec{V}_4$ [011]	$\vec{V}_5$ [001]	$\vec{V}_0$ [000]	$\vec{V}_5$ [001]	$\vec{V}_4$ [011]	$\vec{V}_0$ [111]
IV–b	$\vec{V}_0$ [000]	$\vec{V}_5$ [001]	$\vec{V}_4$ [011]	$\vec{V}_0$ [111]	$\vec{V}_4$ [011]	$\vec{V}_5$ [001]	$\vec{V}_0$ [000]
V–a	$\vec{V}_0$ [000]	$\vec{V}_5$ [001]	$\vec{V}_6$ [101]	$\vec{V}_0$ [111]	$\vec{V}_6$ [101]	$\vec{V}_5$ [001]	$\vec{V}_0$ [000]
V–b	$\vec{V}_0$ [111]	$\vec{V}_6$ [101]	$\vec{V}_5$ [001]	$\vec{V}_0$ [000]	$\vec{V}_5$ [001]	$\vec{V}_6$ [101]	$\vec{V}_0$ [111]
VI–a	$\vec{V}_0$ [111]	$\vec{V}_6$ [101]	$\vec{V}_1$ [100]	$\vec{V}_0$ [000]	$\vec{V}_1$ [100]	$\vec{V}_6$ [101]	$\vec{V}_0$ [111]
VI–b	$\vec{V}_0$ [000]	$\vec{V}_1$ [100]	$\vec{V}_6$ [101]	$\vec{V}_0$ [111]	$\vec{V}_6$ [101]	$\vec{V}_1$ [100]	$\vec{V}_0$ [000]

Incorporating the modified SVM algorithm, symmetrical line–to–line voltage v_{AB} is achieved. A comparison of the line–to–line voltage v_{AB} in sector I and sector IV is represented in Fig. 2.8.

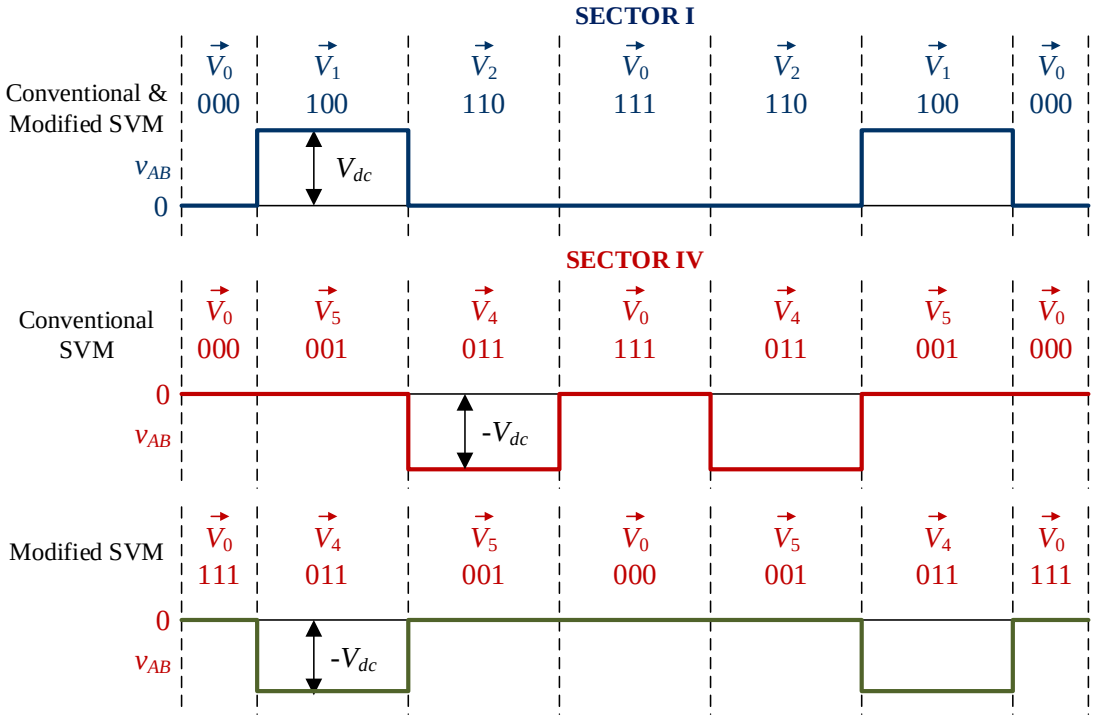

Fig. 2.8. Comparison of line–to–line voltage of sector I and IV using conventional and modified SVM.

The simulation of the proposed modified SVM scheme is simulated with a three–phase two–level VSI in MATLAB Simulink as shown in Fig. 2.1. The modulation waveform of the SVM waveform at m_a equals 0.85 is presented in Fig. 2.9. Table 2.5 represents the simulation specifications.

TABLE 2.5

SIMULATION SPECIFICATIONS FOR MODIFIED SVM

Switching frequency, f_{sw}	20,000 Hz
Sample Time, T_s	5×10^{-5} s
DC–link voltage (V_{dc})	325 V

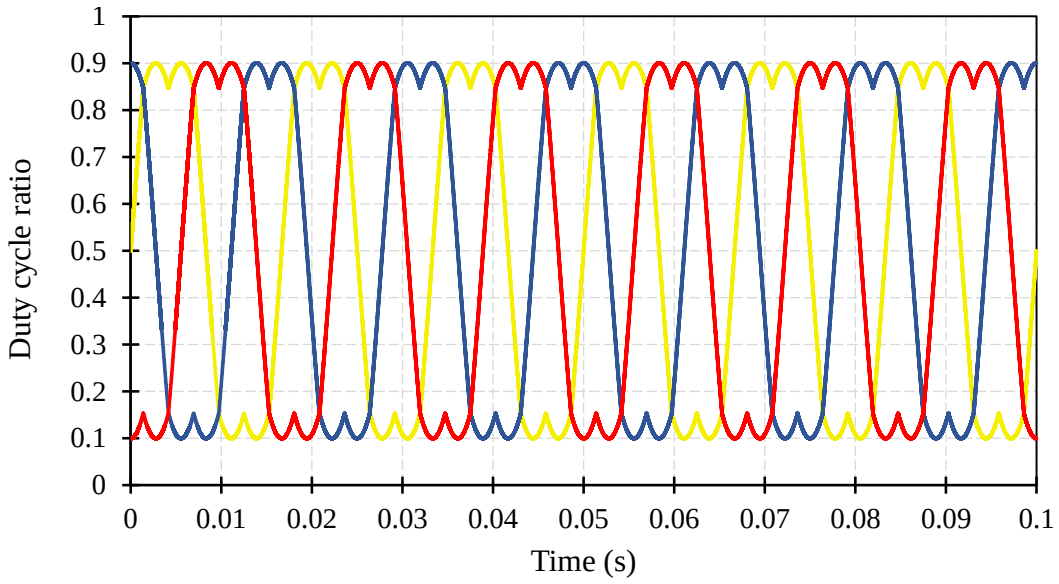

Fig. 2.9. Simulation result of the modulation waveform from modified SVM scheme in three–phase VSI; v_{mA} (yellow), v_{mB} (blue), and v_{mC} (red).

The Simulink result for three–phase line–to–line and line–to–ground voltage for the first leg of VSI is shown in Figs. 2.10 and 2.11, respectively. All the other legs of the VSI represent the same corresponding waveforms with a phase shift of 120°.

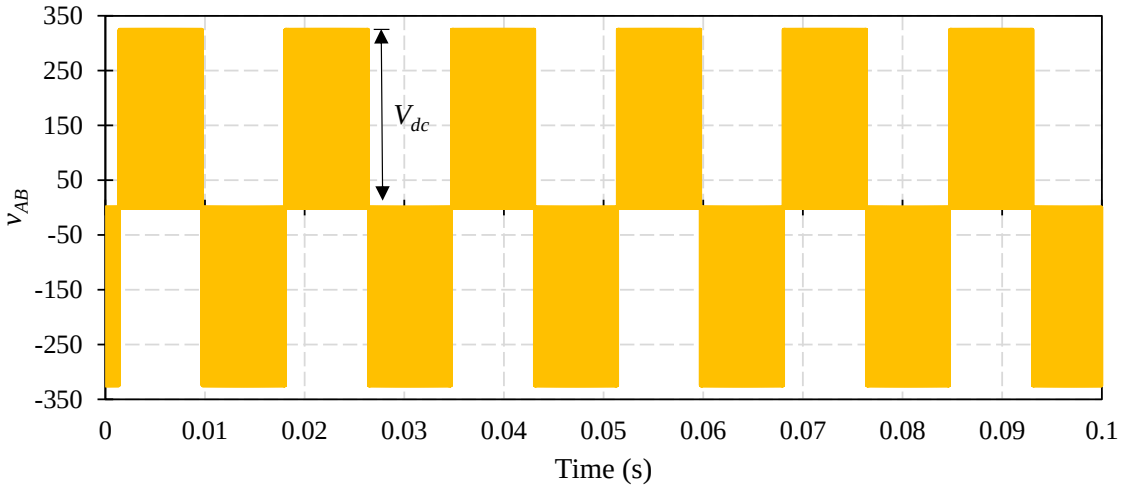

Fig. 2.10. Simulated line–to–line voltage of VSI.

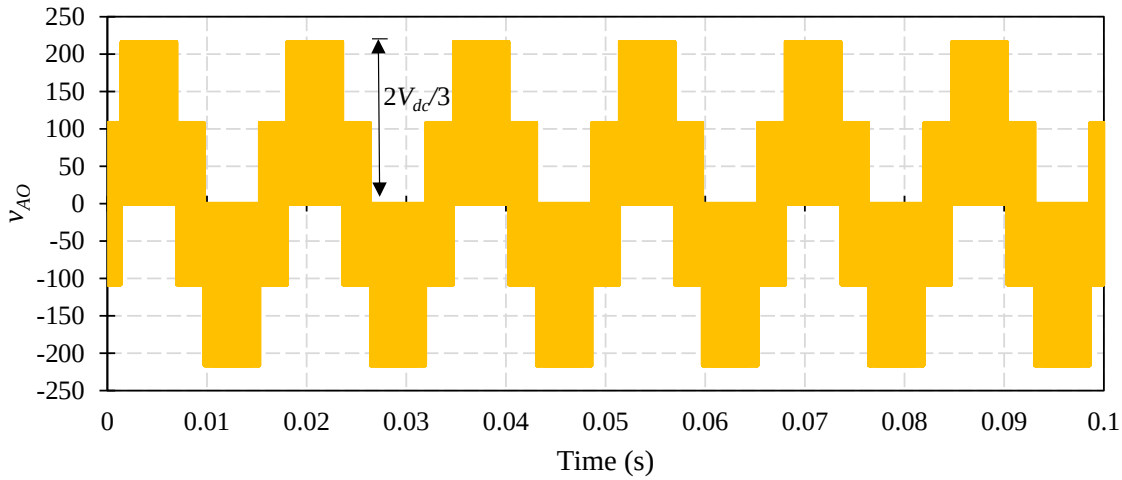

Fig. 2.11. Simulated line–to–ground voltage of VSI.

Equation (2.19) relates an indirect relationship between switching frequency (f_{sw}) and sample time (T_s). Hence the implementation of the modified SVM at high switching frequency using low–cost 150 MHz DSP in WBG–based inverter becomes challenging. Hence a soft computing methodology for the modified SVM algorithm is proposed in chapter 3.

2.5 References

[1] Y. Jiao, F. C. Lee, and S. Lu, "Space Vector Modulation for Three–Level NPC Converter with Neutral Point Voltage Balance and Switching Loss Reduction," *IEEE Trans. Power Electronics*, vol. 29, no. 10, pp. 5579–5591, Oct. 2014.

[2] A. M. Hava and E. Ün, "Performance Analysis of Reduced Common– Mode Voltage PWM Methods and Comparison with Standard PWM Methods for Three–Phase Voltage–Source Inverters," *IEEE Trans. Power Electronics*, vol. 24, no. 1, pp. 241–252, 2009.

[3] X. Zhang, X. Wu, C. Geng, X. Ping, S. Chen, and H. Zhang, "An Improved Simplified PWM for Three-Level Neutral Point Clamped Inverter Based on Two-Level Common-Mode Voltage Reduction PWM," *IEEE Trans. Power Electronics*, vol. 35, no. 10, pp. 11143-11154, Oct. 2020.

[4] O. López, D. Dujic, M. Jones, F. D. Freijedo, J. Doval-Gandoy, and E. Levi, "Multidimensional Two-Level Multiphase Space Vector PWM Algorithm and Its

Comparison with Multifrequency Space Vector PWM Method," *IEEE Trans. Industrial Electronics*, vol. 58, no. 2, pp. 465-475, Feb. 2011.

[5] M. A. Al-Hitmi, S. Moinoddin, A. Iqbal, K. Rahman, and M. Meraj, "Space Vector vs. Sinusoidal Carrier-Based Pulse Width Modulation for a Seven-Phase Voltage Source Inverter," *CPSS Trans. Power Electronics and Applications*, vol. 4, no. 3, pp. 230-243, Sept. 2019.

[6] R. A. Villarreal-Ortiz, M. Hernandez-Angeles, C. R. Fuerte-Esquivel, and R. O. Villanueva-Chavez, "Centroid PWM Technique for Inverter Harmonics Elimination," *IEEE Trans. Power Delivery*, vol. 20, no. 2, pp. 1209-1210, April 2005.

[7] J. W. Kolar, T. Friedli, J. Rodriguez, and P. W. Wheeler, "Review of Three-Phase PWM AC–AC Converter Topologies," *IEEE Trans. Industrial Electronics*, vol. 58, no. 11, pp. 4988-5006, Nov. 2011.

[8] W. Liang, P. C. Luk, and W. Fei, "Investigation of Magnetic Field Interharmonics and Sideband Vibration in the FSCW IPMSM Drive with the SPWM Technique," *IEEE Trans. Power Electronics*, vol. 33, no. 4, pp. 3315-3324, April 2018.

[9] B. Wu and M. Narimani, “Two-Level Voltage Source Inverter,” in *High-Power Converters and AC Drives*, 2nd ed., Wiley-IEEE Press, 2017, ch. 6, pp. 95-100.

[10] B. K. Bose, “Voltage-Fed Converters,” in *Modern Power Electronics and AC Drives*, PH PTR, 2001, ch. 5, pp. 210-239.

[11] M. A. Hannan, J. A. Ali, A. Mohamed, and M. N. Uddin, "A Random Forest Regression Based Space Vector PWM Inverter Controller for the Induction Motor Drive," *IEEE Trans. Industrial Electronics*, vol. 64, no. 4, pp. 2689–2699, April 2017.

CHAPTER 3

ARTIFICIAL NEURAL NETWORK BASED IMPROVED MODULATION STRATEGY FOR GaN INVERTER

3.1 Introduction

For EVs, high power density and high efficiency of the electric powertrain (e–drive) are important to achieve extended driving range. Therefore, it is essential to focus on improving the inverter further. Different topologies of the inverter have been proposed to reduce harmonics distortion and diminish the overall loss of the inverter. New technology power switches such as Silicon Carbide (SiC) MOSFET, Gallium Nitride (GaN) have been developed and improved for high switching frequency operation compared to traditional IGBTs and MOSFETs to reduce losses in the inverter. The new generation WBG switches are capable of switching at 50 kHz and above with greater efficiency compared to existing Si devices [1]–[3].

The performance and efficiency of the voltage source inverter (VSI) depend on the switching control scheme. Hence, an efficient modulation strategy for switching of power switches is necessary to achieve wide modulation range, high frequency and minimum loss of power converters [4]. Over time, different modulation techniques such as sinusoidal PWM, specific harmonic elimination PWM, SVM, carrier–based PWM have been developed to reduce the loss of the converter and improve the overall performance of the drive. Among other control strategies, SVM control is best suited for high switching frequency, reduced harmonics distortion, reduced switching loss, and current ripple [5].

In general, due to algorithm complexity, SVM leads to complex computation during real–time implementation in motor drive. The SVM algorithm requires complex trigonometric functions, coordinate transformations, vector decomposition to sectors, dwell time calculations and so on, all of which require high digital signal processor (DSP) memory and cost a lot of CPU resources. Due to the requirement of additional memory, the operation of the drive at high switching frequency is compromised thereby reducing the accuracy of the SVM. This leads to increased harmonics which reduces the overall performance of the system.

To mitigate this issue, a genetic algorithm (GA) based SVM is used [6]. However, the GA uses a repetitive iteration method to find the minimum cost function, which is time–consuming. Some new implementation methods are also promoted without multiplier and divider, which simplifies the complex calculation of dwell time [7]. In [8], a fuzzy logic controller has been used to implement the algorithm. However, it has been observed that these controllers are not very efficient and accurate which reduces the efficiency of the converter. Also, for a complex system like this with non–linear equations and complicated dynamic performance, deriving analytical equations with reduced computation time is complex and tedious. Intelligent controllers such as neural networks (NN) are an alternative solution. The neural network (NN) based SVM shows promising results with significant improvement in the performance [9]–[10]. Effective training can precisely map the input(s) with the desired output(s) at any point in time over a varied range of operating conditions.

3.2 Neural Network

An artificial neural network (ANN) is a computing system with neurons/nodes that are designed together to imitate the human brain. The fundamental concept of ANN is the learning ability by interpreting knowledge or data for future use. In addition to the learning ability, ANN also can easily generalize information with tolerance towards uncertain noise. Mathematically ANNs are collections of computational units integrating matrices and transfer functions to emulate the biological brain. The learning on neural networks (NNs) is achieved by iterating the weight and bias matrices to an optimal value with a reduced mean square error [11].

An ANN is an augmented form of machine learning (ML) for high precision and complex target output. Hence the NN has the added advantage of high processing speed during a real–time implementation with rapid prediction and prototyping. To minimize the complex online computation and improve the efficiency of the drive, this chapter introduces a state–of–the–art NN–based improved SVM control for high switching e–drive. A supervised ANN is trained offline with batch data and is deployed for real–time implementation in an embedded platform. In the following sections, the different designs and training methods of NN–based SVM are introduced.

3.3 Architecture of Neuron Model

A basic neuron model comprises multiple inputs with weights and bias to generate the optimal output. The structure of a neuron model is shown in Fig. 3.1.

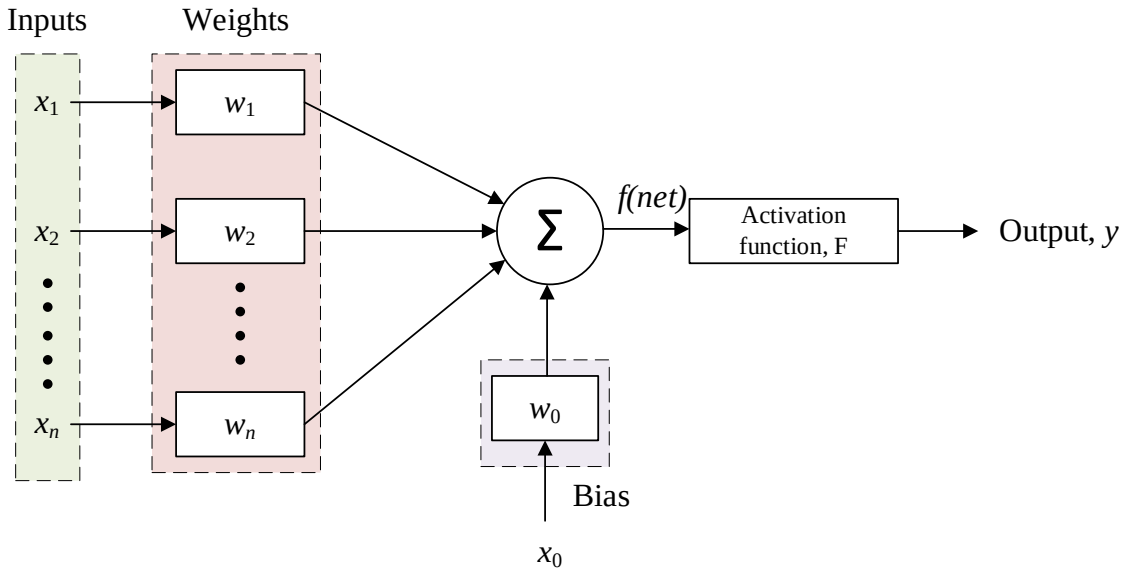

Fig. 3.1. Structure of neuron model.

The individual output is derived from inputs with weights and bias. Mathematically, Fig. 3.1 can be interpreted as

$$f(net) = \sum_{i=1}^{n} w_n \cdot x_n + w_0 \cdot x_0 \tag{3.1}$$

$$y = F(f(net)) \tag{3.2}$$

A neural network consists of many neuron models together to replicate the human brain. A learning algorithm is used to train the NNs for effective memorization and generalization. In general, the architecture of NN can be classified into three main types:

1. Single–layer Feed Forward Perceptron: As the name states, it has one input layer and an output layer. The input is multiplied with the weights and is directly sent to the output layer

2. Multi–layer Neural Network: This type of NNs have multiple layers termed as hidden layers. Multiple hidden layers enable enhanced memorization and generalization capability of the NN. Multi–layer NN can be further classified as a feedforward or feedback network
3. Recurrent Neural Network: A NN with one or more feedback is termed as a recurrent NN. The output of the NN is fed to the input for improved predictions

3.4 Artificial Neural Network Based SVM

An improved space vector modulation (SVM) is used with the neural network–based approach to incorporate real–time implementation in GaN inverter. The improved NN modulation strategy uses the modified SVM method from chapter 2 which incorporates the minimum number of switching instances in each switching cycle with the appropriate symmetrical pulse sequence. With the unique capability of an NN, just like a trained human brain, the proposed network predicts the most precise output instantaneously over a wide operating range.

3.4.1 NN Structure

The proposed NN based real–time approach for the SVM is implemented using a feed–forward multi–layer network. The structure of the NN is shown in Fig. 3.2. The NN consists of three different layers, namely an input layer (*i*), a hidden layer (*j*), and an output layer (*k*). The input layer comprises two inputs, namely V_α and V_β, in a matrix derived from the three–phase voltage (V_a, V_b, and V_c) using Clark's transformation. The output layer consists of the target matrix variable – T_a, T_b, and T_0. Hence, the number of nodes in the input, hidden and the output layer is 2–20–3 respectively. This NN structure yields stronger memorization and generalization ability over a varied range of input parameters.

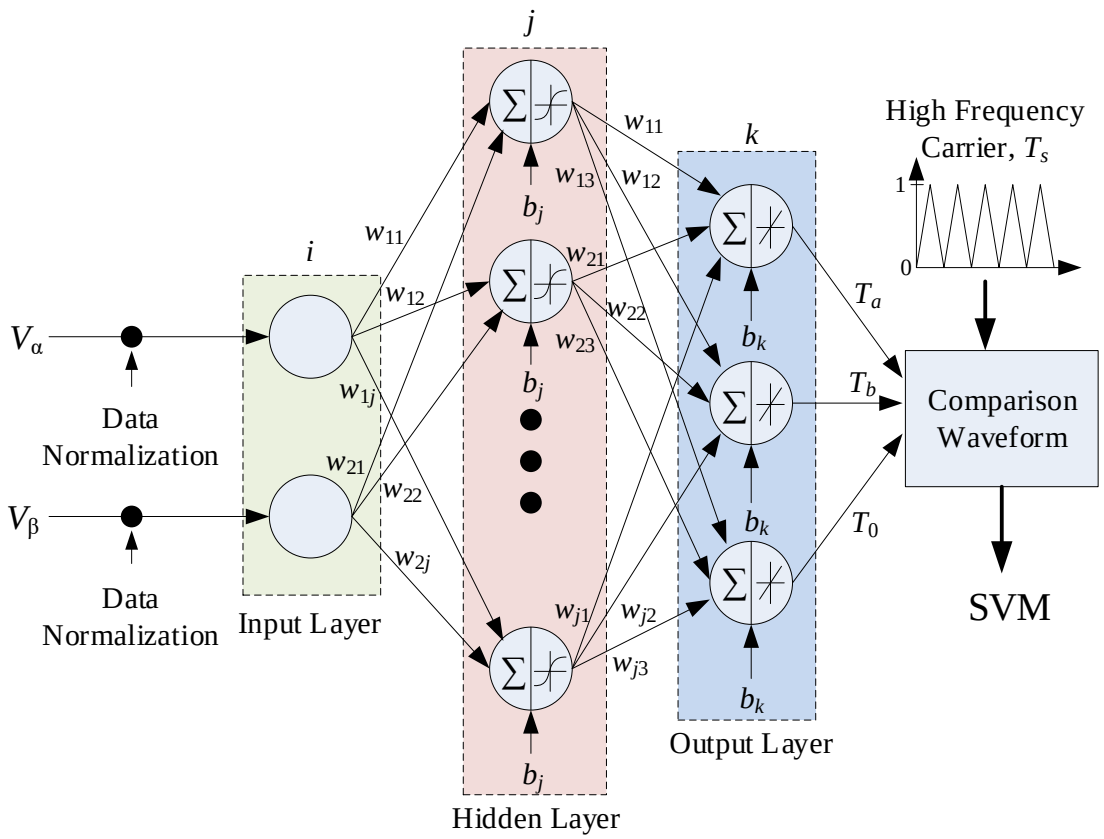

Fig. 3.2. Proposed structure of ANN–based SVM.

The two inputs V_α and V_β are first pre–processed and added with values termed as weight (w) and biases (b) using the proposed training algorithm. The input is then computed using the tangent–sigmoid activation functions in the hidden layer and further processed using the linear transfer functions to get the final output from the output layer. Equations (3.3) and (3.4) show the hidden and output layer responses respectively, where x_i, i = 1, 2 is the NN input values (V_α and V_β) and j = 1, 2, …, 20 is output from the hidden layer.

$$f(net_j) = \frac{2}{1 + e^{-2*\sum_{j=1}^{n} w_{ij} x_i + b_j}} \tag{3.3}$$

$$f(net_k) = \sum_{k=1}^{3} w_{jk} f(net_j) + b_k \tag{3.4}$$

3.4.2 NN Training and Learning Methodology

The learning algorithm plays a key role in the development and training of the neural network. Generally, the learning methodology can be classified into three main categories:

1. Supervised learning
2. Unsupervised learning
3. Reinforcement learning

The ANN–based modified SVM is trained by supervised learning methodology using the backpropagation technique in MATLAB Simulink. An advanced and improved Levenberg–Marquardt algorithm has been developed and is used to optimize the NN to overcome the complex computation and storage costs. The workflow of the modified Levenberg–Marquardt algorithm is shown in Fig. 3.3. The Levenberg–Marquardt is a method for approximation of complex functions consisting of solving (3.5) and (3.6).

$$\left(J^t J + \lambda I\right)\delta = J^t E \tag{3.5}$$

where J is the Jacobian matrix of the system, λ is the damping factor, δ is the weight update vector and E is the output error vector for each input vector used on training the network. The term J^tJ matrix is also referred to as the approximated Hessian matrix (H) and J^tE is termed as the error gradient (g). The improved Levenberg–Marquardt training algorithm uses a Bayesian framework by introducing Bayesian hyperparameters, which improves the learning of the neural network to prevent overfitting of data. These hyperparameters, in Table 3.1, improve the network weight selection and further aids the learning process the network seeks. This slows the downhill progression but also speeds up the convergence rate near the solution. The cost function, $C(k)$ of the proposed network is expressed in (3.6).

$$C(k) = \beta E_k + \alpha E_w \tag{3.6}$$

where alpha (α) and beta (β) are the hyperparameters, E_k is the sum of mean squared errors and E_w is the squared weight errors.

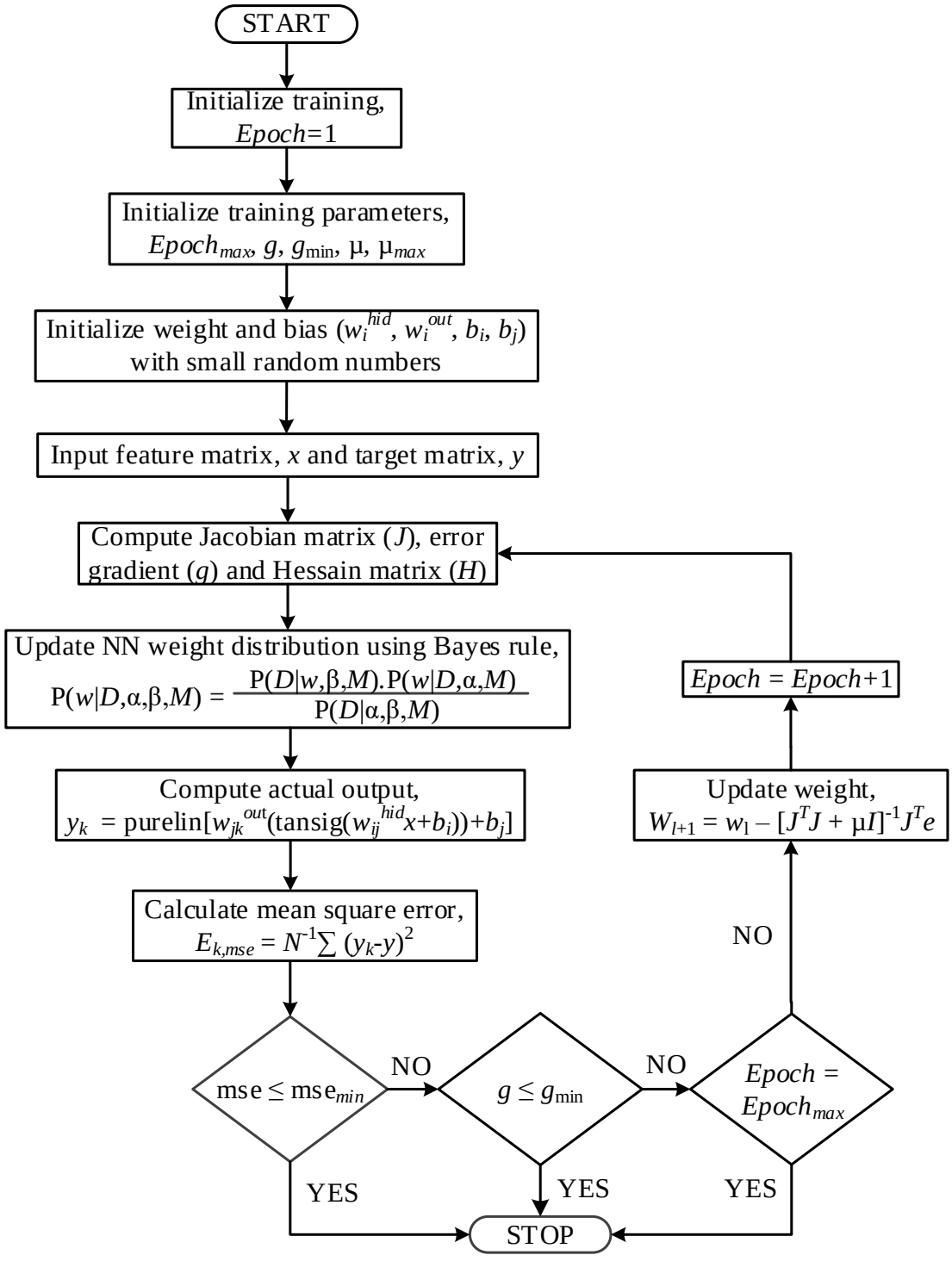

Fig. 3.3. Improved Levenberg–Marquardt training algorithm.

TABLE 3.1

NN TRAINING HYPERPARAMETERS

Hyperparameters	**Values**
Maximum Epoch ($Epoch_{max}$)	1,000
Epoch	1,000
Minimum gradient	1.00×10^{-7}
Gradient	1.3813×10^{-6}
Learning rate (μ)	0.005
Mini–batch size, N	64

The output of the NN is shown in (3.7) which is obtained from (3.3) and (3.4). The optimum hidden layer of the network is obtained through iteration with respect to the least mean square error (*mse*) as shown in (3.8).

$$y_k = \text{purelin}\left[w_{jk}^{out}\left(\text{tansig}\left(w_{ij}^{hid}x+b_i\right)\right)+b_j\right] \tag{3.7}$$

where tansig and purelin are the activation functions of the hidden and output layer, w_{ij}^{hid} and b_i are weight and biases of the hidden layer and w_{jk}^{out} and b_j are weight and biases of the output layer, respectively.

$$E_{k,mse}(Y \mid w, M) = \frac{1}{N}\sum_{k=1}^{N}(y_k - y)^2 \tag{3.8}$$

where Y is the training matrix with the input target pair, M is the NN architecture with its metrics, y^k is the predicted output of the network and y is the target output. To prevent overtraining and overfitting of the NN, the training process terminates if any of the following conditions are met:

i. Mean square error is less than or equal to the target mean square error ($mse_{\min}$)

ii. Error gradient is less than or equal to the target error gradient (g_{min}), and

iii. Epoch is equal to the maximum epoch ($Epoch_{max}$)

3.5 Implementation and Experimental Setup

The proposed ANN–based modified SVM is implemented in a low–cost 150 MHz digital signal processor (DSP). Initially, the performance and output of the NN–based control is tested and verified in the DSP docking kit. Fig. 3.4 represents the TMS320F28335 DSP with the docking kit and Fig. 3.5 represents the testing of PWM generation.

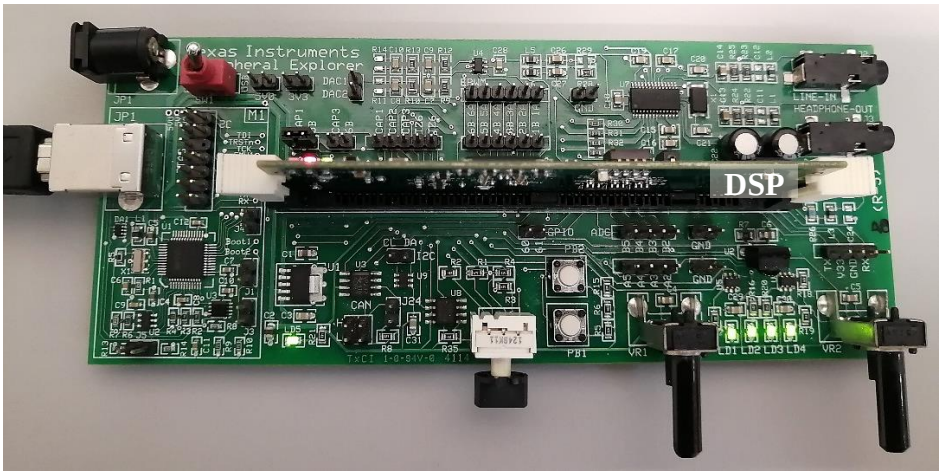

Fig. 3.4. TI docking kit with DSP for testing.

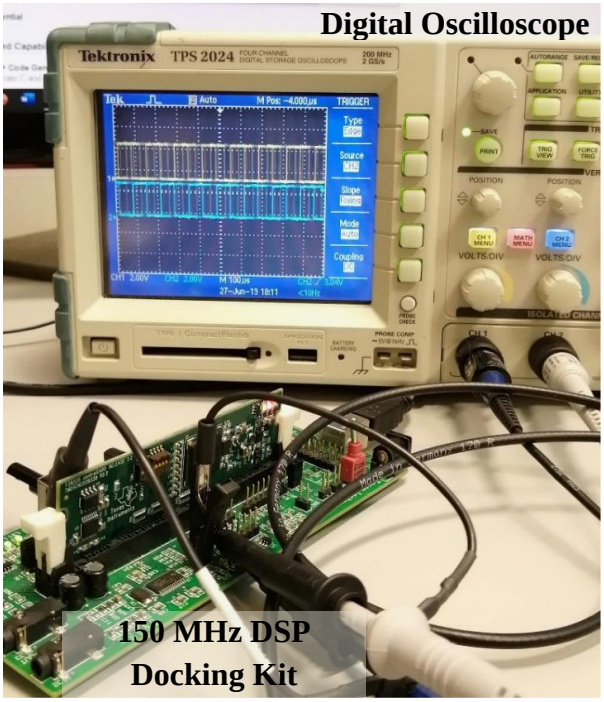

Fig. 3.5. Validation of SVM generation using DSP docking kit.

Due to the space constraint in the GaN–based power–dense inverter faster method of digital voltage source protection is implemented in the 150 MHz DSP card. The phase currents (i_A, i_B, and i_C) are sensed using the ADC sensor to leverage the protection algorithm. The digital implementation of the protection algorithm enables reduced PWM trip latency time during fault occurrence compared to hardware circuit–based protection. The algorithm is tested using the 150 MHz DSP docking kit and the output is presented in Fig. 3.6.

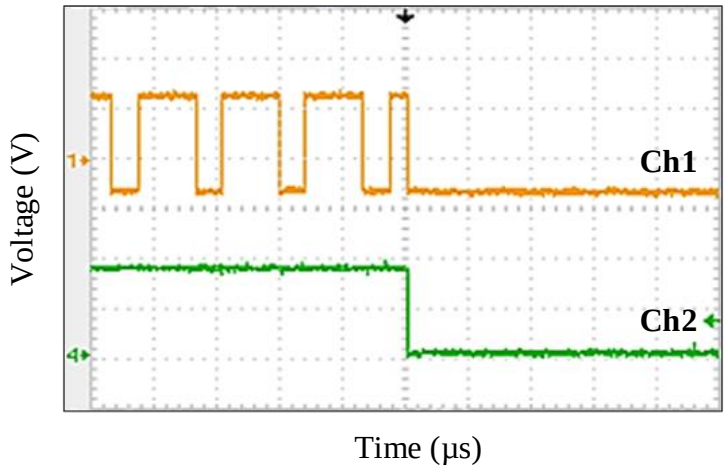

Fig. 3.6. Testing of PWM trip latency: Ch1= ANN–based PWM waveform (5 V/div.); Ch2= PWM enable signal (2 V/div.); x–axis= Time (25 µs/div).

The proposed NN–based control algorithm is simulated in MATLAB Simulink embedded platform and experimentally validated using a 5 kW GaN inverter with an *R–L* load and DSP at a very low sample period to evaluate the stability of the proposed control. The schematic diagram of the prototype is shown in Fig. 3.7. The control gate pulse of the GaN inverter is generated using the proposed control algorithm. The prototyped GaN inverter test bench is shown in Fig. 3.8. The proposed NN–based improved SVM is implemented at 50 kHz switching frequency with 300 ns deadtime. The detailed specification of the GaN inverter test bench is presented in Table 3.2.

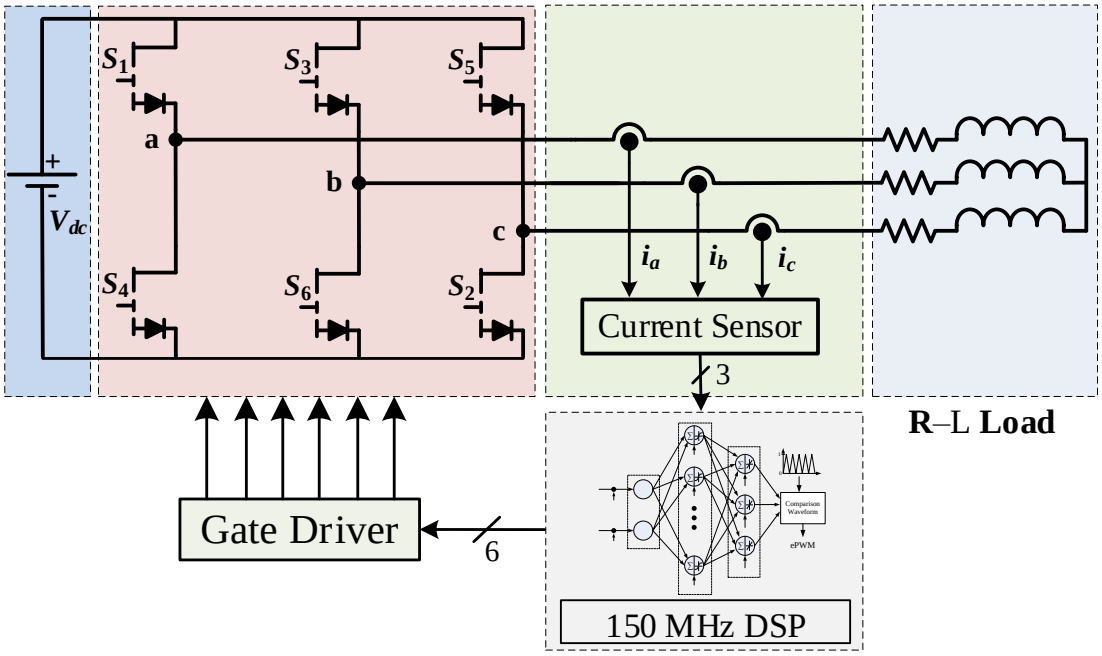

Fig. 3.7. Schematic diagram of experimental setup with NN–SVM.

TABLE 3.2

TEST BENCH SPECIFICATIONS

Parameters	**Values**
Inverter technology	WBG–based GaN device
GaN E–HEMT module	GS66516B
V_{GS}	–3 V to +6 V
Inverter rated power	5 kW
DSP	TMS320F28335
ANN–SVM switching frequency	50,000 Hz
Deadtime	300 ns
Efficiency	87.1%
Cooling technology	Liquid

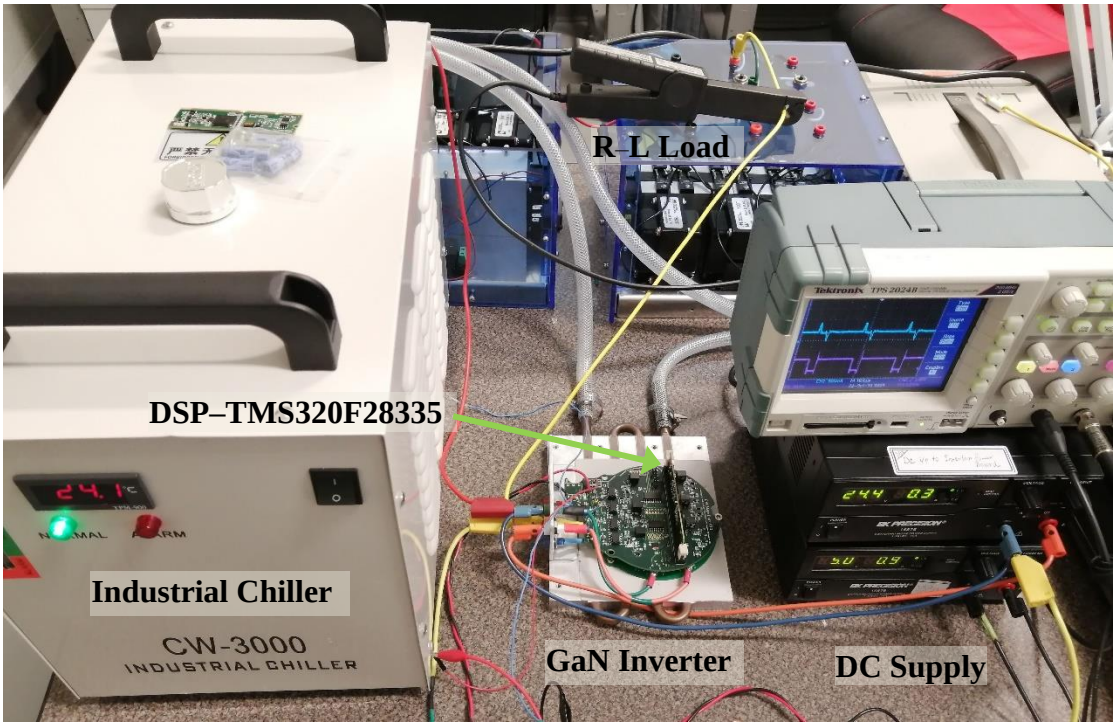

Fig. 3.8. Experimental test bench for GaN inverter.

3.6 Results on Improved ANN–Based Modified SVM Strategy

The performance of the proposed ANN–based improved SVM is investigated and validated using MATLAB Simulink, PSIM, and a laboratory GaN inverter. The performance results are discussed as follows.

3.6.1 Performance Test of Proposed NN

This analysis provides the performance of the NN after its training. The NN is evaluated with unknown test data under varying voltage and switching frequency to understand the generalization capability with the mean square error. The cost function from equation (3.6) and the mean square error (*mse*) from equation (3.8) is used to calculate the best fit of the NN. The performance graph of the NN over the 1,000 epochs is shown in Fig. 3.9. The highlighted point in Fig. 3.9 indicates the least *mse* of the NN at 1,000 epochs. The *mse* is 2.5188×10^{-7} which is very small and is acceptable for the control algorithm. The gate pulse across the top and bottom device from the experimental test bench is shown in Fig. 3.10.

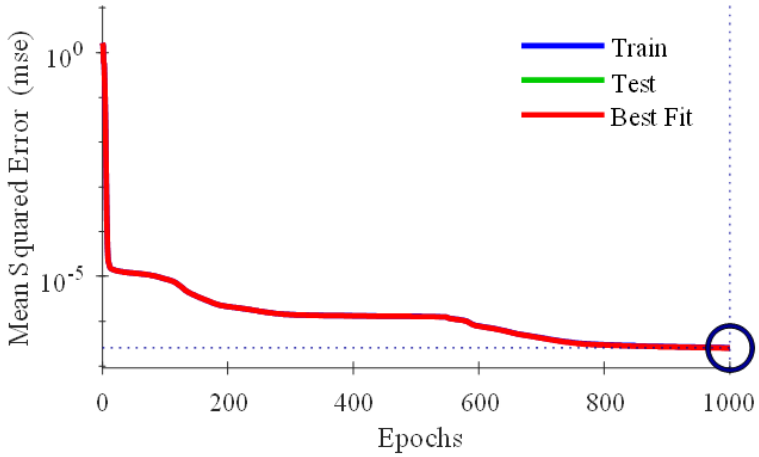

Fig. 3.9. Performance plot of NN–based SVM with 1,000 epochs.

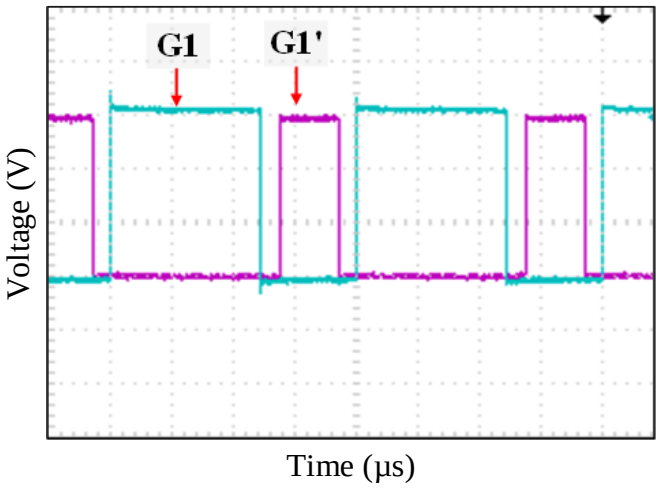

Fig. 3.10. Gate Pulse, V_{GS} in GaN inverter test bench: y–axis=Voltage across top (G1) and bottom (G1') switch (3 V/div.); x–axis= Time (5 µs/div.).

3.6.2 Regression Test of Proposed NN–Based SVM

The regression plot shows the accuracy of the NN under training and testing conditions. Fig. 3.11 evaluates the regression plot for the modulating SVM signal with the best fit curve. The NN regression value is 0.99997 which is very close to 1, indicating a good generalization ability of the proposed NN.

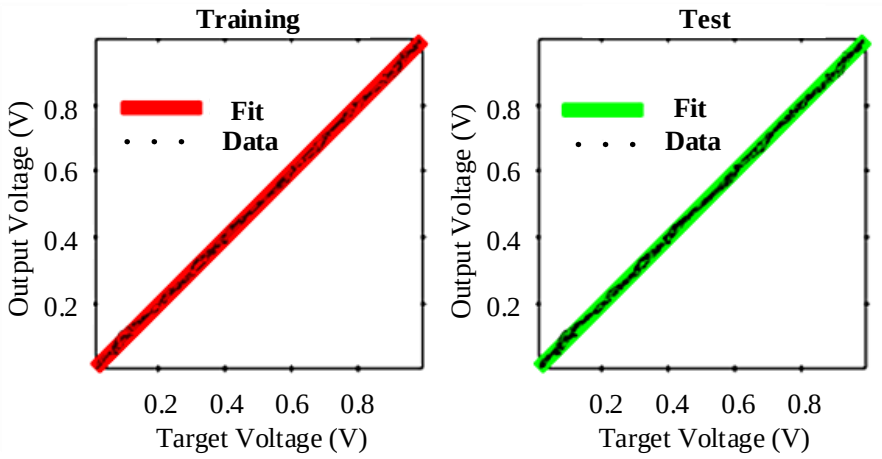

Fig. 3.11. Regression plot for output voltage vs target voltage. (a) NN training results. (b) NN test results.

3.6.3 Computation Time Impact at High–Frequency Operation

The major challenge in the GaN inverter with the low–cost DSP is to achieve high processing speed of the complex algorithm during high switching frequency operation with reduced computation time. The computation time for one cycle real–time simulation of conventional SVM at 50 kHz switching frequency is 12.518 s and that of NN based modified SVM is 1.644 s. Due to the strong memorization and generalization ability of the proposed NN, the time complexity of NN–SVM is significantly reduced as compared to modified SVM as shown in Fig. 3.12. Further the NN–SVM has less computation time compared to the genetic algorithm (GA) based fuzzy logic control.

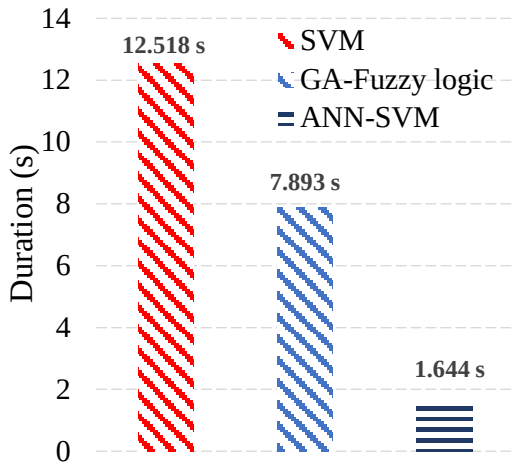

Fig. 3.12. Profiling of computation time for one cycle real–time simulation.

3.6.4 Loss Analysis of GaN Inverter

The GaN E–HEMT module is simulated in PSIM and co–simulated with MATLAB Simulink to analyze the switching loss of the GaN inverter. The loss analysis is performed using both control algorithms. The modified SVM uses an improved nearest three vector (N3V) based scheme which reduces switching losses by reducing the number of switching instances with proper pulse sequence alignment. The result shown in Fig. 3.13 indicates that the switching loss is minimized in the proposed NN–based control algorithm which further improves the efficiency of the GaN inverter.

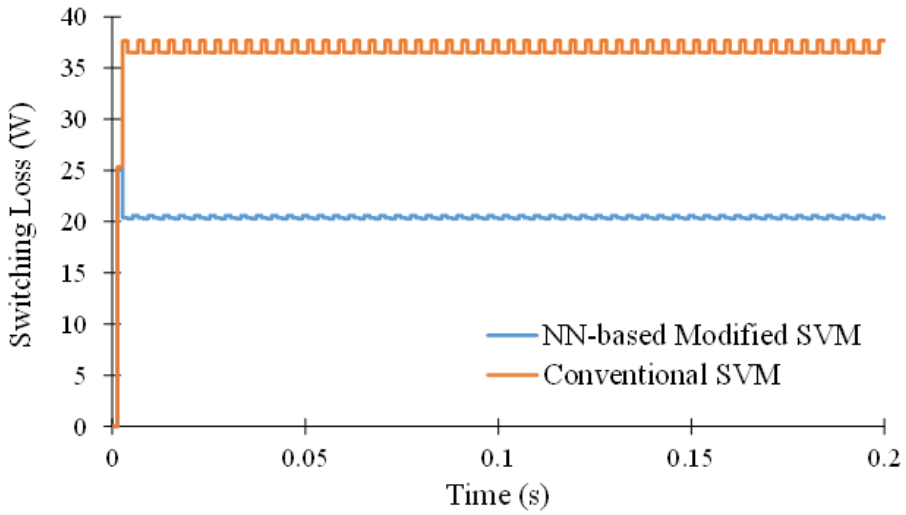

Fig. 3.13. Switching loss with conventional and ANN–based modified SVM.

3.7 References

[1] J. Millán, P. Godignon, X. Perpiñà, A. Pérez–Tomás, and J. Rebollo, "A Survey of Wide Bandgap Power Semiconductor Devices," *IEEE Trans. Power Electronics*, vol. 29, no. 5, pp. 2155–2163, May 2014.

[2] K. Shirabe *et al*., "Efficiency Comparison Between Si–IGBT–Based Drive and GaN–Based Drive," *IEEE Trans. Industry Applications*, vol. 50, no. 1, pp. 566–572, Jan.–Feb. 2014.

[3] E. A. Jones, F. F. Wang, and D. Costinett, "Review of Commercial GaN Power Devices and GaN–Based Converter Design Challenges," *IEEE Journal of Emerging and Selected Topics Power Electronics*, vol. 4, no. 3, pp. 707–719, Sept. 2016.

[4] Y. Jiao, F. C. Lee, and S. Lu, "Space Vector Modulation for Three–Level NPC Converter with Neutral Point Voltage Balance and Switching Loss Reduction," *IEEE Trans. Power Electronics*, vol. 29, no. 10, pp. 5579–5591, Oct. 2014.

[5] A. M. Hava and E. Ün, "Performance Analysis of Reduced Common–Mode Voltage PWM Methods and Comparison with Standard PWM Methods for Three–Phase Voltage–Source Inverters," *IEEE Trans. Power Electronics*, vol. 24, no. 1, pp. 241–252, 2009.

[6] K. L. Shi and Hui Li, "Optimized PWM Strategy Based on Genetic Algorithms," *IEEE Trans. Industrial Electronics*, vol. 52, no. 5, pp. 1458–1461, Oct. 2005.

[7] Z. Shu, J. Tang, Y. Guo, and J. Lian, "An Efficient SVPWM Algorithm with Low Computational Overhead for Three–Phase Inverters," *IEEE Trans. Power Electronics*, vol. 22, no. 5, pp. 1797–1805, 2007.

[8] M. A. Hannan *et al*., "A Quantum Lightning Search Algorithm–Based Fuzzy Speed Controller for Induction Motor Drive," *IEEE Access*, vol. 6, pp. 1214–1223, 2018.

[9] M. A. Hannan, J. A. Ali, A. Mohamed, and M. N. Uddin, "A Random Forest Regression Based Space Vector PWM Inverter Controller for the Induction Motor Drive," *IEEE Trans. Industrial Electronics*, vol. 64, no. 4, pp. 2689–2699, April 2017.

[10] M. Balasubramonian and V. Rajamani, "Design and Real–Time Implementation of SHEPWM in Single–Phase Inverter Using Generalized Hopfield Neural Network," *IEEE Trans. Industrial Electronics*, vol. 61, no. 11, pp. 6327–6336, Nov. 2014.

[11] S. S. Haykin, "Multilayer Perceptron," *Neural Networks: A Comprehensive Foundation*, 2nd ed., Pearson, 1998, ch. 4, pp. 178-227.

CHAPTER 4

MATHEMATICAL MODELING OF PMSM AND VECTOR CONTROL STRATEGIES FOR E–DRIVE

4.1 Introduction

This chapter introduces the development of the mathematical model of PMSM. Based on the position of the permanent magnet (PM) and rotor, PMSMs are further categorized as surface–mounted PMSMs (non–salient pole) and interior PMSMs (salient pole) [1]–[4]. The dynamic model of interior PMSM is further used to derive the conventional vector control strategy by decoupling the flux and torque linkage. The interior PMSM model with its control strategy is developed and the need for an intelligent control strategy is investigated.

4.2 Dynamics of IPMSM

The interior PMSM (IPMSM) model represents a multivariable, dynamic, and non–linear mathematical system. To simplify the development of the IPMSM mathematical model, the following assumptions are made:

1. The core saturation of IPMSM including losses such as copper loss, iron loss, and eddy current loss is considered negligible and hence ignored
2. The damper winding in the rotor is neglected
3. Sinusoidal back EMF
4. Balanced three–phase voltage supply

The model of IPMSM is derived from the rotor reference frame since it is independent of stator voltage and current [5]. This means that the direct and quadrature reference axes of the stator rotate at the same speed as that of rotor speed. The conventional PMSM model is derived from *abc* parameters using Park transformations [6]. Considering the time–varying motor parameters, the stator voltage equation in the rotor reference can be derived from (4.1).

$$\begin{pmatrix} v_d \\ v_q \end{pmatrix} = \begin{pmatrix} R_s + L_d.\dfrac{d}{dt} & -\omega_e L_q \\ \omega_e L_d & R_s + L_q.\dfrac{d}{dt} \end{pmatrix} \begin{pmatrix} i_d \\ i_q \end{pmatrix} + \begin{pmatrix} 0 \\ \omega_e \lambda_m \end{pmatrix} \tag{4.1}$$

Solving (4.1) we get,

$$\begin{cases} v_d = R_s i_d + L_d \dfrac{di_d}{dt} - \omega_e L_q i_q \\ v_q = R_s i_q + L_q \dfrac{di_q}{dt} + \omega_e L_d i_d + \omega_e \lambda_m \end{cases} \tag{4.2}$$

where v_d, v_q, i_d, and i_q are the stator voltage and current of dq frame; R_s is the stator winding resistance; L_d and L_q are d–axis and q–axis inductance of stator and rotor; ω_e is the electrical angular speed; and λ_m is the flux linkage of the PMSM. The torque balance equation of the PMSM is

$$\begin{cases} \dfrac{d}{dt}\omega_m = \dfrac{1}{J}\left(\tau_{em} - \tau_f - \tau_L\right) \\ \tau_f = B\omega_m \end{cases} \tag{4.3}$$

where J is the inertia, B is the friction coefficient, ω_m is the rotor mechanical speed, τ_f is the friction torque, and τ_L is the load torque. Further, the electromagnetic torque, T_e of the IPMSM is expressed based on motor design. For surface PMSM (SPMSM) and interior PMSM (IPMSM) the electromagnetic torque equation can be further expressed in (4.4) and (4.5) respectively, where P denoted the number of pole pairs in PMSM.

$$T_e = \frac{3}{2} P\left(\lambda_m i_q\right) \tag{4.4}$$

$$T_e = \frac{3}{2} P\left[\lambda_m i_q + \left(L_d - L_q\right) i_d i_q\right] \tag{4.5}$$

From (4.2) and (4.5), $\omega_e L_q i_q$ and $-\omega_e L_d i_d$ are the dynamic coupling terms for IPMSM associated with non–linear time–varying parameters. Also, the stator q–axis voltage is associated with the dynamic non–linear EMF term $-\omega_e \lambda_m$. The block diagram of the

mathematical IPMSM model is shown in Fig. 4.1 [7]. A laboratory IPMSM motor is used for simulation and validation of the control techniques as discussed in upcoming sections. The detailed specification for the IPMSM is represented in Table 4.1.

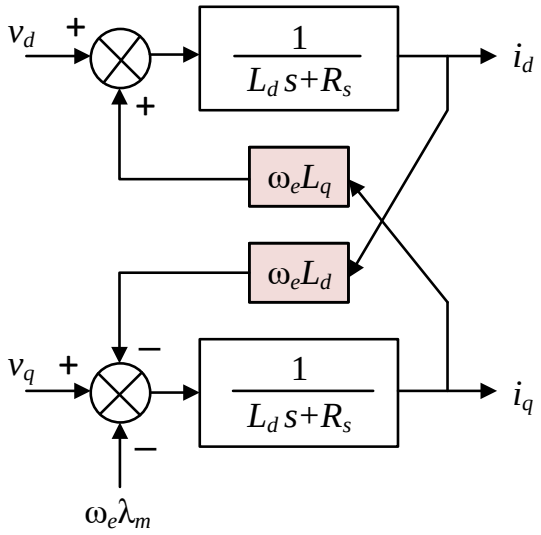

Fig. 4.1. Block diagram of IPMSM mathematical model.

4.3 Vector Control in IPMSM

The conventional vector control also termed as field–oriented control (FOC) of IPMSM incorporates two nested PI controllers for stator current and rotor speed control. An outer control loop is used for rotor speed control of the IPMSM drive. An inner control loop is implemented for *d*–axis and *q*–axis current tracking and control which generates the reference voltage vector (v_d and v_q) for the IPMSM drive. The mathematical model of IPMSM from (4.1) to (4.5) is used to develop the transfer function of the system to design the adaptive speed and current PI controllers. The FOC is further categorized as follows.

4.3.1 Zero d–axis Control

This is the conventional FOC where the reference *d*–axis current is kept zero to keep the direction of the magnet's magnetic field aligned with the *d*–axis [8]–[11]. The implementation of this control strategy is simple and is mainly used in SPMSM by establishing linear torque–current characteristics. The *q*–axis stator current is used to produce the motor's electromagnetic torque. The block diagram of zero *d*–axis control is

TABLE 4.1

IPMSM MOTOR PARAMETERS

Parameters	Values
Pole Pairs, P	4
Rated Power	4.25 kW
Rated Current, $I_{rms/phase}$	11 A
Maximum Current, I_{max}	15.55 A
Rated Speed	575 rpm
Maximum Speed	5,100 rpm
Permanent Magnet Flux Linkage, λ_m	0.61 Wb
Inductance in q–axis, L_q	65.78×10^{-3} H
Inductance in d–axis, L_d	30.45×10^{-3} H
Stator Resistance, R_s	1 Ohm
Inertia, J	0.0375 kg.m^2
Friction coefficient, B	1
DC–link voltage, V_{dc}	450 V
Switching frequency	10,000 Hz

shown in Fig. 4.2. However, due to reduced torque output capability, this control strategy is not used in IPMSM.

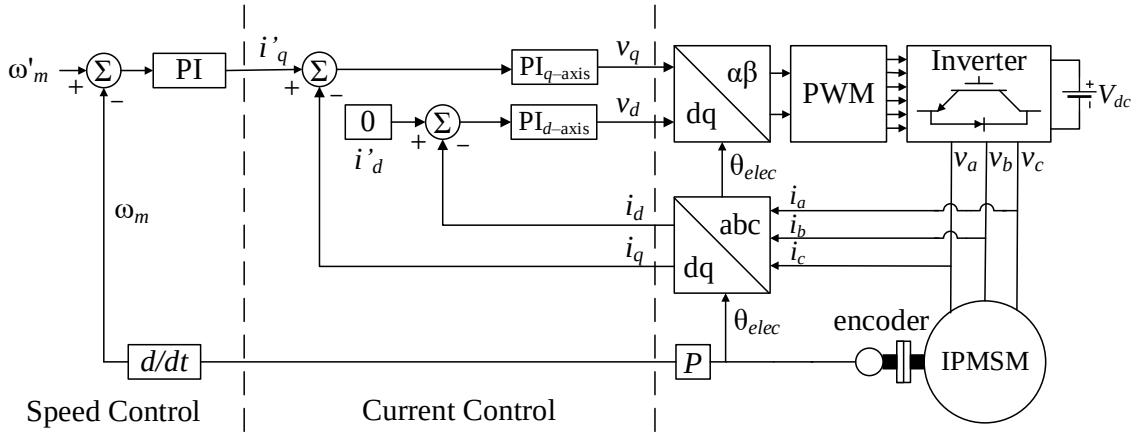

Fig. 4.2. Block diagram of FOC with zero d–axis control.

4.3.2 Maximum Torque per Ampere and Flux Weakening Control

The saliency of the rotor magnetic circuit in IPMSM causes an increased L_q/L_d ratio resulting in reluctance torque in the rotor. The maximum torque per ampere (MTPA) control utilizes the reluctance torque to generate more torque at lower operating speed. Hence with the same stator current, the motor can be operated at optimal values of i_d and i_q resulting in increased efficiency with minimized stator current losses [9]–[10]. The reference torque T_{ref} from the speed controller is used to calculate the maximum reference current i_m as in (4.6).

$$i_m = \frac{2T_{ref}}{3P\lambda_m} \tag{4.6}$$

The MTPA algorithm in e–drive is used to generate the reference i_d and i_q using (4.7) and (4.8) respectively.

$$i_d = \frac{\lambda_m}{4\left(L_d - L_q\right)} - \sqrt{\frac{\lambda_m^2}{16(L_q - L_d)^2} + \frac{i_m^2}{2}} \tag{4.7}$$

$$i_q = \sqrt{i_m^2 - i_d^2} \tag{4.8}$$

The maximum speed of IPMSM is governed by its base speed with its stator voltage, back emf, and rated current. As this operation becomes complex due to increased back emf, the flux weakening control algorithm is used to control the motor beyond the base speed. To operate the motor beyond the base speed, the rotor flux linkage is reduced by reducing i_d to a more negative value. The reference i_d and i_q under the flux weakening region are determined by solving the following equations.

$$i_d = \frac{-\lambda_m L_d + \sqrt{\left(\lambda_m L_d\right)^2 - \left(L_d^2 - L_q^2\right)\left(\lambda_m^2 + L_q^2 i_m^2 - \frac{v_m^2}{\omega_e^2}\right)}}{\left(L_d^2 - L_q^2\right)} \tag{4.9}$$

$$i_q = \sqrt{i_m^2 - i_d^2} \tag{4.10}$$

The block diagram of FOC with MTPA and flux weakening control is shown in Fig. 4.3. The characteristics of the IPMSM under MTPA and flux weakening control is illustrated in Fig. 4.4 [10]–[11].

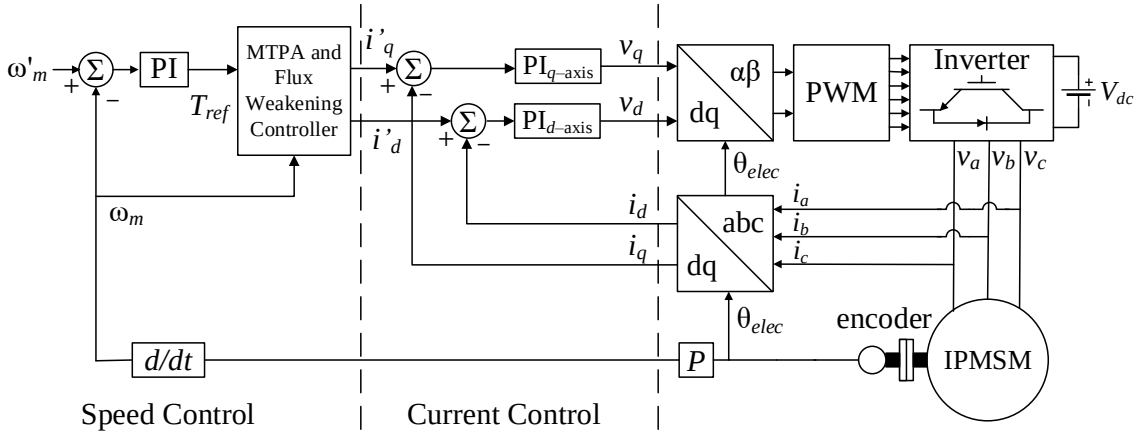

Fig. 4.3. Block diagram of FOC with MTPA and flux weakening control.

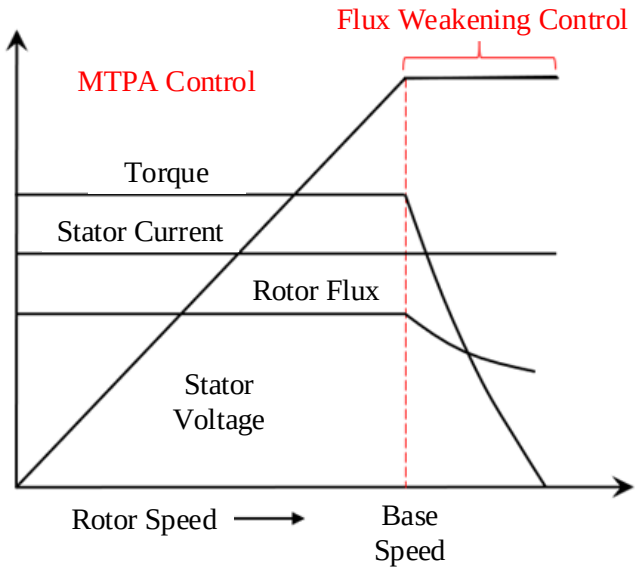

Fig. 4.4. IPMSM characteristics under MTPA and flux weakening control.

4.4 Design of Adaptive PI Controller for FOC

The adaptive PI parameters for tuning of the speed–loop controller is derived from the motor transfer function to track the desired reference torque. The optimal proportional constant K_p and integral constant K_i are represented with overall compensator formula C

of the PI controller in (4.11). Equation (4.12) represents the reference torque T_{ref} output from the speed–loop PI controller.

$$C = \frac{J\pi f_{sw}}{75P\lambda_m} + \frac{B\pi f_{sw}}{75P\lambda_m}\frac{1}{s} \tag{4.11}$$

$$T_{ref} = C(\omega' - \omega) \tag{4.12}$$

where ω' is the reference rotor speed and ω is the actual rotor speed of PMSM.

The current control in PMSM plays an integral role in stator current and torque control. Traditionally, coupled PI controllers are used to eliminate tracking errors in *d*–axis and *q*–axis loop as in (4.13),

$$\begin{cases} e_d = i_d^{'} - i_d \\ e_q = i_q^{'} - i_q \end{cases} \tag{4.13}$$

where e_d and e_q are the tracking errors in direct axis and quadrature axis, respectively; i'_d and i'_q are the reference *d*– and *q*–axis current; and i_d and i_q are the actual *d*– and *q*–axis stator currents. The proportional (P) and integral parameters (I) of the adaptive PI controller are tuned from the IPMSM transfer functions which include the IPMSM time–varying parameters to eliminate the tracking errors of the stator current, e_d and e_q. Two coupled PI controllers are used for tracking the *d*–axis and *q*–axis currents and to generate the reference IPMSM stator voltage vector v_d and v_q, as in (4.14) and (4.15) respectively [12].

$$v_d = \left[\left(\frac{2\pi L_d f_{sw}}{10}\right) + \left(\frac{2\pi R_s f_{sw}}{10}\right)T_s \frac{1}{z-1}\right] e_d \tag{4.14}$$

$$v_q = \left[\left(\frac{2\pi L_q f_{sw}}{10}\right) + \left(\frac{2\pi R_s f_{sw}}{10}\right)T_s \frac{1}{z-1}\right] e_q \tag{4.15}$$

4.5 Performance Evaluation and Needs for Intelligent Controller

The adaptive PI controller is tested on the experimental test bench shown in Fig. 4.5 to understand the transient and dynamic behaviors of the IPMSM. Current control

performance is evaluated by loading the motor using a speed–controlled dynamometer and rotating the motor at a constant speed. The adaptive PI controllers are used to track the *d*– and *q*– axis currents. A real–time OPAL–RT controller is used for rapid control prototyping (RCP) of the control algorithm with an IGBT based inverter. The current angle, γ_{MTPA} is varied at each maximum current, and the current tracking response is evaluated.

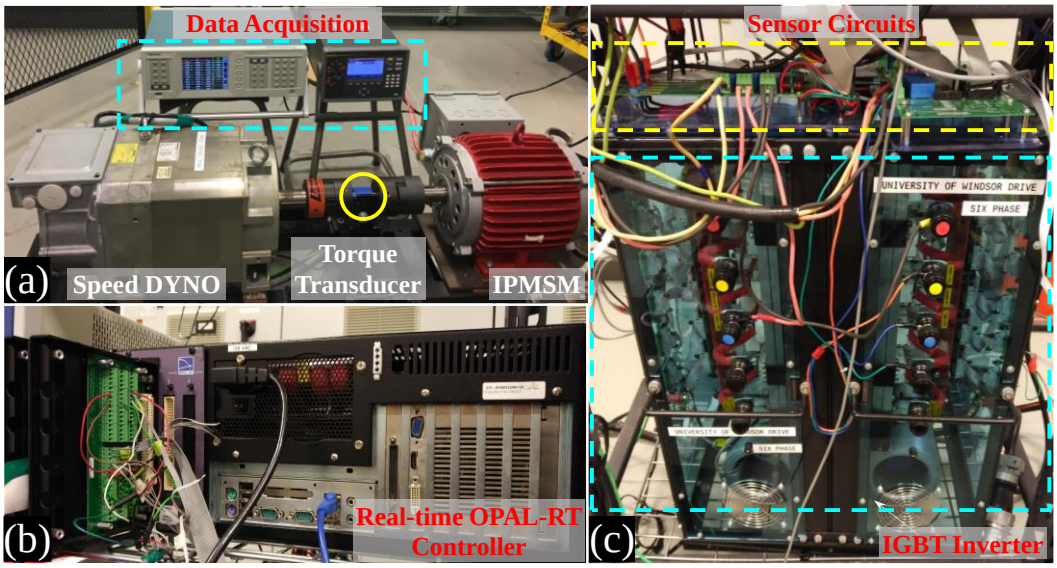

Fig. 4.5. Experiment test bench with adaptive PI controller. (a) IPMSM dyno setup. (b) Real–time OPAL–RT used as controller. (c) IGBT inverter.

Remark 1: Under the dynamic conditions, it is observed that the IPMSM inductances L_d and L_q and magnet flux linkage λ_m change due to the saturation and temperature change respectively, further imposing challenges in accurate *dq* current and voltage tracking [13]–[15]. The inductance varies between 20% and the flux linkage varies up to 20% under different loading conditions and temperature conditions. These changes affect the performance of the adaptive PI control and the overall system.

Remark 2: The transient peaks due to the decoupling inaccuracy of the adaptive PI controller are also observed. The dynamic *dq* current tracking of the adaptive PI controller is shown in Fig. 4.6. This figure demonstrates the transient overshoot in the direct axis due to the change in current in the quadrature axis at 6 s. Similarly, a transient peak is observed in the quadrature axis due to a change of current in the direct axis at 10.25 s. The transient

overshoot is due to the IPMSM coupling terms $\omega_e L_q i_q$ and $-\omega_e L_d i_d$, and hence the decoupling inaccuracy of the adaptive PI controller.

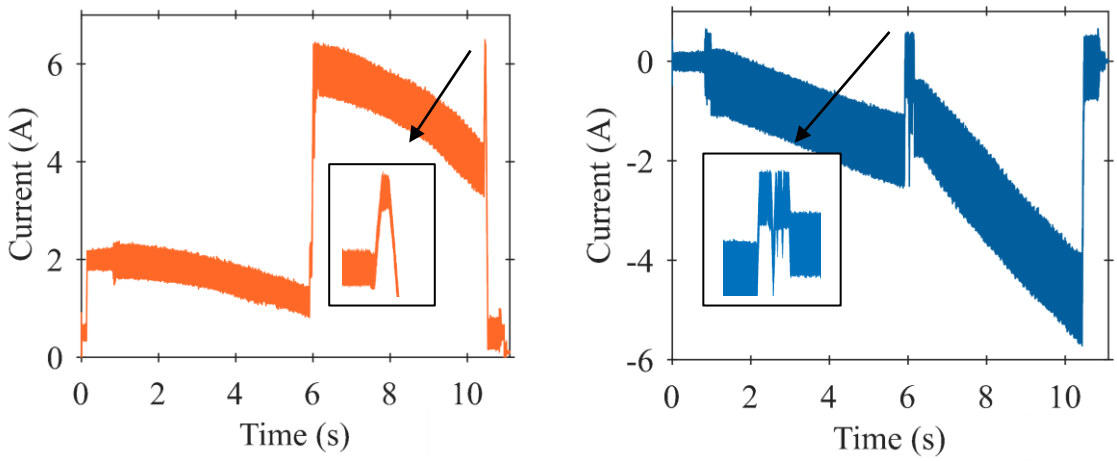

Fig. 4.6. Current tracking of adaptive PI control. (a) *q*–axis current. (b) *d*–axis current.

To mitigate the decoupling inaccuracy of PI controllers and enhance performance by incorporating parameter variation of saturation of IPMSM due to saturation, temperature, aging, and other factors; a DRL based current controller is proposed in the next chapter. The proposed DDPG DRL current controller interacts and learns from the plant environment, IPMSM and inverter, during exploration which makes it independent of the motor parameters during online control.

4.6 References

[1] K. A. K. Narita, Y. Sakashita, and T. Yamada, "Characteristics Comparison Between SPMSM and IPMSM Under High Flux Density Condition by Both Experimental and Analysis Results," in *Proc. ICEMS*, Wuhan, 2008, pp. 2848-2853.

[2] L. Fang, J. Jung, J. Hong, and J. Lee, "Study on High-Efficiency Performance in Interior Permanent-Magnet Synchronous Motor with Double-Layer PM Design," *IEEE Trans. Magnetics*, vol. 44, no. 11, pp. 4393-4396, Nov. 2008.

[3] B. D. S. G. Vidanalage, M. S. Toulabi and S. Filizadeh, "Multimodal Design Optimization of V-Shaped Magnet IPM Synchronous Machines," *IEEE Trans. Energy Conversion*, vol. 33, no. 3, pp. 1547-1556, Sept. 2018.

[4] C. He and T. Wu, "Analysis and Design of Surface Permanent Magnet Synchronous Motor and Generator," *CES Trans. Electrical Machines and Systems*, vol. 3, no. 1, pp. 94-100, March 2019.

[5] R. Krishnan, “Permanent-Magnet Synchronous and Brushless DC Motor Drive,” in *Electric Motor Drives*, 1st ed., Prentice-Hall, 2001, ch. 9, pp. 513-523.

[6] S. Vaez-Zadeh, *Control of permanent magnet synchronous motors*, Oxford University Press, 2018.

[7] H. Jie, G. Zheng, J. Zou, X. Xin, and L. Guo, "Adaptive Decoupling Control Using Radial Basis Function Neural Network for Permanent Magnet Synchronous Motor Considering Uncertain and Time-Varying Parameters," *IEEE Access*, vol. 8, pp. 112323-112332, May 2020.

[8] X. Yuan, S. Zhang, C. Zhang, A. Galassini, G. Buticchi, and M. Degano, "Improved Model Predictive Current Control for SPMSM Drives Using Current Update Mechanism," *IEEE Trans. Industrial Electronics*, vol. 68, no. 3, pp. 1938-1948, March 2021.

[9] K. Li and Y. Wang, "Maximum Torque Per Ampere (MTPA) Control for IPMSM Drives Based on a Variable-Equivalent-Parameter MTPA Control Law," *IEEE Trans. Power Electronics*, vol. 34, no. 7, pp. 7092-7102, July 2019.

[10] Field-Weakening Control (with MTPA) of PMSM, Mathworks, “https://www.mathworks.com/help/mcb/gs/field-weakening-control-mtpa-pmsm.html”

[11] TI Application Note, "Sensorless-FOC With Flux-Weakening and MTPA for IPMSM Motor Drives."

[12] N. Mohan, “Vector Control of Permanent-Magnet Synchronous Motor Drives,” in *Advanced Electric Drives-Analysis, Modeling and Control Using Simulink*, 1st ed., Wiley, 2001, ch. 10, pp. 143-155.

[13] G. Feng, C. Lai, W. Li, Z. Li, and N. C. Kar, "Efficient Permanent Magnet Temperature Modeling and Estimation for Dual Three-Phase PMSM Considering Inverter Nonlinearity," *IEEE Trans. Power Electronics*, vol. 35, no. 7, pp. 7328-7340, July 2020.

[14] G. Feng, C. Lai, J. Tjong, and N. C. Kar, "Investigation of Permanent Magnet Flux Linkage Variation in PMSMs Due to Temperature Rise and Magnetic Saturation," in *Proc. IECON*, Beijing, 2017, pp. 2034-2039.

[15] G. Feng, C. Lai, K. L. V. Iyer, and N. C. Kar, "Improved High-Frequency Voltage Injection Based Permanent Magnet Temperature Estimation for PMSM Condition Monitoring for EV Applications," *IEEE Trans. Vehicular Technology*, vol. 67, no. 1, pp. 216-225, Jan. 2018.

CHAPTER 5

DETERMINISTIC POLICY GRADIENT BASED NOVEL CURRENT CONTROLLER FOR IPMSM DRIVE

5.1 Introduction

Over the last decade, the hardware design of IPMSMs has been drastically improved for high power density, high torque–inertia ratio, high efficiency, and reliability [1]. However, the control scheme plays a vital role in the performance and efficiency of the IPMSM [2]. Also, the control techniques are sensitive to machine parameter uncertainties, load instabilities, etc. Conventionally, torque and speed control of IPMSM drive is achieved through field–oriented control (FOC) algorithm [3]. Conventional FOC algorithm implements nested proportional–integral (PI) based control loops for speed and stator current control of IPMSM, eliminating tracking errors under dynamic performance. The stator current control plays a key role in IPMSM torque control and its overall performance. The effective tuning of PI controller parameters depends on plant parameters which are derived from inverter and motor transfer functions. Under the entire operating range of the motor, equivalent circuit parameters such as *d*– and *q*–axis inductances change due to magnetic saturation, which in turn affect the FOC control performance during both steady-state and transient states and hence, the efficiency of the overall system performance [4]–[9]. Also, the performance and drawbacks of legacy adaptive PI are observed in chapter 4. With improved transient performance of the controller, better efficiency of IPMSM can be achieved [4].

Model predictive Control (MPC) uses complex mathematical equations to evaluate motor current at the next sampling state for optimal control action. Moreover, it makes use of the mathematical model of e–drive which increases the online computational burden. In real–time implementation, few parasitic effects of the overall control system, such as PMSM inductance and cross–saturation, are neglected to reduce the computation cost [5]–[7]. This reduces the overall performance and efficiency of the control system.

Direct torque control (DTC) utilizes a simplified approach for optimal torque control by selecting hysteresis bands and space vector modulation (SVM) switching tables.

However, this control also demands PI–based torque and flux controller which is further dependent on the system non–linear parameters. Although it demonstrates efficient dynamic response, it compromises the performance of IPMSM with increased torque ripple. In addition, DTC requires a high sampling rate, which in turn, increases the computational burden on digital signal processors (DSPs) [8].

Unlike conventional FOC, PI–PR control utilizes PR control with nested PI control loop to enhance current tracking capabilities. However, the PI–PR controller requires accurate tuning of resonant term, and its performance can be affected by the change in motor parameters under dynamic conditions [9].

Recently, there has been a growing interest in several other sophisticated and advanced control schemes such as fuzzy logic control [12]–[13], sliding mode control (SMC) [14]–[15] and so on [16]–[18]. All these schemes demonstrate the state–of–the–art control methods with significant improvements. The concept of fuzzy logic controller requires prior expertise on if–then rules and membership function which further makes the design of the controller complicated. SMC involves detailed and accurate mathematical equations which lead to increased computation burden in DSP. However, these control methods suffer from the drawback of varying load conditions. To address this issue, an additional load torque observer is required. Hence, there is also an utmost need to develop control with better robustness towards uncertain load for EV application.

The concept of deep neural network (DNN) based motor control is also well known. Neural network (NN) based IPMSM control has been proven to be efficient due to its effective control and reduced computation time. Recurrent NN (RNN) and radial bias function NN (RBFNN) are proposed in the literature to enhance the control performance of PMSM [10]–[11]. NNs use the concept of supervised learning and have proven to be a continued success in this domain. The use of supervised learning requires large and labeled training and test data sets under different dynamic conditions. Supervised learning maps the input vector to the anticipated target vector by adapting a generalized function approximation or cost function. However, supervised learning cannot generalize output when the input is unknown, such as varying load.

This chapter proposes a deterministic policy gradient based novel current controller (DPG–NCC) for dynamic stator current control of IPMSM for traction applications such

as EV. The legacy PI controller can be replaced by the proposed DRL agent based DDPG–NCC to mitigate non–linearity of system parameters, decoupling inaccuracy, and achieve optimal control solution. The block diagram with the control architecture of the proposed control is shown in Fig. 5.1.

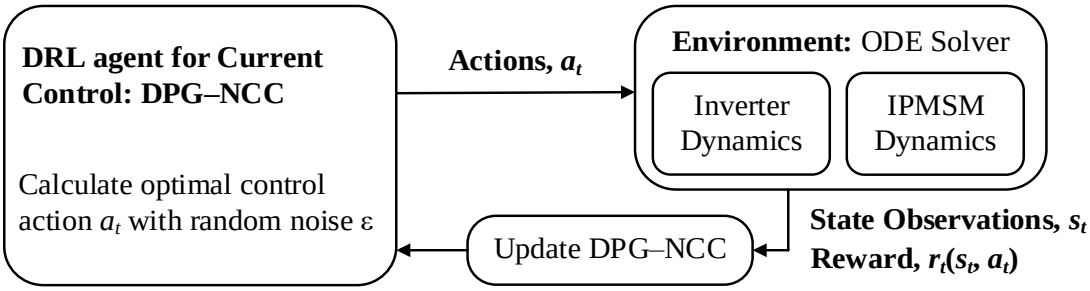

Fig. 5.1. Control architecture of DRL–based PMSM current control.

5.2 Deep Reinforcement Learning

Deep neural networks (DNNs) have been found to achieve remarkable performance in many different domains reducing the computational burden of complex mathematical algorithms through functionality approximations. However, the uncertain and dynamic environments limit the learning ability of supervised learning methodology. Data–driven based deep reinforcement learning (DRL) method can be used for online learning and implementing efficient control schemes under dynamic environments where the cost of exploration is expensive [19]–[20]. In RL, the agent explores and interacts with environment for an optimal action through reward estimation [21]. The block diagram of a RL learning scenario is shown in Fig. 5.2. Model–based RL involves the learning of the dynamic model and systematic approach for the execution of actions e.g., Markov Decision Process (MDP) [22]. Model–free learning can learn a policy by estimating the feedback directly interacting with the environment. Based on the network architecture model–free learning can be further categorized as value–based, policy–based, and actor–critic methods.

Value–based methods are based on *Q*–value estimation. The optimal actions are determined by the maximum cumulative reward corresponding to the input, e.g., deep *Q*–

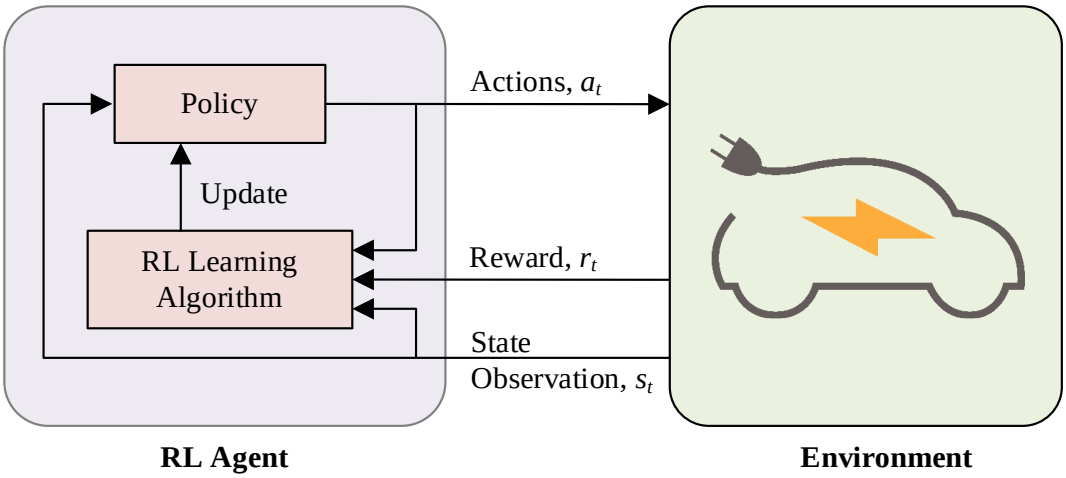

Fig. 5.2. Block diagram of RL learning scenario.

Learning (DQL) [23]. In IPMSM current control, the DQL estimates the optimality of reference voltages, however, it does not optimize the controller to enhance the control signals. On the other hand, policy–based methods compute the possibilities of optimal actions, e.g., REINFORCE algorithm [24], enabling the network to compute only the reference voltages without evaluating its global optimality. The main drawback is that it may converge at a local optimum. Hence, the network may not achieve a globally optimum solution in the continuous state–action spaces. The proposed actor–critic method incorporates both the value– and policy–based methodologies enabling both offline and online learning.

5.3 DRL Based DPG–NCC

The proposed optimal current controller uses the off–policy, actor–critic method to adapt to the continuous action spaces. The RL agent interacts with the plant environment, inverter and IPMSM, to create the optimal deterministic policy function, μ. The RL agent incorporates deep neural networks, actor and critic, to generate the optimal control actions, v_d and v_q. The actor network is trained to imitate the optimal control action of the controller at a given state by maximizing the reward through gradient ascent. A *Q*–learning–based critic network is used to evaluate the accuracy of the state–action pairs by estimating the reward value from the environment feedback. Further, the critic network tunes the actor network from the evaluation of the state–action pairs (*Q*–value) and cumulative reward.

The critic *Q*–values estimation for a deterministic policy can be formulated from the fundamental Bellman equation in (5.1)

$$Q^{\mu}\left(s_t, a_t\right) = \underset{P(s_{t+1}, r|s_t, a_t)}{\mathrm{E}}\left[r\left(s_t, a_t\right) + \gamma \max_{a_{t+1}} Q^{\mu}(s_{t+1}, a_{t+1}) \right] \tag{5.1}$$

where t is the discrete-time step, a is the optimal reference voltages v_d and v_q at state observation $s \in \{i_d, i_q, e_d, e_q, \int e_d, \int e_q\}$, $\gamma \in (0,1]$ is the discount factor, E is the expectation function, and r is the reward function. The reward function r for the proposed optimal current control is defined in (5.2) where u_{t-1} is the action output from the previous time step.

$$r = -(5e_d^2 + 5e_q^2 + 0.001u_{t-1}^2) \tag{5.2}$$

In the DDPG–NCC of IPMSM, the reward r starts from a negative value and converges towards zero to achieve optimal reference stator voltages, v_d and v_q. However, the cumulative reward does not achieve absolute zero due to the penalized negative rewards from transitions between observation states.

5.4 Training and Tuning of DRL Based DPG–NCC

This section proposes deterministic policy gradient-based learning algorithms to train the RL agent to achieve optimal actions based on the actor–critic architecture. The deep deterministic policy gradient (DDPG) based learning is used for single *Q*–value estimation, twin delayed deep deterministic policy gradient (TD3) algorithm is used for dual *Q*–learning estimation and multi–critic multi–*Q*–learning (MCMQL) is used for enhanced multi–*Q*–value estimation for the actor–critic network. The training of the RL agent for optimal control under the three cases is explained in the following sections.

5.4.1 Deep Deterministic Policy Gradient Scheme

The DDPG algorithm is an online, model–free learning for continuous time and action spaces. This algorithm aids the RL agent to interact with the plant environment, inverter and IPMSM, and learn the *Q* function and optimal policy. The training of the RL

agent is carried through sample transitions and estimating the *Q*–value in the critic network. The *Q*–value, y_t is estimated from (5.3),

$$y_t = r(s_t, a_t) + \gamma Q'(s_{t+1}, \mu(s_{t+1} \mid \theta^{\mu}) \mid \theta^{Q'}) \tag{5.3}$$

where θ^{μ} is the weight of the deterministic policy function (actor), θ^{Q} is the weight of the *Q* network (critic) and $\theta^{Q'}$ is the target critic network weight. Equation (5.3) enables to determine the global optimality of the reference voltages, v_d and v_q. The critic network weights are updated from the temporal difference (TD) error to calculate the mean–squared Bellman error (MSBE) by minimizing the loss function $L(\theta^{Q})$ between the original and updated *Q*–value as in (5.4) where *M* is the mini–batch of experiences.

$$L\left(\theta^{Q}\right) = \frac{1}{M}\sum_{t}\left(y_t - Q\left(s_t, a_t \mid \theta^{Q}\right)\right)^2 \tag{5.4}$$

The objective of the actor network is to maximize the expected reward through gradient ascent calculation as in (5.5). The weights of the actor network are updated from the derivative of the objective function, $J(\theta)$ through chain rule as represented in (5.6). Using (5.6) the actor network is optimized to generate the optimal IPMSM control voltages v_d and v_q.

$$J\left(\theta\right) = \mathrm{E}\left[Q\left(s,a\right)|_{s=s_t, a_t=\mu(s_t)}\right] \tag{5.5}$$

$$\nabla_{\theta^{\mu}} J\left(\theta\right) \approx \frac{1}{M}\sum_{i}\left[\nabla_a Q\left(s,a \mid \theta^{Q}\right)|_{s=s_t, a=\mu(s_t)} \nabla_{\theta^{\mu}} \mu\left(s \mid \theta^{\mu}\right)|_{s=s_t}\right] \tag{5.6}$$

To facilitate exploration of the RL agent, a decaying noise ε is added to the actor policy based on the Ornstein–Uhlenbeck process [29] as in (5.7).

$$a_t = \mu\left(s_t \mid \theta^{\mu}\right) + \varepsilon \tag{5.7}$$

Finally, the target actor ($\mu'(s|\theta^{\mu'})$) and critic network ($Q'(s,a|\theta^{Q'})$) is updated at every time step using (5.8), where τ is the smoothing factor and less than 1.

$$\begin{cases} \theta^{Q'} \leftarrow \tau\theta^{Q} + (1-\tau)\theta^{Q'} \\ \theta^{\mu'} \leftarrow \tau\theta^{\mu} + (1-\tau)\theta^{\mu'} \end{cases} \tag{5.8}$$

The process of obtaining the optimal actions, v_d and v_q, by maximizing the discounted cumulative reward is achieved through regression. Using the DDPG learning algorithm, the critic network estimates the *Q*–value by evaluating the Bellman equation in (5.1) and retune the actor network to achieve optimality. Fig. 5.3 demonstrates the overall workflow of the DDPG learning method.

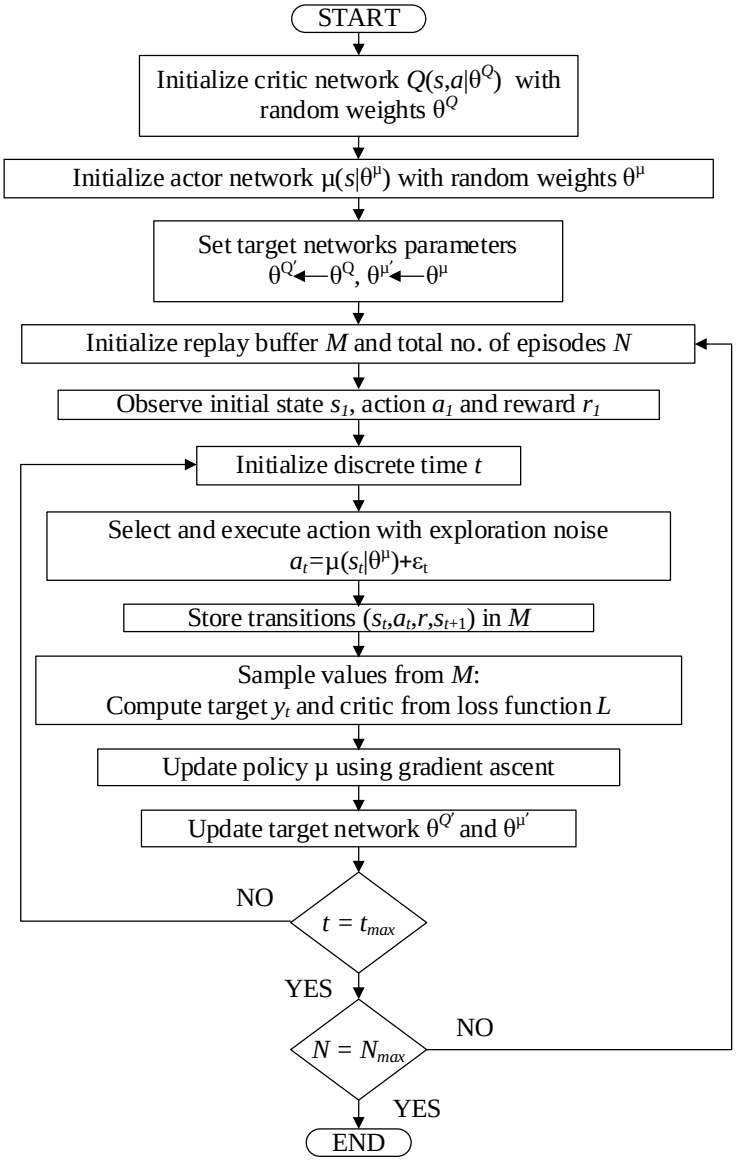

Fig. 5.3. Training workflow of DDPG algorithm for DPG–NCC.

The hyperparameters of the proposed actor–critic networks during training are shown in Table 5.1. Fig. 5.4 represents the schematic of the current control with the DDPG algorithm.

TABLE 5.1

DDPG TRAINING HYPERPARAMETERS

Hyperparameters	**Values**
No. of layers	2
Neurons in actor network	150/100
Neurons in critic network	500/400
Learning rate of actor	1×10^{-4}
Learning rate of critic	1×10^{-3}
Activation function of actor	*tanh*
Activation function of critic	*ReLU*
Discount factor, γ	0.9
Sample time. T_s	1×10^{-4} s
Mini–batch size, *M*	512
Decaying Noise, ε	1×10^{-3} V
Optimizer	Adam

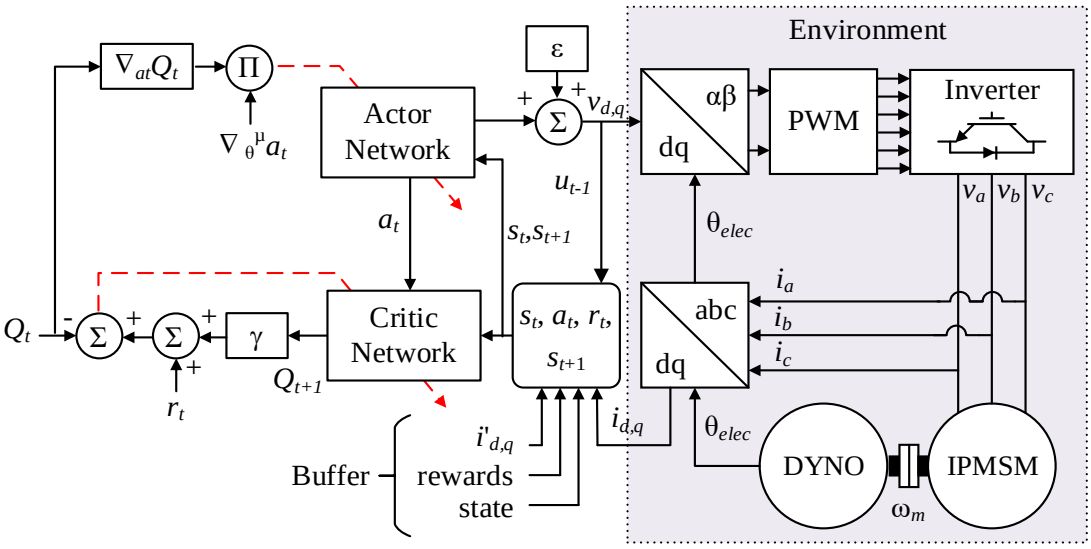

Fig. 5.4. Schematic of optimal DPG–NCC with DDPG scheme.

The actor and critic network apply *tanh* and *ReLU* activation functions respectively in the hidden layers. During training, it is observed that a two–layered actor network shows more stability than a shallow network. The schematic of the DDPG actor–critic network layout is shown in Fig. 5.5.

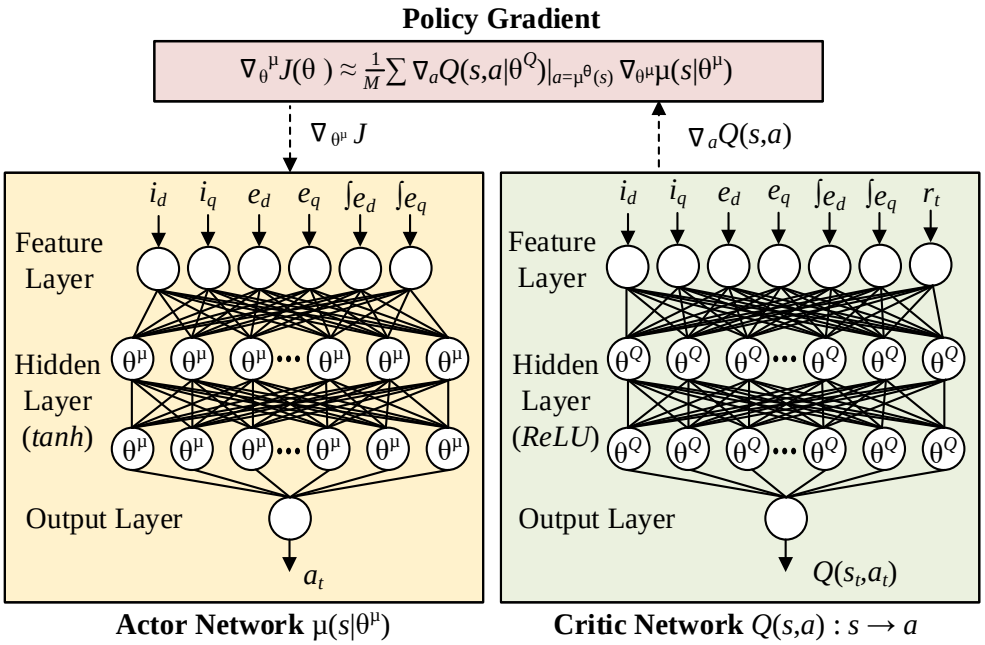

Fig. 5.5. Schematic of DDPG actor–critic network.

From (5.2), the RL agent converges from a negative value to the estimated Q–value of critic network (0 ← Q–value), for a profitable reward through optimal v_d and v_q. The RL agent maximizes the reward value with respect to the *Q*–value estimation. However, due to dynamic variation in speed reference i_d and i_q the reward never achieves perfect zero value or the estimated *Q*–value since the agent is also penalized for constraints violations.

During the training and tuning of the overall system with DPG–NCC and IPMSM, the reward from the previous episode is used as feedback in the next episode by the critic network to optimize the action of actor network through gradient ascent. This iterative process over *N* episodes enables a strong memorization ability of the actor network with accurate current tracking ability. Figure 5.6 demonstrates the training and tuning of the overall system with DDPG–based DRL controller and IPMSM over *N* training episodes. The total cumulative discounted reward over an action for every episode during the DRL training is represented in Fig. 5.7.

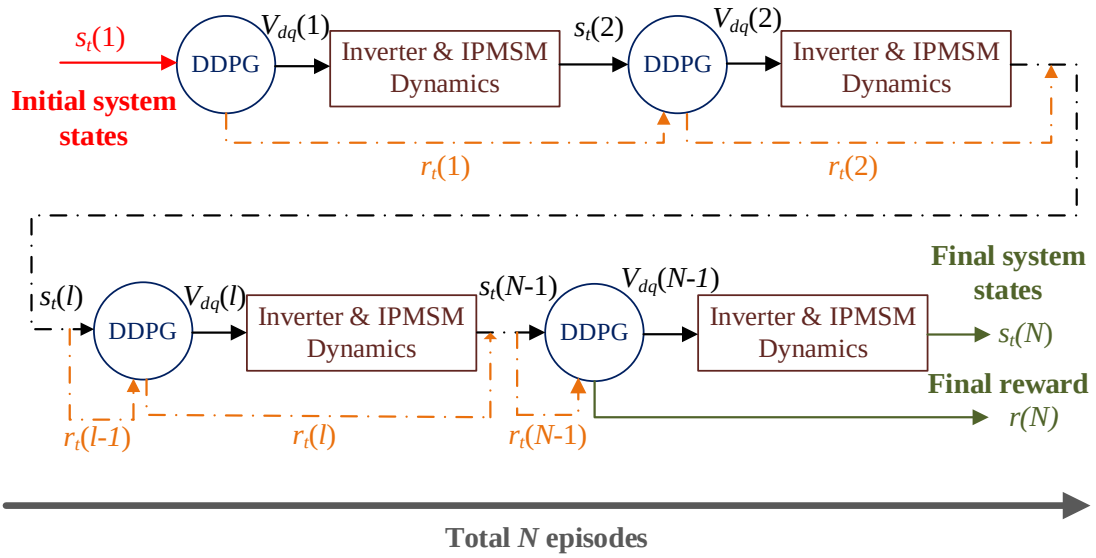

Fig. 5.6. Training and tuning of the DDPG based DRL controller with IPMSM, $s_t \in \{i_d, i_q, e_d, e_q, \int e_d, \int e_q\}$.

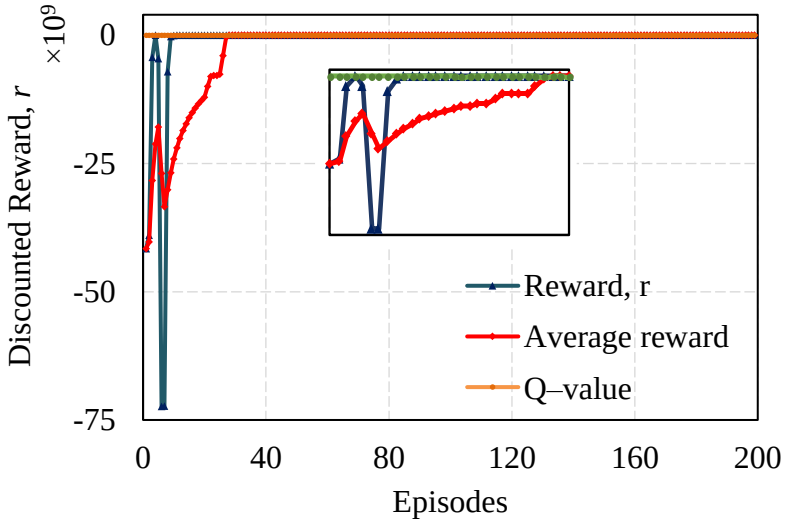

Fig. 5.7. Discounted cumulative reward of RL agent using DDPG algorithm.

An average of the last 40 episodic rewards is considered while training the agent for a generalized performance of the network.

5.4.2 Twin Delayed Deep Deterministic Policy Gradient Scheme

Twin delayed deep deterministic policy gradient (TD3) is an advanced deterministic policy gradient-based learning algorithm with clipped dual *Q*–learning. The

implementation of a secondary critic network for dual *Q*–learning mitigates the overestimation of *Q*–values in the early stage of learning. Also, the target policy update is delayed making the critic network more stable.

Using the double *Q*–learning, the learning targets, y_1 and y_2 are updated from temporal difference learning (TD) and are in (5.9), where π is the deterministic actor and $Q_{1,2}$ are the critic network with parameters φ and θ respectively.

$$\begin{cases} y_1 = r + \gamma Q_{\theta 1}\left(s_{t+1}, \pi_{\phi}\left(s_{t+1}\right)\right) \\ y_2 = r + \gamma Q_{\theta 2}\left(s_{t+1}, \pi_{\phi}\left(s_{t+1}\right)\right) \end{cases} \tag{5.9}$$

However, to prevent overestimation of *Q*–value the minimum *Q*–learning estimates are chosen. The updated target from (5.9) is modified in (5.10). Hence (5.10) is used to determine the global optimality of the IPMSM reference voltage v_d and v_q. To facilitate exploration a random noise ε is added to the target, shown in (5.11). The addition of random noise enables enhanced *Q*–value exploration through policy.

$$y = r + \gamma \min_{i=1,2} Q_{\theta i}\left(s_{t+1}, \pi_{\phi}\left(s_{t+1}\right)\right) \tag{5.10}$$

$$y = r + \gamma \min_{i=1,2} Q_{\theta i}\left(s_{t+1}, \pi_{\phi}\left(s_{t+1}\right) + \varepsilon\right) \tag{5.11}$$

The critic parameters θ is updated as per (5.12), where i=1, 2 and M is a mini–batch of transitions (s, a, r, s_{t+1}) in batch data.

$$\theta_i \leftarrow \arg\min_{\theta_i} \frac{1}{M} \sum \left(y - Q_{\theta_i}\left(s_t, a_t\right)\right)^2 \tag{5.12}$$

To ensure the stability of the networks the actor network is updated at a lower frequency than critic network. The update for actor and critic parameters is delayed using Polyak averaging as shown in (5.13), where i=1, 2 and τ is the smoothing factor.

$$\begin{cases} \theta_{target,i} \leftarrow \tau\theta_{target,i} + \left(1-\tau\right)\theta \\ \phi_{target} \leftarrow \tau\phi_{target} + \left(1-\tau\right)\phi \end{cases} \tag{5.13}$$

The schematic of the TD3 actor–critic network layout is shown in Fig. 5.8.

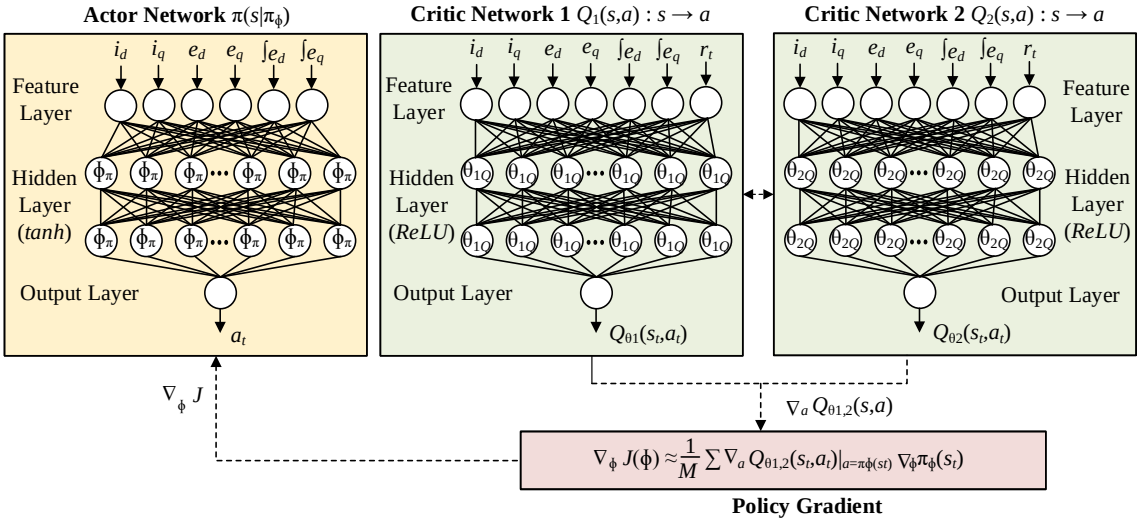

Fig. 5.8. Schematic of TD3 actor–critic network.

The update equation for actor policy π_φ is expressed as the gradient of the cumulative expected return J as expressed in (5.14). The workflow of the advanced TD3 algorithm is shown in Fig. 5.9.

$$\nabla_\phi J(\phi) = \frac{1}{M} \sum \nabla_a Q_{\theta_i}(s_t, a_t)|_{a=\pi_\phi(s_t)} \nabla_\phi \pi_\phi(s_t) \tag{5.14}$$

The actor and critic NN are trained to obtain an optimal controller performance. The critic network is trained which evaluates the Bellman equation in (5.1). The actor network adapts the reference voltages v_d and v_q of IPMSM concerning the critic optimality estimation of v_d and v_q with the goal of a profitable cumulative reward. The ideal weights of actor and critic network are obtained through regression until the RL agent achieves the optimal policy by maximizing reward. The tuning of the TD3 controller is similar to the DDPG based controller as shown in Fig. 5.6. Table 5.2 provides the TD3 training hyperparameters of the actor– critic network.

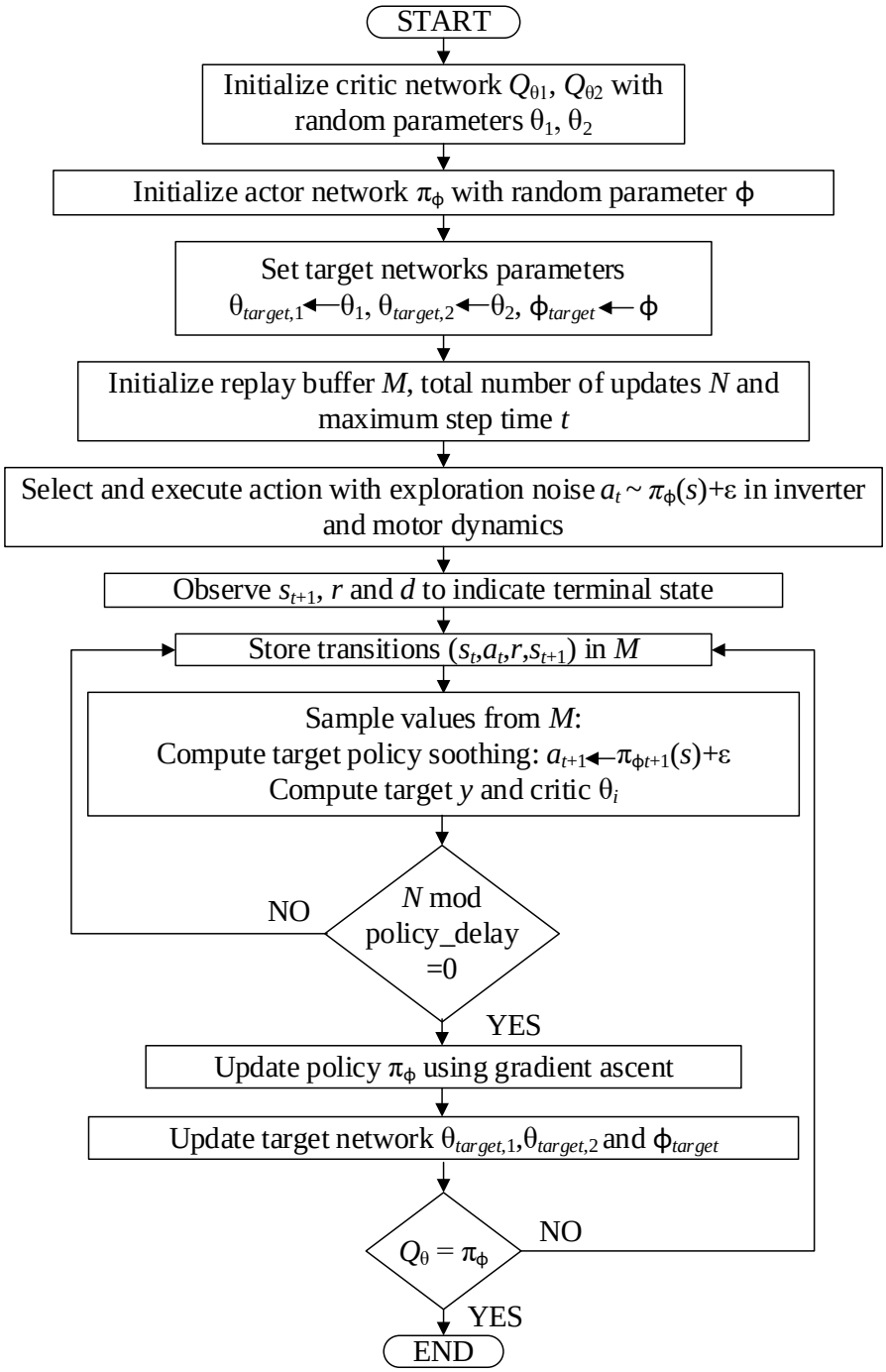

Fig. 5.9. Training workflow of TD3 algorithm for DPG–NCC.

The two-layered network shows the consistent output as compared to a single-layered network. Also increasing of layer caused in overfitting of data resulting in poor performance. The cumulative episode reward curve during the training of RL agent is shown in Fig. 5.10. The *Q*–value curve denotes the value estimates from the critic network.

TABLE 5.2

TD3 TRAINING HYPERPARAMETERS

Hyperparameters	Values
No. of layers	2
Neurons in actor network	250/200
Neurons in critic network	500/400
Learning rate of actor	1×10^{-3}
Learning rate of critic1 and critic 2	1×10^{-3}
Activation function of actor	*tanh*
Activation function of critic1 and critic 2	*ReLU*
Discount factor, γ	0.995
Sample time. T_s	1×10^{-4} s
Mini–batch size, *M*	512
Decaying Noise, ε	1×10^{-3} V
Optimizer	Adam

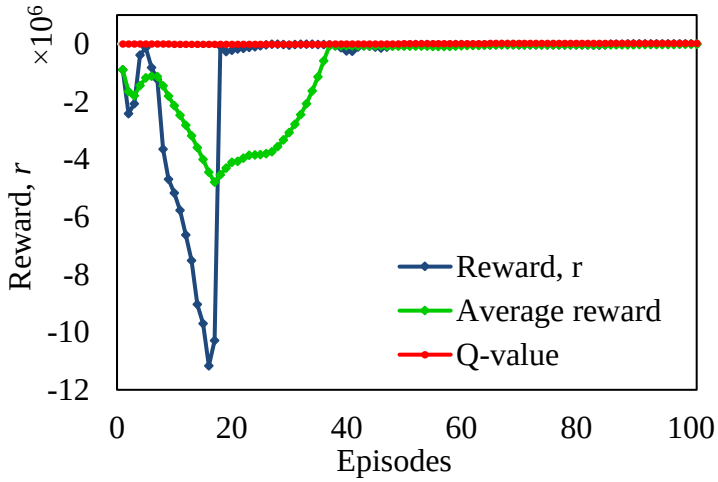

Fig. 5.10. Discounted cumulative reward of RL agent using TD3 algorithm.

The reward curve implicates the total reward earned by the RL agent taking an action. The average reward denotes the average of the last 20 cumulative episode rewards for effective generalization of actor–critic network. The schematic of the current control with the TD3 algorithm is illustrated in Fig. 5.11.

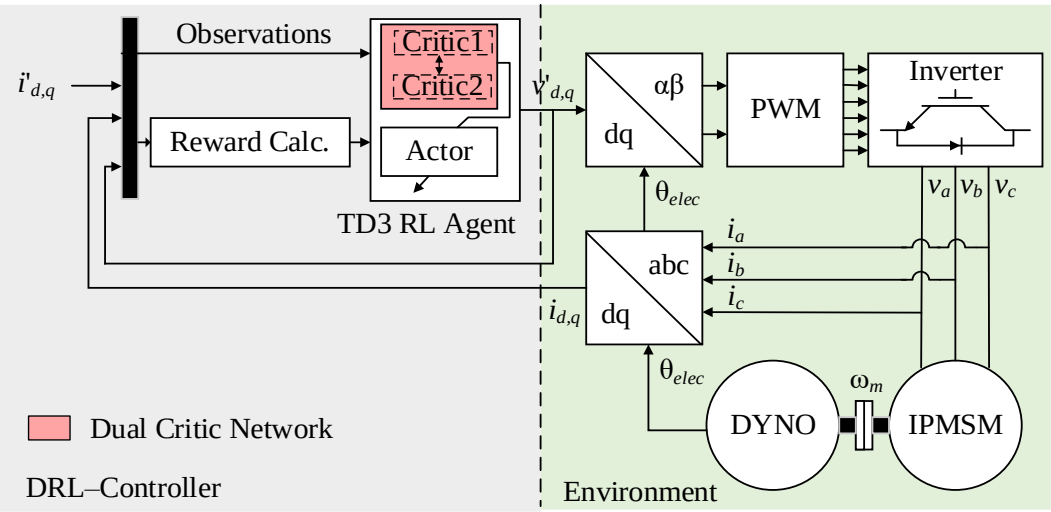

Fig. 5.11. Schematic of optimal DPG–NCC with TD3 scheme.

5.4.3 Multi–Critic Multi–Q–Learning Scheme

The novel multi–critic multi–*Q*–learning (MCMQL) is a deterministic off–policy, online, model–free, actor–critic method to adapt to the continuous action spaces. Like DDPG and TD3, the RL agent interacts with the plant environment, inverter and IPMSM, to create the optimal deterministic policy function, π. The training of the RL agent is carried through sample transitions then estimating the *Q*–value using the multi-critic network. Using the multi–*Q*–learning, the learning targets, y_1, y_2, …, y_n are updated from temporal difference learning (TD) and are given in (5.15), where π is the deterministic actor and Q_j is the multi–critic network with parameters φ and θ_j respectively, where j=1,2, 3, …, n and n is any positive integer. The *Q*–value, y_j is estimated from equation (5.15) and is shown below:

$$y_j = r + \gamma Q_{\theta j}\left(s_{t+1}, \pi_{\phi}\left(s_{t+1}\right)\right) \tag{5.15}$$

To prevent overestimation of *Q*–value, the minimum *Q*–learning estimates are chosen from (5.15). The critic parameters θ is updated as per (5.16), where j=1,2, …, n critic networks and M is a mini–batch of transitions (s, a, r, s_{t+1}) in batch data. The target multi–critic network is updated using (5.17).

$$\theta_j \leftarrow \arg\min_{\theta j} \frac{1}{M} \sum \left(y - Q_{\theta_j}\left(s_t, a_t\right) \right)^2 \tag{5.16}$$

$$\theta_{target,j} \leftarrow \tau\theta_{target,j} + (1-\tau)\theta \tag{5.17}$$

The actor and policy gradient update remains the same as the TD3 learning scheme.

The schematic of the current control block diagram and MCMQL–based optimization algorithm is shown in Figs. 5.12 and 5.13, respectively. The MCMQL optimization will enable the following advantages:

1. Multi–critic with multi–*Q*–learning mitigates the overestimation of *Q* value in the early stage of learning;
2. Multi–critic with multi–*Q*–learning can maximize the reward through avoiding local maximums further enabling fast convergence towards optimality;
3. Multi–critic with multi–*Q*–learning can adapt to the learning performance and enabling efficiency trade–off of reinforcement learning.

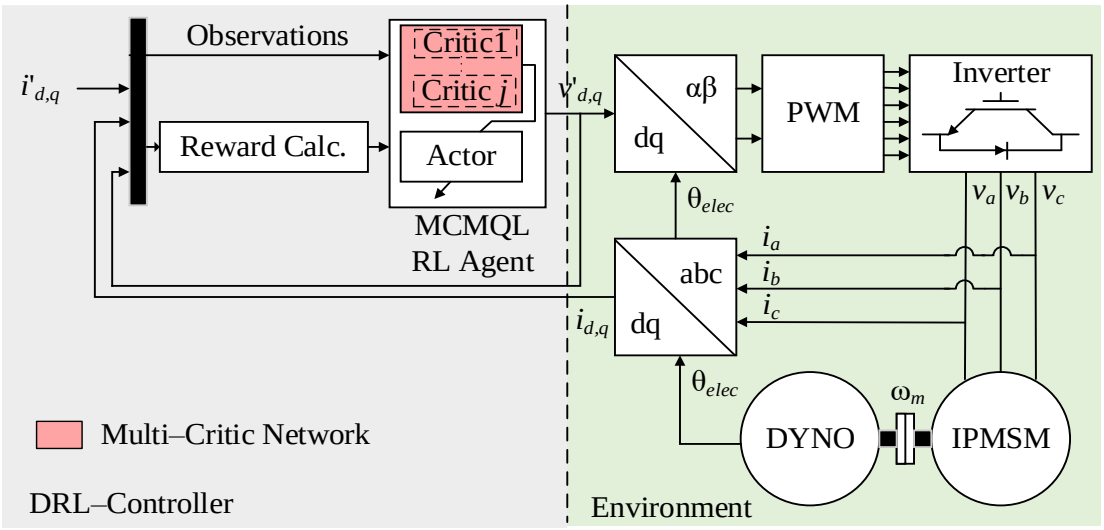

Fig. 5.12. Schematic of optimal DPG–NCC with MCMQL scheme.

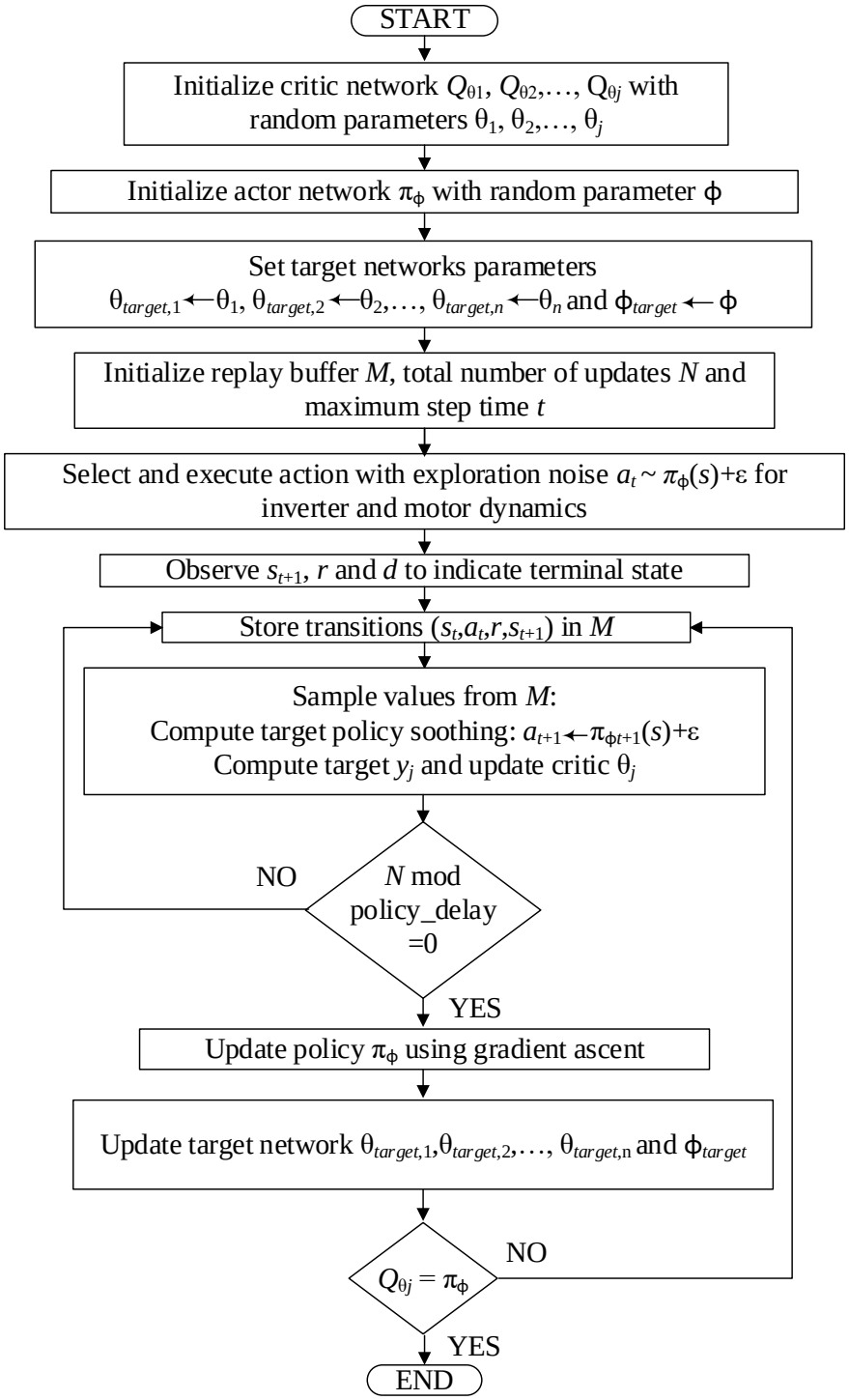

Fig. 5.13. Training workflow of MCMQL algorithm for DPG–NCC.

The implementation and validation results of the proposed DPG–NCC under different current loading conditions are illustrated in the next chapter.

5.5 References

[1] J. A. Güemes, A. M. Iraolagoitia, J. I. Del Hoyo, and P. Fernández, “Torque Analysis in Permanent-Magnet Synchronous Motors: A Comparative Study,” *IEEE Trans. Energy Conversion*, vol. 26, no. 1, pp. 55-63, March 2011.

[2] M. S. Rafaq, and J. Jung, “A Comprehensive Review of State-of-the-Art Parameter Estimation Techniques for Permanent Magnet Synchronous Motors in Wide Speed Range,” *IEEE Trans. Industrial Informatics*, vol. 16, no. 7, pp. 4747-4758, July 2020.

[3] L. Amezquita-Brooks, J. Liceaga-Castro, and E. Liceaga-Castro, "Speed and Position Controllers Using Indirect Field-Oriented Control: A Classical Control Approach," *IEEE Trans. Industrial Electronics*, vol. 61, no. 4, pp. 1928-1943, April 2014.

[4] A. Balamurali, G. Feng, C. Lai, J. Tjong, and N. C. Kar, "Maximum Efficiency Control of PMSM Drives Considering System Losses Using Gradient Descent Algorithm Based on DC Power Measurement," *IEEE Trans. Energy Conversion*, vol. 33, no. 4, pp. 2240-2249, Dec. 2018.

[5] Y. Han, C. Gong, L. Yan, H. Wen, Y. Wang, and K. Shen, "Multiobjective Finite Control Set Model Predictive Control Using Novel Delay Compensation Technique for PMSM," *IEEE Trans. Power Electronics*, vol. 35, no. 10, pp. 11193-11204, Oct. 2020.

[6] T. Türker, U. Buyukkeles and A. F. Bakan, "A Robust Predictive Current Controller for PMSM Drives," *IEEE Trans. Industrial Electronics*, vol. 63, no. 6, pp. 3906-3914, June 2016.

[7] Y. Zhou and G. Chen, "Predictive DTC Strategy With Fault-Tolerant Function for Six-Phase and Three-Phase PMSM Series-Connected Drive System," *IEEE Trans. Industrial Electronics*, vol. 65, no. 11, pp. 9101-9112, Nov. 2018.

[8] J. Kim, S. Ryu, M. S. Rafaq, H. H. Choi, and J. Jung, “Improved Torque Ripple Minimization Technique with Enhanced Efficiency for Surface- Mounted PMSM Drives,” *IEEE Access*, vol. 8, pp. 115017-115027, 2020.

[9] C. Xia, B. Ji, and Y. Yan, “Smooth Speed Control for Low-Speed High-Torque Permanent-Magnet Synchronous Motor Using Proportional–Integral–Resonant Controller,” *IEEE Trans. Industrial Electronics*, vol. 62, no. 4, pp. 2123-2134, April 2015.

[10] H. Jie, G. Zheng, J. Zou, X. Xin, and L. Guo, “Adaptive Decoupling Control Using Radial Basis Function Neural Network for Permanent Magnet Synchronous Motor Considering Uncertain and Time-Varying Parameters,” *IEEE Access*, vol. 8, pp. 112323-112332, 2020.

[11] S. Li, H. Won, X. Fu, M. Fairbank, D. C. Wunsch, and E. Alonso, "Neural-Network Vector Controller for Permanent-Magnet Synchronous Motor Drives: Simulated and Hardware-Validated Results," *IEEE Trans. Cybernetics*, vol. 50, no. 7, pp. 3218-3230, July 2020.

[12] G. Feng, C. Lai, and N. C. Kar, "A Closed-Loop Fuzzy-Logic-Based Current Controller for PMSM Torque Ripple Minimization Using the Magnitude of Speed Harmonic as The Feedback Control Signal," *IEEE Trans. Industrial Electronics*, vol. 64, no. 4, pp. 2642-2653, April 2017.

[13] Z. Wang, A. Yu, X. Li, G. Zhang and C. Xia, "A Novel Current Predictive Control Based on Fuzzy Algorithm for PMSM," *IEEE Journal of Emerging and Selected Topics Power Electronics*, vol. 7, no. 2, pp. 990-1001, June 2019.

[14] A. K. Junejo, W. Xu, C. Mu, M. M. Ismail, and Y. Liu, "Adaptive Speed Control of PMSM Drive System Based a New Sliding-Mode Reaching Law," *IEEE Trans. Power Electronics*, vol 35, no. 11, pp 12110-12121, Nov. 2020.

[15] Y. Xu, M. Wang, W. Zhang, and J. Zou, "Sliding Mode Observer for Sensorless Control of Surface Permanent Magnet Synchronous Motor Equipped With LC filter," *IET Power Electronics*, vol. 12, no. 4, pp. 686-692, 10 4 2019.

[16] A. Balamurali, G. Feng, A. Kundu, H. Dhulipati, and N. C. Kar, “Noninvasive and Improved Torque and Efficiency Calculation Toward Current Advance Angle Determination for Maximum Efficiency Control of PMSM,” *IEEE Trans. Transportation Electrification*, vol. 6, no. 1, pp. 28-40, March 2020.

[17] G. Feng, C. Lai, and N. C. Kar, "A Novel Current Injection-Based Online Parameter Estimation Method for PMSMs Considering Magnetic Saturation,” *IEEE Trans. Magnetics*, vol. 52, no. 7, pp. 1-4, July 2016.

[18] Z. Li, P. Song, B. Sato, W. Li, H. Dhulipati and N. C. Kar, "Novel Current Injection Based Multi-Parameter Estimation Technique for Dual Three-Phase PMSMs," in *Proc.* 2020 *ICEMS*, Hamamatsu, Japan, 2020, pp. 888-893.

[19] K. M. Jagodnik, P. S. Thomas, A. J. van den Bogert, M. S. Branicky, and R. F. Kirsch, “Training an Actor-Critic Reinforcement Learning Controller for Arm Movement Using Human-Generated Rewards,” *IEEE Trans. Neural Systems and Rehabilitation Engineering*, vol. 25, no. 10, pp. 1892-1905, Oct. 2017.

[20] D. Görges, "Relations Between Model Predictive Control and Reinforcement Learning," *IFAC-Papers On-Line*, vol. 50, no. 1, pp. 4920-4928, 2017.

[21] Q. Zheng, C. Jin, Z. Hu, and H. Zhang, “A Study of Aero-Engine Control Method Based on Deep Reinforcement Learning,” *IEEE Access*, vol. 7, pp. 55285-55289, 2019.

[22] J. Tarbouriech, S. Shekhar, M. Pirotta, M. Ghavamzadeh, and A. Lazaric, "Active Model Estimation in Markov Decision Processes," arXiv preprint arXiv:2003.03297, 2020.

[23] J. Fan, Z. Wang, Y. Xie, and Z. Yang., "A Theoretical Analysis of Deep Q-Learning," in *Proc. In Learning for Dynamics and Control*, PMLR, 2020, vol. 120, pp. 486-489.

[24] R. J. Williams, "Simple Statistical Gradient-Following Algorithms for Connectionist Reinforcement Learning," *Machine Learning*, vol 8, pp. 229-256, 1992.

[25] T. P. Lillicrap *et al.*, "Continuous control with deep reinforcement learning, " arXiv preprint arXiv:1509.02971, 2015.

CHAPTER 6

IMPLEMENTATION AND VALIDATION OF DPG–NCC IN IPMSM DRIVE

6.1 Introduction

This chapter extends the work from the chapter 5 to validate the proposed DPG–NCC. A software–in–the–loop (SIL) testing of the DPG–NCC based current control of PMSM drive in a real–time environment (RTE) is illustrated in this chapter. For accurate analysis and validation of the proposed DDPG DRL control performance, the corresponding C code is developed for SIL testing. A state–of–the–art adaptive PI controller based current control is also developed and its performance is compared against the proposed DRL–based current control for IPMSM.

6.2 Performance Evaluation of DPG–NCC vs Adaptive PI

To demonstrate the effectiveness and practical feasibility of the proposed DRL current control scheme, software–in–the–loop (SIL) testing is performed using OPAL–RT real-time simulator. The SIL test setup and overall block diagram of the proposed DRL current control in the RTE is shown in Figs. 6.1. OPAL-RT is used to compile and run

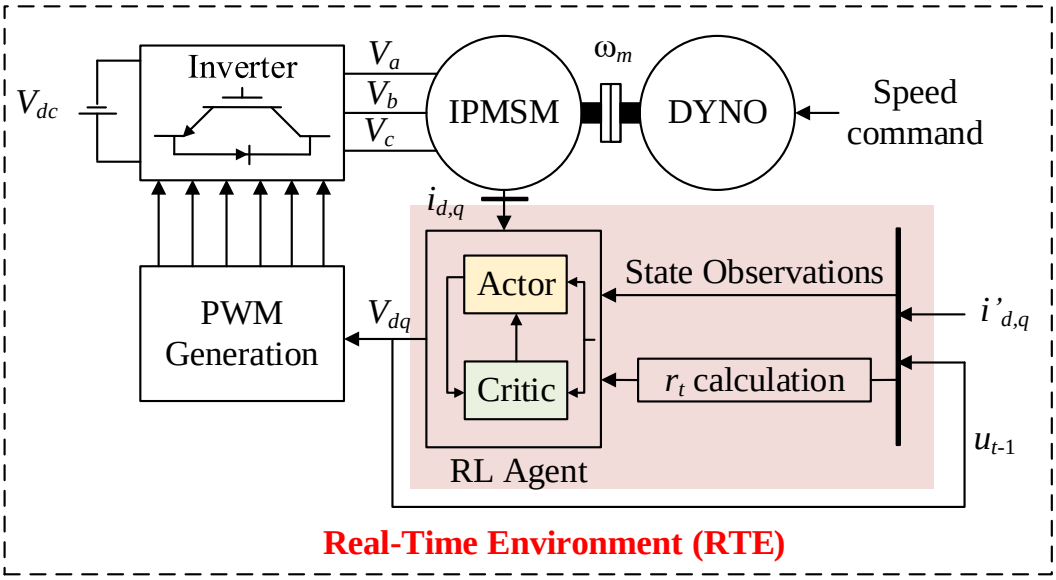

Fig. 6.1. Test setup for SIL validation of DRL–based current control of IPMSM.

the developed current control models in RTE. The parameters from Table 4.1 are used for the IPMSM model development. In Fig. 6.1 the tracking ability of the current loop controller is evaluated by rotating the device under test (DUT) at a constant speed with a speed–controlled dynamometer, while the reference *d*– and *q*–axis currents are varied to produce torque.

6.2.1 Test 1: Current Tracking

In Test 1, the proposed DDPG DRL–based controller is validated with the same setup as in Fig. 6.1 to evaluate its current tracking capability. The reference *d*– and *q*–axis currents are changed to study the transient and dynamic tracking capability of the proposed DRL–based advanced current controller. The SIL testing results with the performance comparison are shown in Fig. 6.2. The reference *q*–axis current is changed from 15 A to 5 A at 0.3 s and again to 10 A at 0.6 s. Similarly, at 0.45 s, the *d*–axis reference current is changed from –15 A to –5 A. From Fig. 6.2, it is observed that the proposed DPG–NCC and PI-based current controllers tracks the reference *q*– and *d*–axis currents satisfactorily in steady-state. The optimal reference stator voltages v_d and v_q of the DPG–NCC corresponding to Fig. 6.2 is presented in Fig. 6.3.

The cumulative reward earned by the RL agent during the current tracking evaluation is shown in Fig. 6.4. Due to the constraint violations during the change in reference currents, the cumulative reward decreases at 0.3, 0.45, and 0.6 s, respectively. However, the cumulative rewards remain the same during the steady state operation.

The DPG–NCC shows fast and promising dynamic characteristics mitigating decoupling inaccuracy. Also, a reliable response with reduced transient peaks by 5 A is observed in DPG–NCC compared to adaptive PI.

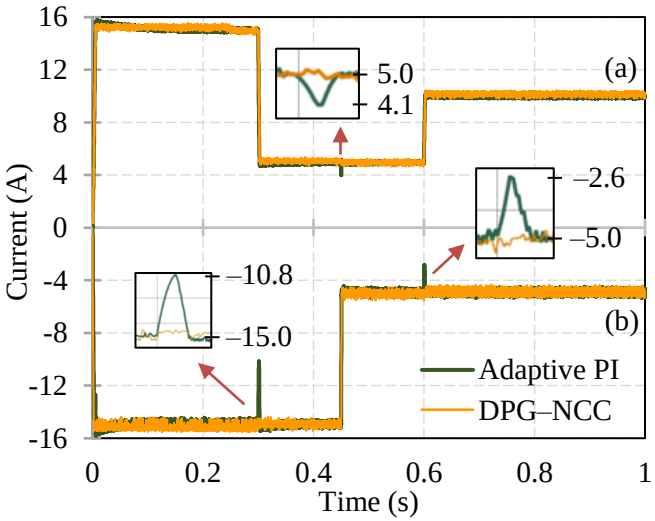

Fig. 6.2. Current tracking, DPG–NCC versus adaptive PI control. (a) *q*–axis current. (b) *d*–axis current.

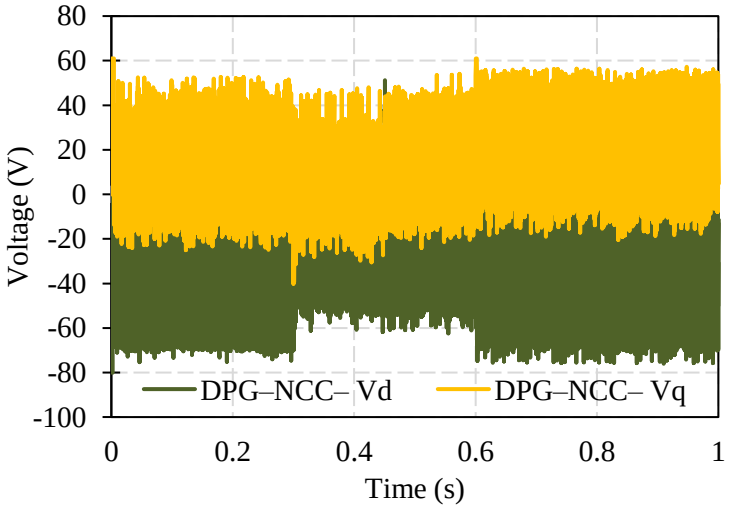

Fig. 6.3. Voltage tracking using DPG–NCC controller.

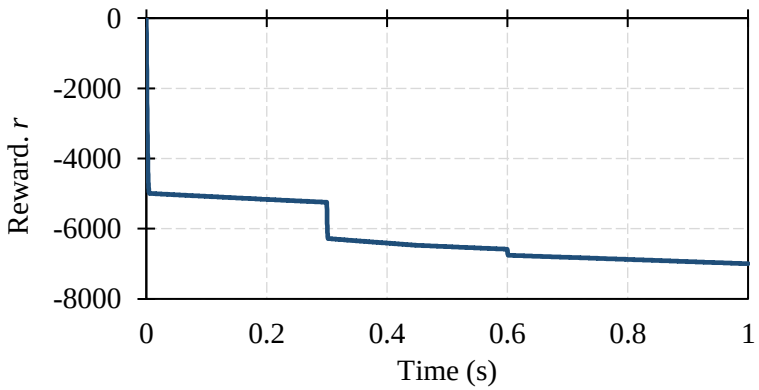

Fig. 6.4. Cumulative reward of DPG–NCC RL agent during current tracking evaluation.

6.2.2 Test 2: Impact of Rotor Flux Linkage Under Dynamic Performance

Performance of the IPMSM changes with magnet temperature change. The relationship between magnet temperature T and PM flux linkage λ_m is expressed in (6.1), where T_{ref} is the reference temperature of the magnet and $\alpha_{\beta r}$ is the temperature coefficient of the magnet. Hence, under real–time operation the rotor magnetic flux linkage changes with an increase in temperature which further affects the current, performance, and reliability of the IPMSM.

$$\lambda_m\left(T\right)=\lambda_{m(Tref)}\left[1+\alpha_{\beta r}\left(T-T_{ref}\right)\right] \tag{6.1}$$

In Test 2, the current tracking ability of the proposed DPG–NCC under varying flux linkage is evaluated. The rotor flux linkage is increased and decreased by 20% at 0.3 s compared to the rated value keeping other parameters constant and the real–time SIL results are presented in Figs. 6.5 and 6.6, respectively. The updated flux linkage values are presented in Table 6.1. In the real–time SIL testing the reference *q*–axis current is changed from 10 A to 5 A at 0.3 s and again to 10 A at 0.6 s. Also, at 0.45 s the *d*–axis reference current is changed from –15 A to –5 A. Figure 6.5 illustrates the *d*– and *q*–axis current waveforms and Fig. 6.6 shows the electromagnetic torque waveforms of IPMSM for adaptive PI and DRL–based DPG–NCC under 20% increased flux linkage.

TABLE 6.1

IPMSM VARYING FLUX LINKAGE

20% Increased Value	**20% Decreased Value**
0.73 Wb	0.48 Wb

The evaluation of the proposed current control is achieved by operating the IPMSM at a constant speed and tracking the *d*– and *q*–axis currents. The DPG–NCC demonstrated in Fig. 6.5 adapts itself with fluctuating IPMSM rotor magnet flux. The transient electromagnetic torque overshoot at 0.3 s in Fig. 6.6 is observed due to flux linkage variation at 0.3 s. An enhanced dynamic current tracking under changing PM flux is observed in the proposed controller. Also, a better transient response of IPMSM electromagnetic torque by 4 Nm is noted under varying flux linkage. Similar current

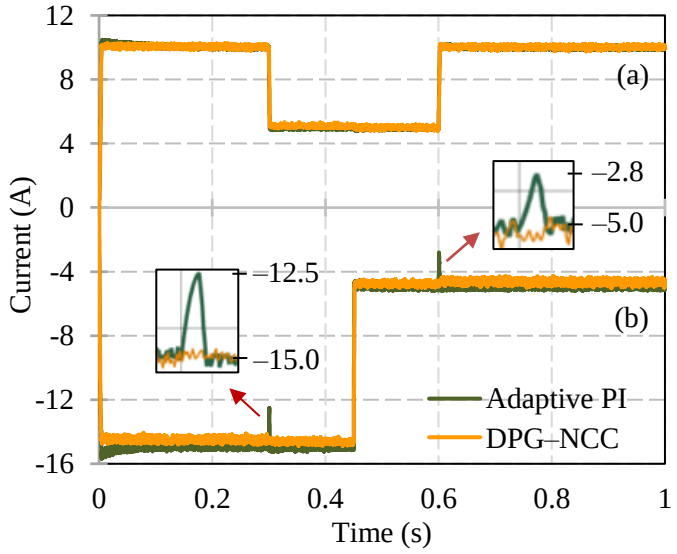

Fig. 6.5. Current tracking with 20% increased flux linkage, DPG–NCC versus adaptive PI control. (a) *q*–axis current. (b) *d*–axis current.

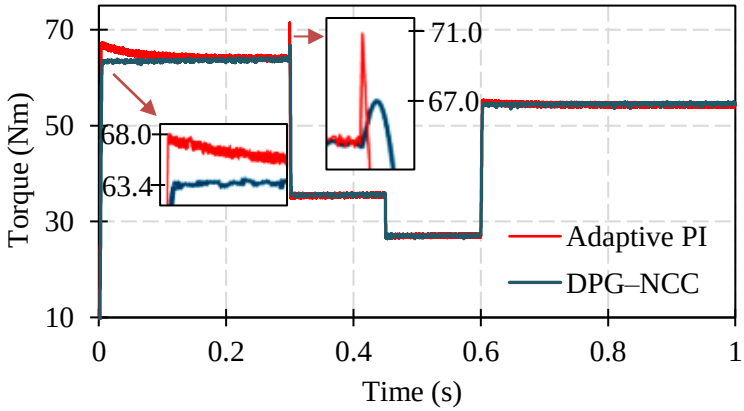

Fig. 6.6. IPMSM electromagnetic torque with 20% increased flux linkage, DPG–NCC versus adaptive PI control.

tracking and torque performance during transient conditions is observed under 20% reduced PM flux linkage. The reduction in transient response will further lead to reduced dynamic power loss under drive cycle condition with a full–scale 110 kW prototype of IPMSM drive.

*6.2.3 Test 3: Robustness of DRL–Based DPG–*NCC

Under the dynamic performance of IPMSM in traction applications, the electrical parameters change due to saturation and temperature. The change in time–varying parameters in PMSM affects the current control and system performances. In Test 3, the robustness of the proposed DRL–based DPG–NCC is evaluated with inductance and resistance changing. The current response and system performance of the DPG–NCC are evaluated by varying L_d, L_q, and R_s by 20% of the nominal value. The L_d, L_q, and R_s parameters for SIL validations are shown in Table 6.2. The proposed DPG–NCC results are compared with the adaptive PI controller.

TABLE 6.2

IPMSM TIME–VARYING PARAMETERS

Parameters	**20% Increased Value**	**20% Decreased Value**
q–axis Inductance, L_q	78.98×10^{-3} H	52.62×10^{-3} H
d–axis Inductance, L_d	36.54×10^{-3} H	24.36×10^{-3} H
Stator Resistance, R_s	1.2 Ohm	0.8 Ohm

With changing *d*–axis and *q*–axis currents, the L_d, L_q and R_s value is also increased by 20% at 0.3 s. The SIL validation results with the performance comparison are shown in Figs. 6.7 and 6.8. The transient overshoot and slow response in current and torque waveform due to decoupling inaccuracy of PI controller, $\omega_e L_q i_q$ and $-\omega_e L_d i_d$, is mitigated with the proposed controller. This will further reduce the instantaneous power loss under drive cycle conditions in a scaled–up prototype of IPMSM drive.

A very similar torque response for 20% reduced time–varying parameter is observed as shown in Fig. 6.8. The proposed DPG–NCC shows a more reliable, stable, and superior adaptive performance under dynamic conditions with parameter uncertainties of the IPMSM.

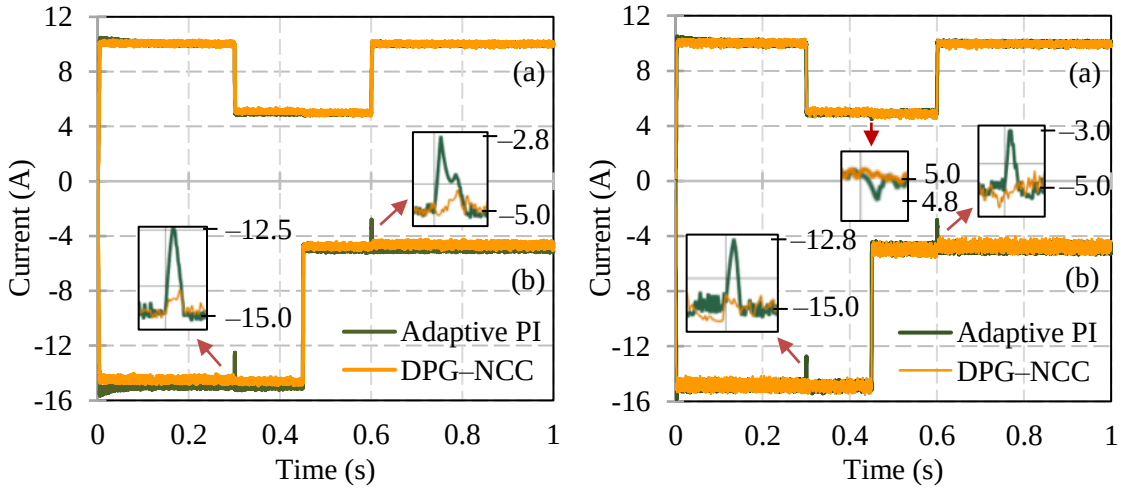

Fig. 6.7. Current tracking (i) 20% increased time–varying parameters and (ii) 20% reduced time–varying parameters, DPG–NCC versus adaptive PI control. (a) *q*–axis current. (b) *d*–axis current.

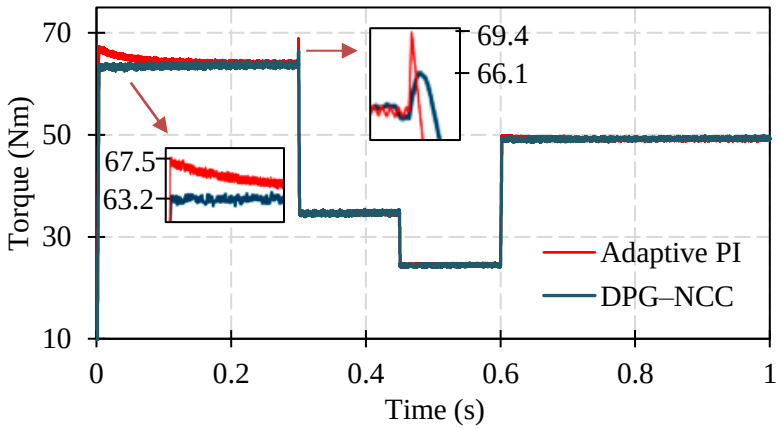

Fig. 6.8. IPMSM electromagnetic torque with 20% increased time–varying parameters, DPG–NCC versus adaptive PI control.

*6.2.4 Test 4: Effect of Sample Time on DRL–based DPG–*NCC

In real–time PMSM control, the speed control loop, current control loop and the hardware runs asynchronously with different discrete sampling time. Considering the machine coupling terms $\omega_e L_q i_q$ and $-\omega_e L_d i_d$, it is inferred that the rotating speed of IPMSM is directly related to stator *d*– and *q*–axis currents. Since the IPMSM speed and the electrical frequency are directly related to each other, the impact of the sampling rate plays

a vital role in the performance of the IPMSM. Also, the angular position of the motor changes very quickly with the change in rotational speed, and hence a smaller sampling time would be ideal for fast and efficient performance [1].

The proposed DDPG DRL–based current controller can be trained with a smaller sample time for a faster and more effective current response. Since the training and exploration of the DRL controller are time–consuming processes, the proposed DRL current controller is trained at a moderate sample time as 1×10^{-4} s. The training and exploration time can be significantly reduced through parallelization of CPU with CUDA–based graphics processing units (GPUs) or tensor processing units (TPUs) hardware [2].

In the current control as in Fig. 6.1, the reference stator current $i'_{d,q}$ and the IPMSM sample rate are implemented as 1×10^{-3} and 1×10^{-6} s, respectively. The IPMSM speed is varied and the impact of the sampling time on *d*– and *q*–axis current is shown in Fig. 6.9.

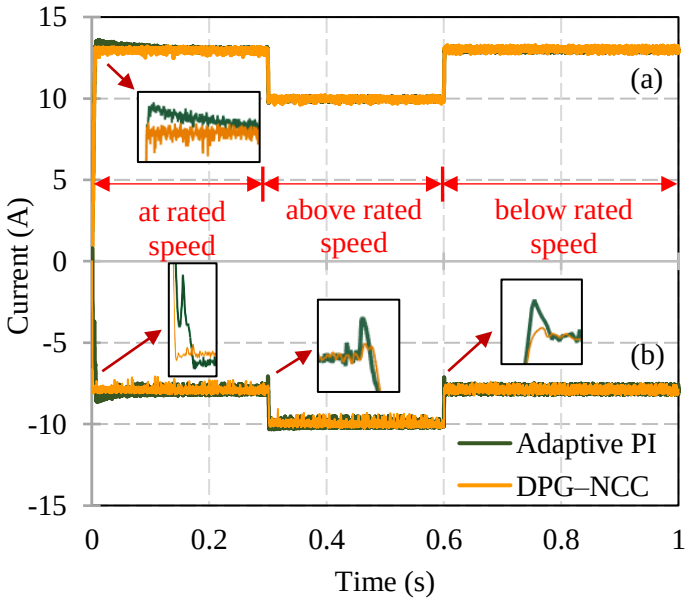

Fig. 6.9. Effect of sample time at different speed profiles, DPG–NCC versus adaptive PI control. (a) *q*–axis current. (b) *d*–axis current.

The proposed controller shows reduced transient overshoot by 2 A and improved performance stability.

6.2.5 Test 5: Computation Time

The computation cost of an algorithm plays a crucial role in the performance evaluation of the vector control in a real–time dynamic environment. To evaluate the computation for our proposed DPG–NCC with existing counterpart controls, Test 5 compares the computation time of the adaptive PI and DPG–NCC controllers.

For one simulation cycle, it is observed that the computation time of the adaptive PI controller is 0.255 seconds with 90,007 calls while the computation time of our proposed DRL–based DPG–NCC is only 0.017 s with 20,013 calls. The reduced computation time of the proposed controller is due to the strong function approximation and generalization ability of deep neural networks. The proposed DPG–NCC has a significantly reduced computational cost compared to the adaptive PI controller. The faster action of the proposed controller mitigates slow response in legacy dynamic conditions.

The implementation of the parameter independent DPG–NCC in IPMSM control shows reduced transient response in varying current and torque conditions. The fast response of the proposed DPG–NCC will further achieve a faster torque response with reduced power loss of IPMSM under drive cycle conditions. Due to the function approximation ability of the DPG–NCC, a reduced computation time is also observed in real–time implementation.

6.3 References

[1] H. Jie, G. Zheng, J. Zou, X. Xin, and L. Guo, “Adaptive Decoupling Control Using Radial Basis Function Neural Network for Permanent Magnet Synchronous Motor Considering Uncertain and Time-Varying Parameters,” *IEEE Access*, vol. 8, pp. 112323-112332, 2020.

[2] B. Zarebavani, F. Jafarinejad, M. Hashemi, and S. Salehkaleybar, "cuPC: CUDA-Based Parallel PC Algorithm for Causal Structure Learning on GPU," *IEEE Trans. Parallel and Distributed Systems*, vol. 31, no. 3, pp. 530-542, March 2020.

CHAPTER 7

CONCLUSION AND FUTURE WORK

7.1 Conclusion

The state–of–the–art PWM control strategy and vector control of IPMSM were investigated in this thesis. The study leads to the development of AI and machine learning based control strategies to improve the traditional control schemes. A brief summary of each chapter is presented below.

Chapter 1 presents an overview of the booming market of e–mobility across the world and Canada. This chapter introduces different traditional control strategies for PMSM e–drives. Furthermore, this chapter provides a brief illustration of the need for advanced and intelligent control methodologies. The chapter also gives the overall summary and objectives of the research.

Chapter 2 compares SPWM and SVM techniques to evaluate its performance. A mathematical model of an enhanced symmetrical SVM scheme is developed in this chapter. The SVM waveform of the model is validated using MATLAB Simulink.

Chapter 3 demonstrates a NN–based improved SVPWM control for GaN inverter in EV. One of the vital challenges in GaN inverter is to achieve high processing speed of complex algorithms during high switching frequency at reduced sample rate, which is achieved using the proposed NN–based improved SVPWM with low–cost DSP. Another challenge in GaN inverter is the switching loss which plays a key role in the performance of the inverter. The results exhibit the reduction of switching loss with the proposed control which, in turn, improves the efficiency of the GaN inverter. Furthermore, the results demonstrate that the NN–based improved SVPWM is superior to the conventional one in terms of time complexity and switching loss, and hence exhibit the feasibility and stability of the proposed control.

Chapter 4 presents the development of the mathematical model of the IPMSM motor and discusses its different conventional control strategies. A state–of–the–art adaptive PI–based control is used to leverage FOC. The enhance the transient performance

with changing IPMSM parameters, an intelligent deep reinforcement learning (DRL) based control is proposed.

Chapter 5 presents the next generation, novel deterministic policy gradient based novel current controller (DPG–NCC) for IPMSM. Different deterministic policy gradient learning methodologies are proposed for training and tuning of the proposed controller. The multi–critic methodology enabled faster optimization reducing the overall training period and further mitigates overestimation of *Q*–value in the early stage of learning. The overall control architecture of the DRL control is also illustrated in this chapter.

Chapter 6 extends the work from the Chapter 5 to validate the proposed DPG–NCC. The validation and testing of DPG–NCC–based parameter independent current control of IPMSM for EV application based on deep reinforcement learning (DRL) is presented in this chapter. The proposed DPG–NCC control shows accurate, reliable, adaptive, and efficient performance compared to conventional control techniques such as state–of–the–art adaptive PI control. The novel control also mitigates the need for supervised learning as in traditional machine learning. The exploration of RL agent with the plant environment enables accurate learning with a strong adaptive ability reducing transient overshoot responses, oscillations, and decoupling inaccuracy. The proposed DRL–based current controller is independent of IPMSM parameters and, hence mitigating complex tuning methods in non–linear systems. The fast response of DPG–NCC enables it to achieve the desired torque faster in the motor drive for electrified vehicle application. This study foresees an added advantage of online learning with the novel DPG–NCC current controller. Furthermore, the DPG–NCC controller concept can be adapted to other complex non–linear control systems.

7.2 Future Work

1. Implementation of the deterministic policy gradient control algorithm for parameter independent speed control loop of IPMSM. The deep deterministic policy gradient (DDPG) scheme, twin delayed deep deterministic policy gradient (TD3) or multi–critic multi–*Q*–learning (MCMQL) optimization can be used to train RL agent to achieve the optimal speed control. The block diagram of the proposed model is shown in Fig. 7.1, where $i \geq 1$ and $j \geq 1$

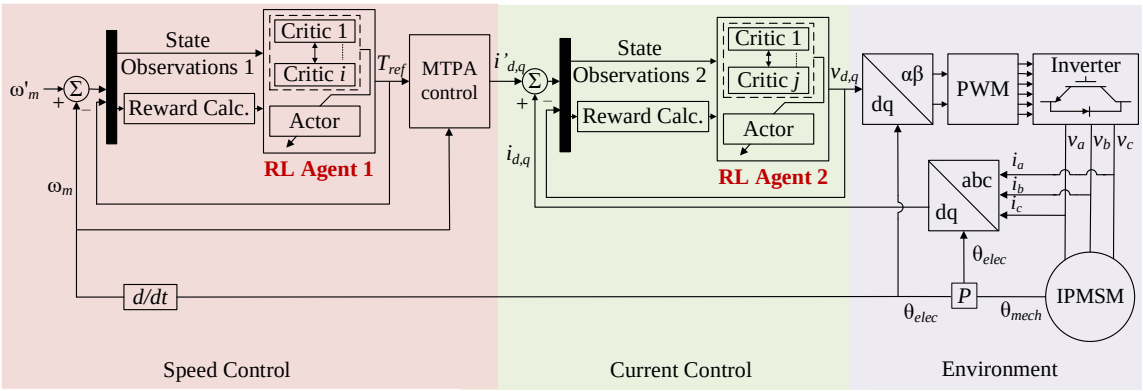

Fig. 7.1. Proposed future work on deterministic policy gradient–based speed control of IPMSM.

2. Extend and study the limit to detect fault–tolerant capability of dynamic PMSM drive controls using the proposed deep reinforcement learning (DRL) in EV powertrain

APPENDIX A

ABBREVIATIONS

Abbreviation	Explanation
ADC	Analog to Digital Converter
ANN	Artificial Neural Network
BEV	Battery Electric Vehicle
DDPG	Deep Deterministic Policy Gradient
DL	Deep Learning
DPG	Deterministic Policy Gradient
DPG–NCC	Deterministic Policy Gradient based Novel Current Control
DQL	Deep *Q*–Learning
DRL	Deep Reinforcement Learning
DSP	Digital Signal Processor
DTC	Direct Torque Control
EV	Electric Vehicle
FCEV	Fuel Cell Electric Vehicle
FOC	Field–Oriented Control
GA	Genetic Algorithm
GaN	Gallium Nitride
HEV	Hybrid Electric Vehicle
IM	Induction Motor
IPMSM	Interior Permanent Magnet Synchronous Motor
MDP	Markov Decision Process
ML	Machine Learning
MSBE	Mean–Squared Bellman Error
MSE	Mean Squared Error
MTPA	Maximum Torque per Ampere
N3V	Nearest Three Vector
NN	Neural Network

PHEV	Plug–in Hybrid Electric Vehicle
PI	Proportional–Integral
PID	Proportional–Integral–Differential
PMSM	Permanent Magnet Synchronous Motor
PWM	Pulse Width Modulation
RBFNN	Radial Bias Function Neural Network
RL	Reinforcement Learning
RNN	Recurrent Neural Network
SiC	Silicon Carbide
SMC	Sliding Mode Controller
SoH	State of Health
SPWM	Sinusoidal Pulse Width Modulation
SVM	Space Vector Modulation
TD	Temporal Difference
TD3	Twin Delay Deep Deterministic Policy Gradient
THD	Total Harmonics Distortion
VSI	Voltage Source Inverter
WBG	Wide Bandgap

APPENDIX B

PERMISSION FOR USING IEEE PUBLICATIONS

IEEE
Requesting permission to reuse content from an IEEE publication

Artificial Neural Network Based Improved Modulation Strategy for GaN–based Inverter in EV

Conference Proceedings:
2020 IEEE Canadian Conference on Electrical and Computer Engineering (CCECE)

Author: Soumava Bhattacharjee

Publisher: IEEE

Date: 30 Aug. 2020

Thesis / Dissertation Reuse

The IEEE does not require individuals working on a thesis to obtain a formal reuse license, however, you may print out this statement to be used as a permission grant:

Requirements to be followed when using any portion (e.g., figure, graph, table, or textual material) of an IEEE copyrighted paper in a thesis:

1) In the case of textual material (e.g., using short quotes or referring to the work within these papers) users must give full credit to the original source (author, paper, publication) followed by the IEEE copyright line © 2011 IEEE.
2) In the case of illustrations or tabular material, we require that the copyright line © [Year of original publication] IEEE appear prominently with each reprinted figure and/or table.
3) If a substantial portion of the original paper is to be used, and if you are not the senior author, also obtain the senior author's approval.

Requirements to be followed when using an entire IEEE copyrighted paper in a thesis:

1) The following IEEE copyright/ credit notice should be placed prominently in the references: © [year of original publication] IEEE. Reprinted, with permission, from [author names, paper title, IEEE publication title, and month/year of publication]
2) Only the accepted version of an IEEE copyrighted paper can be used when posting the paper or your thesis on-line.
3) In placing the thesis on the author's university website, please display the following message in a prominent place on the website: In reference to IEEE copyrighted material which is used with permission in this thesis, the IEEE does not endorse any of [university/educational entity's name goes here]'s products or services. Internal or personal use of this material is permitted. If interested in reprinting/republishing IEEE copyrighted material for advertising or promotional purposes or for creating new collective works for resale or redistribution, please go to http://www.ieee.org/publications_standards/publications/rights/rights_link.html to learn how to obtain a License from RightsLink.

If applicable, University Microfilms and/or ProQuest Library, or the Archives of Canada may supply single copies of the dissertation.

BACK CLOSE WINDOW

VITA AUCTORIS

NAME:	Soumava Bhattacharjee
PLACE OF BIRTH:	Cuttack, Odissa, India
YEAR OF BIRTH:	1995
EDUCATION:	SRM University, India, 2013 – 2017, B. Tech B. D. Memorial Institute, India., 2013, Pre–University